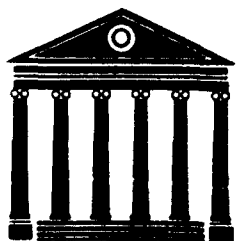Theoretical and Experimental Study of
Thermoacoustic Engines

Richard Raspet, Henry E. Bass and W. Pat Arnott

Physical Acoustics Research Laboratory
University of Mississippi
University, Mississippi 38677
PARGUM 90-12

THE UNIVERSITY OF MISSISSIPPI

PHYSICAL ACOUSTICS RESEARCH GROUP

DEPARTMENT OF PHYSICS AND ASTRONOMY

91 1 15 010

2

Theoretical and Experimental Study of
Thermoacoustic Engines

Richard Raspet, Henry E. Bass and W. Pat Arnott

Physical Acoustics Research Laboratory
University of Mississippi
University, Mississippi 38677
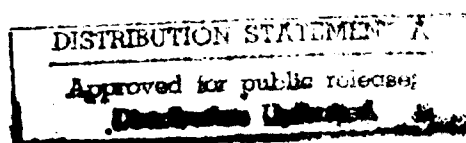PARGUM 90-12

20 December 1990

Annual Report
ONR Contract N00014-89-J-3087

JAN 1991

Prepared for:

Office of Naval Research
Department of the Navy
Arlington, Virginia 22217

REPORT DOCUMENTATION PAGE			*Form Approved* OMB No. 0704-0188

1a. REPORT SECURITY CLASSIFICATION UNCLASSIFIED		1b. RESTRICTIVE MARKINGS	
2a. SECURITY CLASSIFICATION AUTHORITY		3. DISTRIBUTION/AVAILABILITY OF REPORT Approved for public release; distribution unlimited.	
2b. DECLASSIFICATION/DOWNGRADING SCHEDULE			
4. PERFORMING ORGANIZATION REPORT NUMBER(S) PARGUM 90-12		5. MONITORING ORGANIZATION REPORT NUMBER(S)	

6a. NAME OF PERFORMING ORGANIZATION Physical Acoustics Research Laboratory	6b. OFFICE SYMBOL (If applicable)	7a. NAME OF MONITORING ORGANIZATION Office of Naval Research
6c. ADDRESS (City, State, and ZIP Code) The University of Mississippi University, MS 38677		7b. ADDRESS (City, State, and ZIP Code) Physics Division, Code 1112 Arlington, VA 22217-5000

8a. NAME OF FUNDING/SPONSORING ORGANIZATION OFFFICE OF NAVAL RESEARCH	8b. OFFICE SYMBOL (If applicable)	9. PROCUREMENT INSTRUMENT IDENTIFICATION NUMBER N00014-89-J-3087		
8c. ADDRESS (City, State, and ZIP Code) OFFICE OF NAVAL RESEARCH		10. SOURCE OF FUNDING NUMBERS		
		PROGRAM ELEMENT NO. 61153N	PROJECT NO.	TASK NO. 4126936	WORK UNIT ACCESSION NO.

11. TITLE (Include Security Classification)

Annual Report of Theoretical and Experimental Study of Thermoacoustic Engines

12. PERSONAL AUTHOR(S)

13a. TYPE OF REPORT Annual Summary	13b. TIME COVERED FROM Sept 89 TO 1 Sept 90	14. DATE OF REPORT (Year, Month, Day) 901220	15. PAGE COUNT 113

16. SUPPLEMENTARY NOTATION

17.	COSATI CODES		18. SUBJECT TERMS (Continue on reverse if necessary and identify by block number)
FIELD	GROUP	SUB-GROUP	Thermoacoustics, refrigerators
20	01		

19. ABSTRACT (Continue on reverse if necessary and identify by block number)

This annual report describes theoretical and experimental research during the past year on thermoacoustic engines. The work includes three principal components: 1) theoretical and experimental work performed by Dr. Bass at the Naval Postgraduate School, 2) theoretical investigation of the thermoacoustic engine from acoustic analysis rather than energy analysis, 3) and design of a low frequency thermoacoustic driver utilizing square pore material for the stack.

At the Naval Postgraduate School, Dr. Bass working with Dr. Atchley and Hofler of the NPG, developed an acoustic based theory to predict the onset of oscillation in a thermoacoustic driver and for the Q of the resonance and performed measurements. The experimental results agree well with the theory. At the University of Mississippi, an acoustic theory for thermoacoustic engines utilizing various stack geometries was developed. This theory was based on earlier work on sound propagation in arbitrary pore shapes. A thermoacoustic driver was designed based on the square pore theory.

20. DISTRIBUTION/AVAILABILITY OF ABSTRACT ☒ UNCLASSIFIED/UNLIMITED ☐ SAME AS RPT. ☐ DTIC USERS	21. ABSTRACT SECURITY CLASSIFICATION UNCLASSIFIED	
22a. NAME OF RESPONSIBLE INDIVIDUAL L.E. hargrove ONR Physics Division	22b. TELEPHONE (Include Area Code) (202) 69604221	22c. OFFICE SYMBOL ONR Code 1112

DD Form 1473, JUN 86   *Previous editions are obsolete.*   SECURITY CLASSIFICATION OF THIS PAGE

Table of Contents

THEORETICAL AND EXPERIMENTAL STUDY OF THERMOACOUSTIC ENGINES

1.0 Introduction

The major thrust of this research is the use of ceramic elements as the stack structure in a thermoacoustic device and the development of an acoustics based theory to calculate the behavior of the thermoacoustic engine. This work builds on previous work performed at the Naval Postgraduate School and Los Alamos National Laboratory on thermoacoustic engines and refrigerators as well as the Physical Acoustics Research Group extensive work on sound propagation through porous media.

The main body of this report describes the general formulation of thermoacoustics for stacks having arbitrary-shaped pore cross-sections. Attached appendices are papers describing the work performed by Dr. Bass at the Naval Postgraduate School, the development and testing of the theory of sound propagation in square pore material, and the design parameter of the UM low frequency thermoacoustic driver.

2.0 GENERAL FORMULATION OF THERMOACOUSTICS FOR STACKS HAVING ARBITRARILY-SHAPED PORE CROSS-SECTIONS

2.1 Introduction

The subject of modern thermoacoustics is primarily due to the work of N. Rott. His review paper[1] describes much of this work. Thermoacoustic streaming in a driven resonance tube was also investigated by Merkli and Thomann.[2] Rott and Merkli and Thomann were interested in thermoacoustic effects in a single tube having a circular cross section. Rott and Zouzoulas[3] also investigated thermally driven acoustic oscillations for circular tubes with variable cross-sectional area.

Wheatley, Cox, Swift, Hoffler and others have approached thermoacoustics from a more traditional thermodynamics point of view. Much of this work is reviewed by Swift.[4] They use thermoacoustic elements such as heat exchangers and a stack as shown in Fig. 2.1a to investigate thermoacoustically-driven prime movers and refrigerators. An exposed view of a thermoacoustic element is shown in Fig. 2.1b. Thermoacoustic elements consist of a parallel combination of many elementary capillary tubes or pores. For example in Fig. 2.1b the pores have square cross-sections. The theory for a thermoacoustic heat engine is built up from knowledge of thermoacoustic effects in a single capillary tube. Both Rott[5] and Swift[4] considered thermoacoustic effects for acoustic oscillation between parallel plates. Merkli and Thomann[2] and Rott[1,5] investigated thermoacoustic effects for tubes with circular cross-sections.

Our initial intent was to investigate thermoacoustic effects in a stack having square pores as shown in Fig. 2.1b. An inexpensive source of square pore stack material is the ceramic plug used in automobile catalytic converters.[6] We previously used this ideal-geometry material to investigate sound propagation in porous media.[7] Since ceramic has a low thermal conductivity in comparison to metals, it is ideal for use as a stack where heat loss due to normal conduction down the stack reduces efficiency.

In this paper, we investigate thermoacoustics for stacks having arbitrary pore geometries, (parallel slits, rectangular pores, equilateral-triangle pores, circular pores, etc).

In particular, we are interested in the following question: What are the minimum necessary calculations to describe the acoustics of gas-filled thermoacoustic elements made of arbitrary-perimeter capillary tubes. An example of an arbitrary-perimeter capillary tube is shown in Fig. 2.1c. Rott[5] pursued this question to the point of computing the acoustic field quantities pressure, density, particle velocity, and temperature for arbitrary perimeter tubes, and gave examples of parallel slit and circular pore geometries. Here we consider the acoustic field quantities and the second order energy flow for arbitrary perimeter pores. Heat and work flow are compared in the short stack approximation for stacks having the aforementioned pore geometries. In addition, we make connections between thermo-acoustic theory and capillary-tube-based porous media theory.

Once the acoustical behavior of the various thermoacoustic elements has been worked out, the elements must be connected in series inside of a resonator as shown in Fig. 2.1a. Previously, numerical integration of the acoustical equations was used to compute field quantities in the stack since in general a temperature gradient exists from one side to the other.[4] The physical parameters of ambient density, viscosity, specific heat, sound speed, thermal conductivity, etc, are temperature dependent and thus depend on location within the stack. An alternative method developed here assumes that the stack may be broken up into isothermal subsections over which the physical parameters are constant. When this assumption is made, techniques available to analyze waves in layered media are applicable. In particular, specific acoustic impedance and pressure translation theorems are developed to compute all acoustical field quantities and energy flow at each point in the resonator shown in Fig. 2.1a. This method of solution is easily generalized to more complicated systems, e.g. a resonator containing a refrigeration stack, a prime mover stack, and 4 heat exchangers. These translation theorems are uniformly applicable to propagation in heat exchangers, stacks, and in the wide-tube sections of the resonator.

a)

acoustic
driver

cold
heat
exch

stack

hot
heat
exch

resonance tube

b) exposed view of a thermoacoustic element

$T_{ambient} = T_0 + T_{0z} Z$

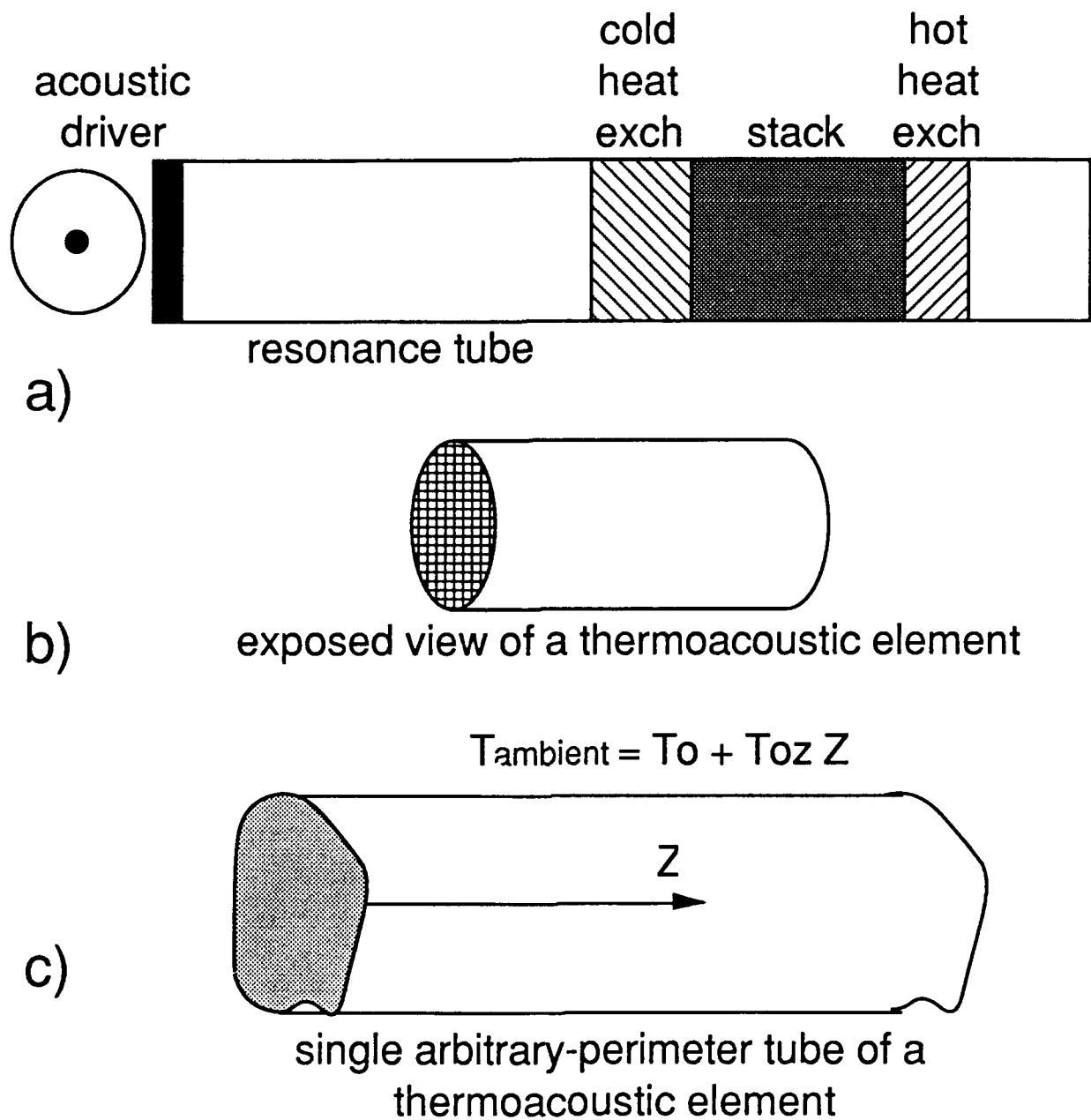c) single arbitrary-perimeter tube of a
thermoacoustic element

Figure 2.1 (a) Generic arrangement used in thermoacoustics. Thermoacoustics
elements are the heat exchanges and stack. (b) An exposed view of
a thermoacoustic element consisting of a parallel combination of
square capillary tubes. (c) A single arbitrary-perimeter capillary
tube for use in a thermoacoustic element.

4

2.2 Propagation in Thermoacoustic Elements from a Porous Media Analysis

A common design for the stack and heat exchangers in a thermoacoustic engine are equally spaced parallel plates. Fluid undergoes oscillitory flow between the plates allowing for greater heat transfer than would occur if the fluid was static. The pores in the parallel plate arrangement are described in their transverse direction as parallel slits and as straight tubes in their longitudinal direction. For arbitrary geometries, the stack or heat exchangers can be described as a section of a porous media. In this section, we first establish the fluid field equations and assumptions necessary to treat the general case. A wave equation for the pressure in a single pore is established. Enroute, we make reference to the terminology used in acoustical modeling of porous media. With the specific acoustic impedance assumed known at the hot end of the stack, we derive impedance and pressure translation theorems for the stack. Heat and work flow are computed for arbitrary pore geometries and are expressed in terms of pressure and specific acoustic impedance.

A. Fluid field equations and assumptions.

The transverse coordinates in a pore are taken to be x and y, and the longitudinal coordinate is z. For the stack, a positive linear temperature gradient exists on the pore in the z direction. Heat flows to and from the gas inside the pore to the walls so that, on the average, the temperature along the pore is the same for the fluid and the pore walls at the boundary. We assume that the pore walls are of sufficiently high heat capacity that the pore wall temperature is unaffected by temperature variations in the fluid caused by an acoustic wave. We also assume constant frequency pressure variations exist in the pore and that the pore walls are rigid. The pore is taken to be infinitely long in the z direction. With these assumptions, we would like to completely specify the acoustic field in the pore to first order in the acoustic variables.

The fluid quantities in a pore approximated to first order are:

$$P(z,t) = P_0 + P_1(z) \, exp(-i\omega t) \, , \tag{2.1}$$

$$v(x,y,z,t) = v(x,y,z) \, exp(-i\omega t) \, , \tag{2.2}$$

$$T(x,y,z,t) = T_0 + \frac{(T_H - T_0) \, z}{d} + T_1(x,y,z) \, exp(-i\omega t)$$
$$= T_0 + T_{0z} \, z \, + \, T_1(x,y,z) \, exp(-i\omega t), \tag{2.3}$$

$$s(x,y,z,t) = s_0(z) + s_1(x,y,z) \, exp(-i\omega t) \, , \tag{2.4}$$

$$\rho(x,y,z,t) = \rho_0(z) + \rho_1(x,y,z) \, exp(-i\omega t) \, . \tag{2.5}$$

Because of the ambient temperature gradient, physical parameters including density, viscosity, thermal conductivity, adiabatic sound speed, coefficient of thermal expansion, and the specific heats also depend on position. We ignore these variations within a section of small length. Later we will include this temperature dependence by treating the stack as a sum of short stacks with different temperatures. For physical parameters independent of position, the fluid field equations to first order are[8]

$$-i \, \omega \, \rho_0 \, v_z(x,y,z) = - \frac{dP_1(z)}{dz} + \eta \, \nabla^2_{xy} \, v_z(x,y,z) \, , \tag{2.6}$$

$$-i \, \omega \, \rho_1(x,y,z) + \frac{\partial(\rho_0(z) \, v_z(x,y,z))}{\partial z} + \rho_0(z) \frac{\partial v_x(x,y,z)}{\partial x} + \rho_0(z) \frac{\partial v_y(x,y,z)}{\partial y} = 0, \tag{2.7}$$

$$\rho_1(x,y,z) = - \rho_0(z) \, \beta \, T_1(x,y,z) + \frac{\gamma}{c^2} P_1(z) \, , \tag{2.8}$$

$$s_1(x,y,z) = \frac{c_p}{T_0} T_1(x,y,z) - \frac{\beta}{\rho_0} P_1(z) \, , \tag{2.9}$$

6

and

$$- i\omega\rho_0(z)c_pT_1(x,y,z) + \rho_0(z)c_pv_z(x,y,z)T_{0z} = -i\omega\beta T_0P_1(z) + \kappa\nabla^2_{xy}T_1(x,y,z), \quad (2.10)$$

where the transverse Laplacian operator is defined by $\nabla^2_{xy} = \left(\partial^2/\partial x^2 + \partial^2/\partial y^2\right)$. In order, these equations approximately express the z component of the equation of motion, continuity or mass conservation, equations of state for density and entropy, and heat transfer. Except for the T_{0z} terms in Eq. (2.10), these are the equations for the low reduced frequency solution[9] given by Zwikker and Kosten[10] in their solution for the propagation of sound in circular pores. In the derivation of Eq. (2.10), the convective derivative for the entropy is evaluated using the equation of state (2.9) and the relation $v \cdot \nabla s = v_z(x,y,z) \, ds_0(z)/dz = c_p \, v_z(x,y,z) \, T_{0z} \, / \, T_0$. Equation (2.10) shows that the temperature at a fixed position changes due to motion of the ambient fluid, due to compression of the gas, and due to heat conduction.

In writing Eq. (2.6), we assume that the longitudinal fluid velocity is much larger than the transverse velocity. We also assume that the transverse variation of the longitudinal velocity is much greater than the longitudinal variation. The latter assumption is sensible since the acoustic wavelength is much larger than the pore diameter. The fluid velocity vanishes at the pore wall and changes rapidly in a viscous boundary layer away from the pore wall. In Eq. (2.10), we have also made the assumption that the transverse variations of temperature are much greater than the longitudinal variation. Further discussion of these approximations may be found in references 4 and 9.

Several variations in notation should be noted. First, the viscous and thermal boundary layer thicknesses are given by $\delta_v = (2\eta/\omega\rho_0)^{1/2}$ and $\delta_\kappa = (2\kappa/\omega\rho_0c_p)^{1/2}$. Swift[4] writes most equations in terms of δ_v and δ_κ. Tijdeman[9] and Attenborough[11] introduce a dimensionless "shear wave number" $\lambda = R(\rho_0\omega/\eta)^{1/2}$ or $\lambda = 2^{1/2} R/\delta_v$ where R is a

characteristic transverse dimension of the pore. They also use the dimensionless thermal disturbance number $\lambda_T = R(\rho_0 \omega c_p / \kappa)^{1/2}$ or $\lambda_T = 2^{1/2} R / \delta_\kappa$ for the ratio of the pore radius to the thermal boundary layer thickness. Use of the Prandtl number $N_{pr} = \eta c_p / \kappa$ gives the relation $\lambda_T = \lambda N_{pr}^{1/2}$. For definiteness, we take R to be twice the ratio of the transverse pore area to the pore perimeter so for a circular or square pore, R is just the pore radius. In this paper we use the λ and λ_T notation.

B. Transverse velocity profile in a pore.

To obtain a solution to the equation of motion, Eq. (2.6), the z component of velocity is taken to be

$$v_z(x,y,z) = \frac{F(x,y;\lambda)}{i\omega\rho_0} \frac{dP_1(z)}{dz} . \tag{2.11}$$

From the equation of motion, Eq. (2.6), $F(x,y,\lambda)$ satisfies

$$F(x,y;\lambda) + \frac{R^2}{i\lambda^2} \nabla^2_{xy} F(x,y;\lambda) = 1 , \tag{2.12}$$

subject to the boundary condition that $F(x,y,\lambda)$ is zero at the pore walls. As we shall see, this is the only differential equation need be solved.

Denote by $v_z(z)$ and $F(\lambda)$ the average of $v_z(x,y,z)$ and $F(x,y;\lambda)$ over the cross section of the pore. The equation of motion for the fluid can now be expressed simply as

$$v_z(z) = \frac{dP_1(z)/dz}{i\omega\rho_0} F(\lambda). \tag{2.13}$$

8

The traditional approach of porous media modeling[10,11] introduces a complex density at this point which is defined as

$$\tilde{\rho}(z;\lambda) = \frac{\rho_0(z)}{F(\lambda)} \ .$$

(2.14)

Use of the terminology complex here implies that $\tilde{\rho}(z;\lambda)$ is a complex number. The complex density is the apparent dynamical density of the fluid in the pore.

C. Transverse temperature profile in a pore: complex compressibility.

The excess temperature in the pore fluid is given by Eq. (2.10). Algebraic rearrangement followed by use of the thermodynamic relation $T_0\,\beta^2/c_p = (\gamma - 1)/c^2$ for the first term on the right and by use of Eq. (2.11) results in a simplified expression for the excess temperature,

$$T_1(x,y,z) + \frac{R^2}{i\lambda_T^2}\nabla^2_{xy}\,T_1(x,y,z) = \frac{\gamma - 1}{c^2\rho_0\beta}P_1(z) - \frac{T_{0z}}{\rho_0\omega^2}F(x,y;\lambda)\frac{dP_1(z)}{dz} \ .$$

(2.15)

We may assume a superposition form of $T_1(x,y,z)$,

$$T_1(x,y,z) = \tau_a(x,y)\,P_1(z) + \tau_b(x,y)\frac{dP_1(z)}{dz} \ .$$

(2.16)

Following Rott[1], Eq. (2.16) is split into two equations corresponding to the inhomogeneous terms,

$$\tau_a(x,y) + \frac{R^2}{i\,\lambda_T^2}\nabla^2_{xy}\,\tau_a(x,y) = \frac{\gamma - 1}{c^2\,\rho_0\,\beta} \ ,$$

(2.17)

9

$$\tau_b(x,y) + \frac{R^2}{i \lambda_T^2} \nabla^2_{xy} \tau_b(x,y) = - \frac{T_{0z}}{\rho_0 \omega^2} F(x,y;\lambda) \ . \tag{2.18}$$

Comparing Eq. (2.17) with Eq. (2.8), the solution for Eq. (2.17) follows immediately,

$$\tau_a(x,y) = \frac{\gamma - 1}{c^2 \rho_0 \beta} F(x,y;\lambda_T) \ . \tag{2.19}$$

To obtain the solution for $\tau_b(x,y)$ in Eq. (2.18), Eq. (2.19) can be used in Eq. (2.17) along with the differential equation for $F(x,y;\lambda)$ in Eq. (2.12) to prove the following result,

$$\tau_b(x,y) = - \frac{T_{0z}}{\rho_0 \omega^2} \frac{F(x,y;\lambda_T) - N_{pr} F(x,y;\lambda)}{1 - N_{pr}} \ . \tag{2.20}$$

The general solution for the excess temperature from Eq. (2.16) is

$$T_1(x,y,z) = \frac{\gamma - 1}{c^2 \rho_0 \beta} F(x,y;\lambda_T) P_1(z)$$

$$- \frac{T_{0z}}{\rho_0 \omega^2} \frac{F(x,y;\lambda_T) - N_{pr} F(x,y;\lambda)}{1 - N_{pr}} \frac{dP_1(z)}{dz} \ . \tag{2.21}$$

The equation of state for the acoustic density fluctuation, Eq. (2.8), can be combined with the expression for the acoustic temperature , Eq. (2.21) to give

$$\rho_1(x,y,z) = \frac{1}{c^2} \left(\gamma - (\gamma - 1) F(x,y,\lambda_T) \right) P_1(z)$$

$$+ \frac{\beta T_{0z}}{\omega^2} \frac{F(x,y;\lambda_T) - N_{pr} F(x,y;\lambda)}{1 - N_{pr}} \frac{dP_1(z)}{dz} \ . \tag{2.22}$$

10

The first term on the right of Eq. (2.22) can be used to define a complex compressibility.

When T_{0z} is zero, Eq. (2.22) can be used to define a complex compressibility which is useful in porous media theory.[10,11] Denote by $\rho_1(z)$, $F(\lambda_T)$, and $F(\lambda)$ as the average of $\rho_1(x,y,z)$, $F(x,y;\lambda_T)$ and $F(x,y;\lambda)$ over the cross section of the pore. Following the traditional approach of porous media modeling,[10,11] the complex compressibility is defined as

$$\tilde{C}(z;\lambda_T) = \frac{1}{\rho_0} \frac{\rho_1(z)}{P_1(z)} \ .$$

(2.23)

and from Eq. (2.22), with $T_{0z} = 0$, is given by

$$\tilde{C}(z;\lambda_T) = \frac{1}{\rho_0 c^2} \left(\gamma - (\gamma - 1) F(\lambda_T) \right) \ .$$

(2.24)

The cross-sectionally-averaged density can then be expressed as

$$\rho_1(z) = \rho_0 \tilde{C}(z;\lambda_T) P_1(z) + \frac{\beta T_{0z}}{\omega^2} \frac{F(\lambda_T) - N_{pr} F(\lambda)}{1 - N_{pr}} \frac{dP_1(z)}{dz} \ .$$

(2.25)

As was the case with the complex density, the use of the terminology complex signifies that $\tilde{C}(z;\lambda_T)$ is a complex number. The motivation for averaging the density over the cross section of the pore becomes apparent in the next section.

D. Pressure wave equation in a pore.

The continuity equation, Eq. (2.7), along with the equation of motion, Eq. (2.13), and the equation of state for the density, Eq. (2.25), can be combined to yield a wave

equation for the pressure in a pore. The boundary conditions on v_x and v_y are that they vanish at the pore wall. By assuming that we may interchange the operation of z differentiation and averaging over x and y coordinates, the cross sectionally averaged continuity equation for the pore is

$$-i\,\omega\,\rho_1(z) + \frac{d}{dz}\big(\rho_0(z)\,v_z(z)\big) = 0 \; . \tag{2.26}$$

To make progress the z derivative on the second term must be applied to the right hand side of Eq. (2.13). Use of Eq. (2.13) gives

$$\frac{d}{dz}\big(\rho_0(z)\,v_z(z)\big) = \frac{1}{i\omega}\,\frac{d}{dz}\bigg(F(\lambda)\,\frac{dP_1(z)}{dz}\bigg). \tag{2.27}$$

The derivative of $F(\lambda)$ with respect to z occurs because λ depends on temperature and hence on z also. Multiplying Eq. (2.26) by $i\omega$, dividing through by $F(\lambda)$, using the complex density of Eq. (2.14), the equation of state for density, Eq. (2.25), and Eq. (2.27), the wave equation for pressure is

$$\frac{1}{F(\lambda)}\,\frac{d}{dz}\bigg(F(\lambda)\frac{dP_1(z)}{dz}\bigg) \;+\; 2\,\alpha(\lambda,\lambda_T)\,\frac{dP_1(z)}{dz} \;+\; \zeta^2(\lambda,\lambda_T)\,P_1(z) = 0\,, \tag{2.28}$$

where

$$\alpha(\lambda,\lambda_T) = \frac{T_{0z}}{2}\,\bigg(\beta\,\frac{F(\lambda_T)/F(\lambda) - N_{pr}}{1 - N_{pr}}\bigg)\,, \tag{2.29}$$

and

$$\zeta(\lambda,\lambda_T)^2 = \frac{\omega^2}{c^2}\,\frac{1}{F(\lambda)}\,\big(\gamma - (\gamma - 1)\,F(\lambda_T)\big) \; . \tag{2.30}$$

12

In the abscence of a temperature gradient, $T_{0z} = 0$ so $\alpha(\lambda, \lambda_T) = 0$. The propagation constant in the pore is then given by $\pm \zeta$ which is the usual form used in porous media modeling.[10,11] The form of the wave equation for pressure is reminiscent of the time analog of a damped harmonic oscillator; however, here α and ζ are complex quantities.

E. Specific acoustic impedance and pressure translation theorems.

It is appropriate to establish the terminology used in this section. The specific acoustic impedance of an acoustical medium is equal to the ratio of the total acoustic pressure and total particle velocity. For example, in a fluid layer, the total pressure is a combination of a down going wave and an upgoing wave. The acoustic impedance is equal to the ratio of the total acoustic pressure and the total volume velocity. For porous media, the appropriate boundary condition at a surface is continuity of the acoustic impedance.[11] For adiabatic sound, the characteristic or intrinsic impedance is equal to $\rho_0 c$ where ρ_0 is the ambient density and c is the adiabatic sound speed.

Rayleigh developed an impedance translation theorem for homogeneous fluid layers.[12] The impedance translation theorem relates the specific acoustic impedance at one side of a layer to that at the other. In this manner, one may apply the theorem as many times a necessary to compute the specific acoustic impedance at any surface in the layered media.

To this point, we have considered propagation in a single pore of infinite length. Denote by N the number of pores per unit area in a porous sample (e.g. Fig. 2.1b) consisting of a parallel combination of many identical single pores (e.g. Fig. 2.1c) of finite length. Define by V_{zb} a particle velocity for the bulk porous sample, by A_{res} the area of the resonator at the face ot the sample, and by A the area of a single pore in the sample. Volume velocity is $A_{res} V_{zb} = N A A_{res} v_z = \Omega A_{res} v_z$ where $\Omega = N A$ is the porosity of the sample. Thus by using $v_z = V_{zb} / \Omega$ in all of the single pore equations, both acoustic

13

impedance and specific acoustic impedance are continuous at each interface (e.g. at the stack, heat exchanger interface in Fig. 2.1a) between the porous media.

Several assumptions are necessary to construct an impedance translation theorem for the stack. First, although the stack temperature varies continuously from the hot end to the cold end, we assume that the stack can be modeled as a series of isothermal layers. Each layer temperature is the average of the temperature at the ends as indicated in Fig. 2.2. The number of layers and layer thickness are practically unrestricted. The physical parameters $\lambda = R \, (\rho_0 \, \omega / \eta)^{1/2}$ and $\lambda_T = R \, (\rho_0 \, c_p \, \omega / \kappa)^{1/2}$ are taken to be constant within a layer, and are evaluated for the average temperature of the layer. The most important consequence of these assumptions is that α and ζ in Eq. (2.29) can be considered constant within a layer. The wave equation for pressure, Eq. (2.29), can then be solved easily and an impedance translation theorem analogous to Rayleigh's may be derived. We also assume that the acoustic field equations developed in Sec. 2.2A through Sec. 2.2D apply to each finite length pore in the stack.

$$Z - d \qquad\qquad Z \qquad\qquad Z + d$$

To + Toz (Z - d/2) | To + Toz (Z + d/2)
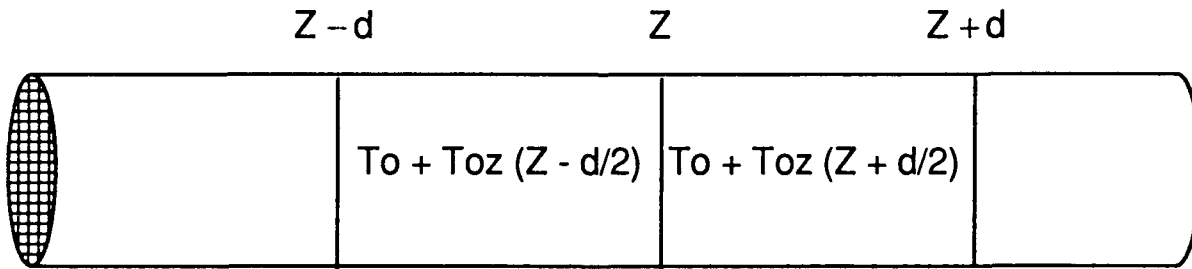
ISOTHERMAL SUBSECTIONS OF A
THERMOACOUSTIC
ELEMENT

Figure 2.2   An isothermal subsection of a thermoacoustic element, shown here having square pore capillary tubes. Each subsection is taken to be locally isothermal, at the average temperature of the end temperatures. For the stack thermoacoustic element, an arbitrary number of subsections may be used in spanning the temperature difference at the ends of the stack. Constant temperature heat exchangers are associated with only one subsection.

Allowing for these assumptions, the solution of Eq. (2.28) is

$$P_1(z) = B \, exp(-\alpha z) \, exp(i \, kz) \; + \; D \, exp(-\alpha z) \, exp(-i \, kz), \tag{2.31}$$

where B and D are constants and

$$k^2 = \zeta^2 - \alpha^2 \quad . \tag{2.32}$$

One must take care in obtaining k since both ζ and α are complex quantities. From Eq. (2.13), bulk particle velocity is

$$V_{zb}(z) = \frac{F(\lambda)\Omega}{\omega\rho_0} \Big(B(i\alpha + k) exp(-\alpha z) exp(ikz) + D(i\alpha - k) exp(-\alpha z) exp(-i \, kz) \Big). \tag{2.33}$$

From Eq. (2.31) and Eq. (2.33), one may compute a propagator formalism in the usual way,

$$\begin{pmatrix} P_1(z-d) \\ V_{zb}(z-d) \end{pmatrix} = exp(\alpha d) \begin{pmatrix} cos(kd) - \alpha/k \, sin(kd) & -i \, Z_{int} sin(kd) \\ -i \, \dfrac{1 + \alpha^2/k^2}{Z_{int}} sin(kd) & cos(kd) + \dfrac{\alpha}{k} sin(kd) \end{pmatrix} \begin{pmatrix} P_1(z) \\ V_{zb}(z) \end{pmatrix} \tag{2.34}$$

where $Z_{int} = \rho_0 \, \omega \, / \, (F(\lambda) \, \Omega \, k)$ is analogous to characteristic impedance. From use of Eq. (2.34), and referring to Fig. 2.2, a right-to-left impedance translation theorem can be computed

$$Z(z-d) = Z_{int} \, \frac{Z(z) \, [cos(kd) - \alpha/k \, sin(kd)] - i \, Z_{int} \, sin(kd)}{Z_{int} \, [cos(kd) + \alpha/k \, sin(kd)] - i \, Z(z) \, [1 + \alpha^2/k^2] \, sin(kd)}, \tag{2.35}$$

and a left-to right pressure translation theorem can be computed

$$P_1(z+d) = exp(-\alpha d) \, P_1(z) \left(cos(kd) + \left(\frac{\alpha}{k} + i \, \frac{Z_{int}}{Z(z)} \right) sin(kd) \right) \quad . \tag{2.36}$$

15

The impedance translation theorem reduces to Rayleigh's form when no temperature gradient is present on the stack and $\alpha = 0$. Use of these translation theorems will be discussed next.

The translation theorems in Eq. (2.35) and Eq. (2.36) can be used to determine the impedance and pressure at all points in the resonance tube in Fig. 2.1. For thermoacoustic elements other than the stack, $\alpha = 0$ in Eqs. (2.35) and (2.36). One starts with a known value of impedance at one end of the tube. As an example, the rigid end of the tube in Fig. 2.1a a starting point. Subsequent use of Eq. (2.35) determines Z at the hot heat exchanger interface, the stack-hot-heat-exchanger interface, etc. The stack may be broken up into several isothermal layers as indicated in Fig. 2.2. Finally the acoustic impedance at the acoustic driver can be computed. For known acoustic driver response (e.g. perhaps constant velocity or constant displacement, etc), the pressure can be determined at the driver location. Then use us Eq. (2.36) determines the pressure at all points. It should be noted that all variables in Eq. (2.35) and Eq. (2.36) are to be evaluated at the local position of the thermoacoustic element or subsection. The translation theorem approach for computing acoustical quantities is a superior way of performing calculations for resonators containing many thermoacoustic elements. Knowledge of heat and work flow is central to thermoacoustics. In the next section, heat and work flow are evaluated for arbitrary pore perimeters and are expressed in terms of pressure and specific acoustic impedance.

F. Heat and work flow.

The time averaged energy flow $\overline{H}_2(z)$ is[4]

$$\overline{H}_2(z) = \overline{Q}_2(z) + \overline{W}_2(z) - \overline{Q}_{loss}(z) \tag{2.37}$$

16

where time averaged heat flow due to hydrodynamic transport $\bar{Q}_2(z)$ is[4]

$$\bar{Q}_2(z) = \frac{\Omega A}{2} \text{Re} \frac{1}{A_p A_p} \int \left(\rho_0 c_p v_z(x,y,z) T_1(x,y,z)^* - \beta T_0 v_z(x,y,z) P_1(z)^* \right) dx\,dy \quad (2.38)$$

the heat flow due to conduction down a temperature gradient is[4]

$$\bar{Q}_{loss}(z) = \Omega A \kappa_{gas} T_{0z} + (1 - \Omega) A \kappa_{stack} T_{0z} , \quad (2.39)$$

and the time averaged work flow $\bar{W}_2(z)$ is[4]

$$\bar{W}_2(z) = \frac{\Omega A}{2} \text{Re} \frac{1}{A_p A_p} \int v_z(x,y,z) P_1(z)^* dx\,dy . \quad (2.40)$$

Here A is the cross-sectional area of the resonance tube at point z, A_p is the cross-sectional area of a single pore, Ω is porosity, κ_{gas} and κ_{stack} are the thermal conductivity of the gas and stack, and Re indicates the real part of the expression. The product ΩA is cross-sectional open area of the tube at position z.

To compute $\bar{Q}_2(z)$ and $\bar{W}_2(z)$ we make use of Eq. (2.21) for $T_1(x,y,z)$ and Eq. (2.11) for $v_z(x,y,z)$ in Eq. (2.38) and Eq.(2.39). Resulting expressions are

$$\bar{Q}_2(z) = \frac{\Omega A}{2} \frac{\rho_0 c_p}{A_p} \text{Im} \int_{A_p} \frac{F(x,y;\lambda)}{\omega \rho_0} P_{1z}(z) \times$$

$$\left(\frac{\gamma - 1}{c^2 \rho_0 \beta} F(x,y;\lambda_T)^* P_1(z)^* - \frac{T_{0z}}{\rho_0 \omega^2} \frac{F(x,y;\lambda_T)^* - N_{pr} F(x,y;\lambda)^*}{1 - N_{pr}} P_{1z}(z)^* \right) dx\,dy$$

$$- \beta T_0 \bar{W}_2(z) \quad (2.41)$$

where $P_{1z}(z) = dP_1(z)/dz$ and $*$ implies complex conjugation, and

$$\bar{W}_2(z) = \frac{\Omega A}{2} \frac{1}{A_p} \, \text{Im} \int_{A_p} \frac{F(x,y;\lambda)}{\omega \rho_0} P_{1z}(z) \, P_1(z)^* \, dx \, dy \quad . \tag{2.42}$$

Recal the definitions $\lambda_T = N_{pr}^{1/2} \lambda$ and

$$F(\lambda) = \frac{1}{A_p} \int_{A_p} F(x,y;\lambda) \, dx \, dy \quad . \tag{2.43}$$

The following general integral result, which is proven at the end of this section,

$$I_1 \equiv \frac{1}{A_p} \int_{A_p} F(x,y;\lambda) \, F(x,y;\lambda_T)^* \, dx \, dy \;=\; \frac{F(\lambda) \, N_{pr} + F(\lambda_T)^*}{N_{pr} + 1} \quad , \tag{2.44}$$

and

$$I_2 \equiv \frac{1}{A_p} \int_{A_p} F(x,y;\lambda) \, F(x,y;\lambda)^* \, dx \, dy \;=\; \underset{N_{pr}=1}{\text{Lim}} \; I_1 \;=\; \text{Re} \, F(\lambda). \tag{2.45}$$

are necessary to evaluate Eqs. (2.42) and (2.43). By making use of these integrals and the thermodynamic relation $\gamma - 1 = \beta^2 \, T_0 \, c^2 / c_p$, heat and work flow are

$$\bar{Q}_2(z) = \frac{\Omega A}{2} \beta \, T_0 \; \text{Im}\!\left(\frac{P_{1z}(z) \, P_1(z)^*}{\rho_0 \, \omega} \; \frac{F(\lambda_T)^* - F(\lambda)}{1 + N_{pr}} \right) -$$

$$\frac{\Omega A}{2} \, T_{0z} \frac{c_p}{\rho_0 \, \omega^3} \, |P_{1z}(z)|^2 \; \frac{\text{Im}\!\left(F(\lambda_T)^* + N_{pr} \, F(\lambda) \right)}{1 - N_{pr}^2} \quad , \tag{2.46}$$

18

are

$$\bar{\vec{W}}_2(z) = \frac{\Omega A}{2} \; \text{Im}\!\left(\frac{P_{1z}(z)\, P_1(z)^*}{\rho_0\, \omega} \; F(\lambda) \right) \; . \tag{2.47}$$

Equations (2.46) and (2.47) are general expressions for heat and work flow with the functional form of $F(\lambda)$ dependent on the particular pore geometry. It can be shown that Eq. (2.46) and Eq. (2.47) are the same as Swift's[4] equations for the special case of parallel slit geometries and assuming the $\varepsilon_s = 0$ (appropriate for gas thermodynamics) in Swift's theory.

Since impedance and pressure translation theorems have been derived for arbitrary locations within the resonator, and specifically for the stack element, it is useful to express heat and work flow in terms of the specific acoustic impedance $Z(z)$ and pressure $P_1(z)$. From the definition of specific acoustic impedance, $Z(z) = P_1(z) / (\Omega\, v_z(z))$, and Eq. (2.8) for $v_z(z)$,

$$\frac{dP_1(z)}{dz} = P_{1z}(z) = \frac{i\omega\rho_0\, P_1(z)}{\Omega\, F(\lambda)\, Z(z)} \; . \tag{2.48}$$

Heat and work flow are

$$\bar{\vec{Q}}_2(z) = \frac{\Omega A}{2} \, \beta\, T_0\, |P_1(z)|^2 \; \text{Im}\!\left(\frac{i}{\Omega\, Z(z)} \; \frac{F(\lambda_T)^*/F(\lambda) - 1}{1 + N_{pr}} \right) -$$

$$\frac{\Omega A}{2}\, |P_1(z)|^2 \, T_{0z} \frac{\rho_0\, c_p}{\omega} \, \frac{1}{|F(\lambda)\Omega Z(z)|^2} \; \frac{\text{Im}\!\left(F(\lambda_T)^* + N_{pr}\, F(\lambda)\right)}{1 - N_{pr}{}^2} \; , \tag{2.49}$$

are

$$\bar{W}_2(z) = \frac{\Omega A}{2} \; |P_1(z)|^2 \, \mathrm{Im}\!\left(\frac{i}{\Omega \, Z(z)} \right) \; . \tag{2.50}$$

In Eqs. (2.49) and (2.50), $P_1(z)$ and $Z(z)$ are global variables in that they depend on the detailed arrangement of all elements of the thermoacoustic engine, and $F(\lambda)$ and $F(\lambda_T)$ depend on the local properties of the gas and stack.

The remainder of this section is devoted to proof of Eq. (2.44). From Eq. (2.12), we can write Eq. (2.44) as

$$I_1 = \frac{1}{A_p} \int\limits_{A_p} F(x,y;\lambda) \left(1 + \frac{R^2}{i\lambda_T^2} \nabla^2_{xy} \, F(x,y;\lambda_T)^* \right) dx \; dy \tag{2.51}$$

Integration by parts and the definition of $F(\lambda)$ give

$$I_1 = F(\lambda) + \frac{1}{A_p} \frac{R^2}{i\lambda_T^2} \int\limits_{A_p} \nabla_{xy} \cdot \left(F(x,y;\lambda) \, \nabla_{xy} F(x,y;\lambda_T)^* \right) dx \; dy$$

$$\qquad - \frac{1}{A_p} \frac{R^2}{i\lambda_T^2} \int\limits_{A_p} \nabla_{xy} F(x,y;\lambda) \cdot \nabla_{xy} F(x,y;\lambda_T)^* \, dx \; dy \quad , \tag{2.52}$$

where the gradient operator in the x,y plane is ∇_{xy}. The divergence theorem in the x,y plane can be applied to the second integral in Eq. (2.52). From the divergence theorem, we have

$$\int\limits_{A_p} \nabla_{xy} \cdot \left(F(x,y;\lambda) \, \nabla_{xy} F(x,y;\lambda_T)^* \right) dx \; dy \; =$$

$$\int\limits_{S} \mathbf{n} \cdot \left(F(x,y;\lambda) \, \nabla_{xy} F(x,y;\lambda_T)^* \right) dS = 0 \quad , \tag{2.53}$$

where dS is an element of perimeter on the pore of arbitrary shape, and **n** is the outward normal at the pore wall. The integral in Eq. (2.53) is zero by the boundary condition $F(x,y;\lambda) = 0$ for x and y on S. Thus

$$I_1 = F(\lambda) - \frac{1}{A_p} \frac{R^2}{i\lambda_T^2} \int_{A_p} \nabla_{xy} F(x,y;\lambda) \cdot \nabla_{xy} F(x,y;\lambda_T)^* \, dx \, dy \quad . \qquad (2.54)$$

Now we could have instead used Eq. (2.12) for $F(x,y;\lambda)$ in Eq. (2.44), rather than for $F(x,y;\lambda_T)^*$ as we did to obtain Eq. (2.54). Had we done this, Eq. (2.54) would be

$$I_1 = F(\lambda_T)^* + \frac{1}{A_p} \frac{R^2}{i\lambda^2} \int_{A_p} \nabla_{xy} F(x,y;\lambda) \cdot \nabla_{xy} F(x,y;\lambda_T)^* \, dx \, dy \quad . \qquad (2.55)$$

Eliminating the common integral between Eq. (2.54) and Eq. (2.55) gives Eq. (2.44).

2.3 Heat and Work Flow in the Short Stack Approximation for Various Stack Geometries

In this section heat flow is compared for stacks consisting of a variety of capillary tubes. In addition to the square pore stack shown in Fig. 2.1b, parallel plate, circular, and equilateral triangular capillary tubes will be considered. Figure 32. shows the arrangment for the short stack approximation. In this approximation, pressure and specific acoustic impedance are given by empty-tube values for empty tube propagation constant k_0,

$$Z(s) = i \, \rho_0 \, c \, cot \, (k_0 s) , \qquad (2.56)$$

and

$$P_1(s) = \frac{i \, \rho_0 \, c \, V_0 \, cos(k_0 s)}{sin \, (k_0 L)} \qquad (2.57)$$

21

Use of Eq. (2.56) and Eq. (2.57) in the heat flow equation, Eq. (2.49) gives

$$\bar{Q}_2(z) = \frac{A_{res} \, V_0^2}{2 sin^2(k_0 L)} \frac{\beta \, T_0 \, \rho_0 \, c}{1 + N_{pr}} \frac{sin \, (2k_0 s)}{2} Im \, [F^*(\lambda_T)/F(\lambda)]$$

$$\left(1 - \Gamma \frac{Im \, \{F^*(\lambda_T) + N_{pr} \, F(\lambda)\}}{Im \, \{F^*(\lambda_T)F(\lambda)\} \, (1 - N_{pr})} \right) \tag{2.58}$$

where

$$\Gamma = \frac{T_{0z}}{T_0} \frac{\beta \, T_0 \, c \, tan \, (k_0 s)}{\omega \, (\gamma - 1)} . \tag{2.59}$$

In the inviscid approximation for which $N_{pr} = 0$, $F(\lambda) = 1$,

$$\bar{Q}_2(z) = \frac{A_{res} \, V_0^2}{2 sin^2(k_0 L)} \beta \, T_0 \, \rho_0 \, c \, \frac{sin \, (2k_0 s)}{2} \, Im \, F^*(\lambda_T) \, (1 - \Gamma) . \tag{2.60}$$

Physically, the term $Im \, F^*(\lambda_T)$ is a measure of the dynamic thermal interaction between the gas and solid. Recall that $\lambda_T = R \, (\rho_0 \, \omega \, c_p / \kappa)^{1/2}$ where R is twice the ratio of capillary pore area to pore perimeter. The function $F(x, y; \lambda_T)$ is a solution to the partial differential equation, Eq. (2.12), for a particular pore geometry and $F(\lambda_T)$ is the average of this quantitiy over the pore cross-section. According to Eq. (2.60), stacks made of pores for which $Im \, F^*(\lambda_T)$ is a large value will result in the greatest heat flow.

Work flow is given generally by Eq. (2.50). No work is done in the region to the right of the stack in Fig. 2.3, which can be verified readily by using the impedance of Eq. (2.56) in Eq. (2.50). In this region, pressure and velocity have standing wave phasing. Work is done in the stack. To compute the amount of work done, we make use of the

22

impedance translation theorem to compute the impedance at the left side of the stack. In the short stack approximation we take $kd \ll 1$, hence from Eq. (2.35),

$$Z(s+d) = Z(s) \left(1 - 2\alpha d - \frac{i \rho_0 \omega d}{F(\lambda) Z(s)} + \frac{i d Z(s) \zeta^2 F(\lambda)}{\rho_0 \omega} \right) . \qquad (2.61)$$
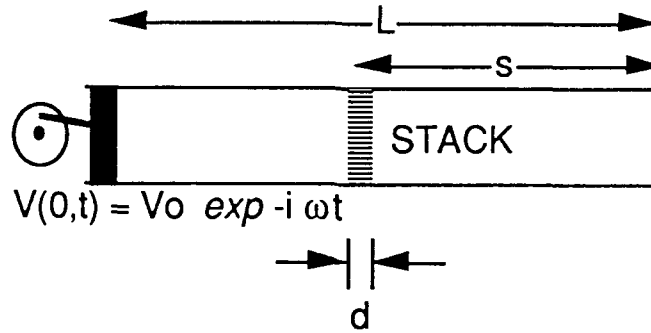

Figure 2.3 Arrangement for the short stack approximation.

After some manipulation, work flow is

$$\bar{W}_2(z) = \frac{A_{res} V_0^2}{2 sin^2(k_0 L)} (\gamma - 1) \rho_0 \omega d \, Im \, F^*(\lambda_T) \, cos^2(k_0 s) \left(1 - \Gamma \frac{Im \{ F^*(\lambda_T)/F^*(\lambda) \}}{Im \, F^*(\lambda_T) (1 - N_{pr})} \right)$$

$$+ \bar{W}_{2visc}(z) \qquad (2.62)$$

where work done on the gas due to viscosity is

$$\bar{W}_{2visc}(z) = \frac{A_{res} V_0^2}{2 sin^2(k_0 L)} \rho_0 \omega d \, sin^2(k_0 s) \frac{Im \, F^*(\lambda)}{F(\lambda) \, F^*(\lambda)} . \qquad (2.63)$$

In the inviscid approximation, work flow is

23

$$\bar{W}_2(z) = \frac{A_{res} V_0{}^2}{2 sin^2(k_0 L)} (\gamma - 1) \rho_0 \omega d \, Im \, F^*(\lambda_T) \, cos^2(k_0 s) \, (1 - \Gamma) \quad . \tag{2.64}$$

Equation (2.62) and Eq. (2.64) are the acoustic power absorbed by the stack and when these quantities are negative, it indicates that acoustic power is being produced by the stack. Just as we saw for heat flow above, stacks made of pores for which $Im \, F^*(\lambda_T)$ is a large value will result in the greatest work flow.

Work and heat flow are to be compared for the various pore geometries shown in Fig. 2.4a-d. In the inviscid short stack approximation, pores with a large value of $Im \, F(\lambda)^*$ will have the greatest heat and work flows as indicated by Eq. (2.60) and Eq. (2.64). According to the results shown in Fig. 2.5, the parallel slit geometry has the largest value of $Im \, F(\lambda)^*$. The value occurs for $\lambda_c \approx 3.2$ which allows one to compute the optimal operating frequency from the relation $\lambda_c = (\rho_0 \omega c_p / \kappa)^{1/2} R$. In other words, you can get about 10% more heat flow and work flow in thermoacoustics just by choosing to make your stack from parallel plates rather than the other pore geometries. The functional form of $F(\lambda)$ for the various pore geometries is given below.

Swift[4] and Rott[5] have worked out the parallel slit geometry stack. Parallel slit porous media has also been of interest in porous media.[11,13] Denote by 2a the separation distance between plates. To be consistent with the definition of the characteristic pore radius R as being equal to twice the transverse pore area divided by the pore perimeter, we take R = 2a. The y axis is centered at the mid-point between plates with the z axis extending in the longitudinal direction. The function $F(y;\lambda)$ which satisfies the differential equation for the transverse dependence of the equation of motion, Eq. (2.12), is

$$F(y;\lambda) = 1 - \frac{cosh(\sqrt{-i} \, \lambda/2 \, y/a)}{cosh(\sqrt{-i} \, \lambda/2)} \quad . \tag{2.65}$$
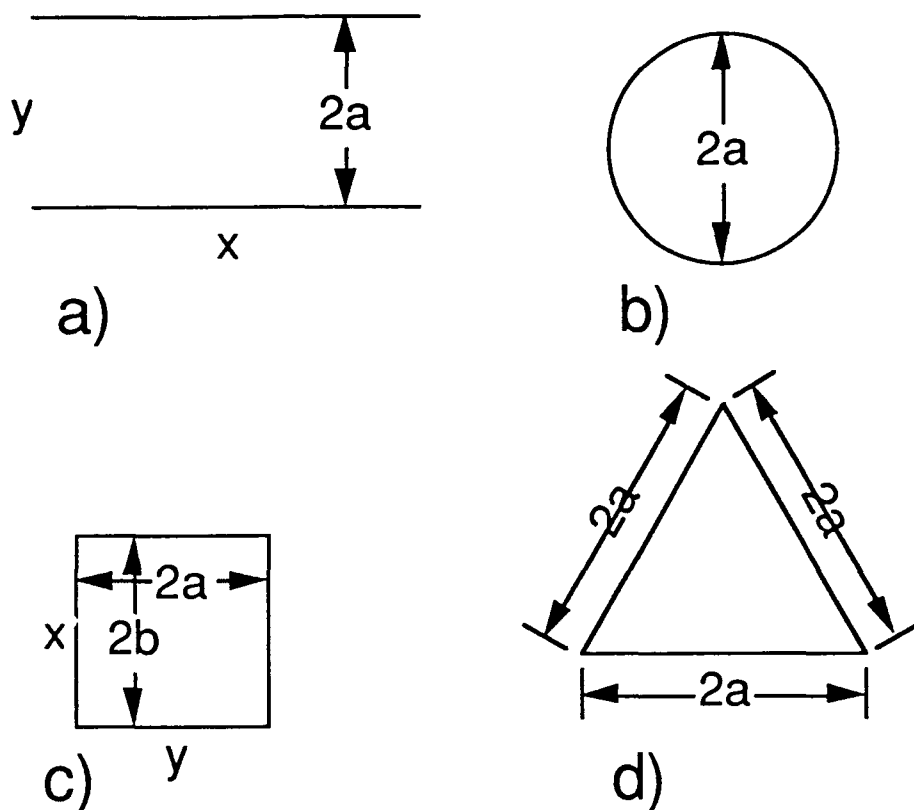
Figures 2.4   (a) Parallel slit, (b) circular, (c) rectangular, and (d) equi-
lateral triangular capillary tube geometries considered for the
short stack approximation. For example, c) corresponds to
the stack shown in Figure 1b.

For the slit, the average of $F(y;\lambda)$ over the pore is defined as $F(\lambda) = 1/(2a) \int F(y;\lambda) \, dy$ and

is

$$F(\lambda) = 1 - \frac{2}{\lambda\sqrt{-i}} \, tanh(\sqrt{-i}\,\lambda/2)) \quad . \tag{2.66}$$

Rott has worked out the cylindrical pore[1] geometry stack. One type of porous media

theory is based upon propagation in a single cylindrical cylindrical capillary tube.[10,11]

Denote by a the radius of the cylindrical pore. The characteristic pore radius for cylindrical

pores is R = a. The radial coordinate of a cylindrical coordinate system centered at the

middle of the circular pore is r. The function $F(r;\lambda)$ which satisfies the differential equation

for the transverse dependence of the equation of motion, Eq. (2.12), is
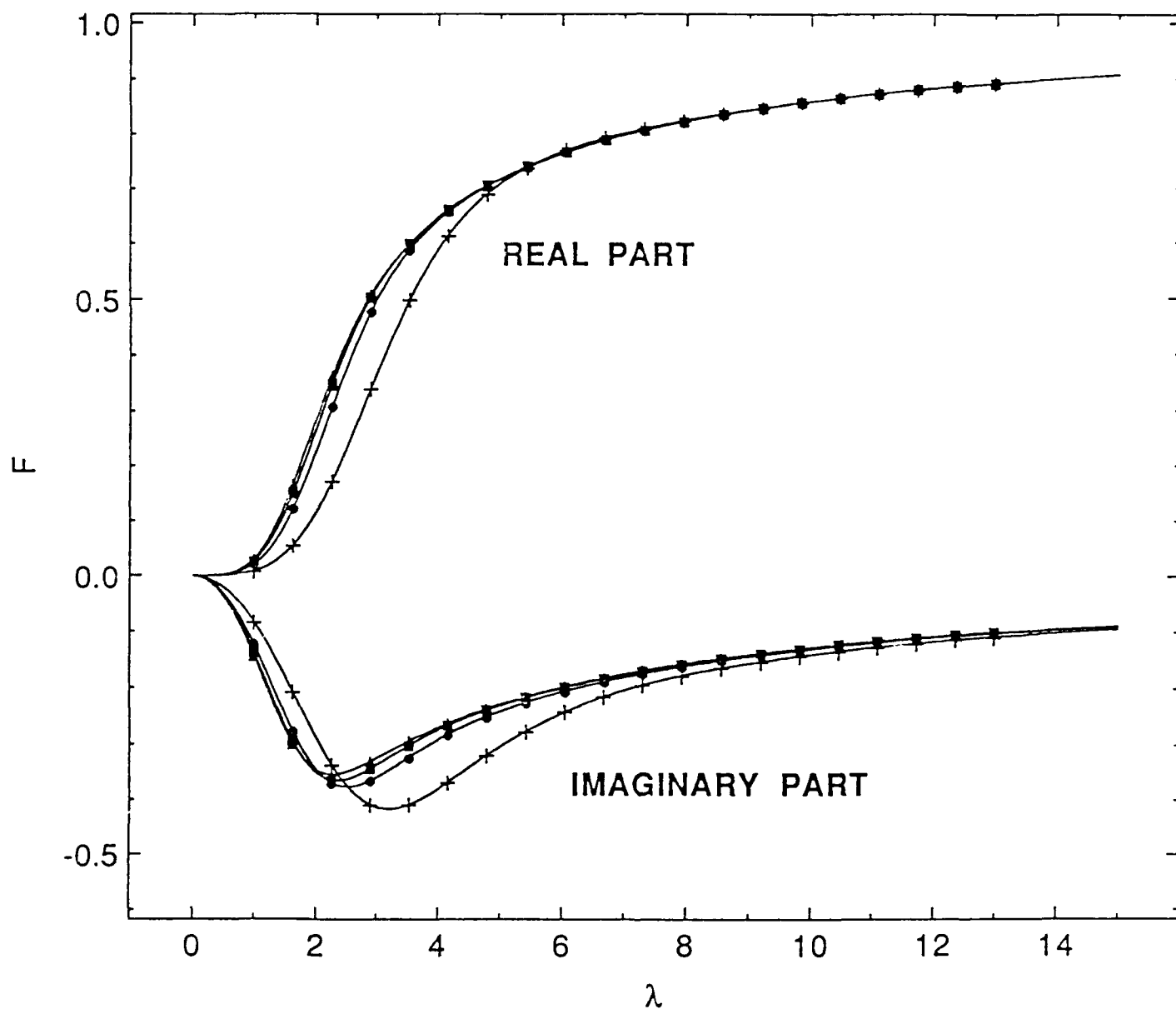
Figure 2.5   Real and imaginary part of the $F(\lambda_T)$ for parallel slits (+), circular pores (closed circles), square pores (closed squares), and equilateral triangular pores (closed triangles). Heat flow is proportional to the imaginary part of $F^*(\lambda_T)$ in the short stack approximation. Parallel slit stack geometry is the best choice for optimizing heat flow.

26

$$F(r;\lambda) = 1 - \frac{J_0(\sqrt{i}\,\lambda\,r/a)}{J_0(\sqrt{i}\,\lambda)} \quad . \tag{2.67}$$

The average of $F(r;\lambda)$ over the pore is defined as $F(\lambda) = 2/a^2 \int F(r;\lambda)\,r\,dr$ and is

$$F(\lambda) = 1 - \frac{2}{\sqrt{i}\,\lambda}\,\frac{J_1(\sqrt{i}\,\lambda)}{J_0(\sqrt{i}\,\lambda)} \quad . \tag{2.68}$$

Previous work has emphasized thermoacoustic stacks consisting of parallel slit pores and cylindrical pores. The basic equations are given here for stacks consisting of rectangular pores. Rectangular pores offer a much wider range of applicability than do parallel slits or cylindrical pores.[7] In addition, we anticipate using square pore ceramic material in a thermoacoustic refrigerator. Denote by 2a and 2b the length along the x axis and y axis of the rectangular pore cross section. We take the coordinate system origin to be at the lower left corner of the rectangular pore. It is convenient to define a function $Y_{mn}(\lambda)$ as

$$Y_{mn}(\lambda) = 1 + \frac{i\pi^2}{\lambda^2}\,\frac{b^2 m^2 + a^2 n^2}{(a+b)^2} \quad . \tag{2.69}$$

The characteristic transverse dimension equal to twice the pore area divided by the pore perimeter is

$$R = \frac{2ab}{a+b} \quad . \tag{2.70}$$

A series solution for the function $F(x,y;\lambda)$ which satisfies the differential equation for the transverse dependence of the equation of motion, Eq. (2.12), is

$$F(x,y;\lambda) = \frac{16}{\pi^2} \sum_{m\ n\ odd} \frac{sin(m\pi x/2a)\ sin(n\pi y/2b)}{m\ n\ Y_{mn}(\lambda)} \quad . \tag{2.71}$$

In all sums given in this section, m and n extend over positive odd integers. For a rectangular pore the average is defined by $F(\lambda) = 1/(4ab) \int F(x,y;\lambda)\ dx\ dy$, where the integral extends over the entire cross section of the pore.

$$F(\lambda) = \frac{64}{\pi^4} \sum_{m\ n\ odd} \frac{1}{m^2\ n^2\ Y(\lambda)} \quad . \tag{2.72}$$

We obtained $F(x,y;\lambda)$ in Eq. (2.71) from a solution by Han[14] for the same differential equation as Eq. (2.12).

The solution for equilateral triangular pores has been recently reported by Stinson.[15] The pore geometry is shown in Fig. 2.4d. The characteristic dimension is $R = a / 3^{1/2}$ and

$$F(\lambda) = 1 - \frac{2}{\sqrt{-i}\ \lambda}\ coth\left(\frac{3\ \lambda\ \sqrt{-i}}{2}\right) + \frac{4\ i}{3\ \lambda^2} \quad . \tag{2.73}$$

2.4 Conclusion

Assume that one can compute $F(x,y;\lambda)$ from Eq. (2.12) and the boundary condition $F(x,y;\lambda) = 0$ for x and y on the arbitrary pore perimeter, and $F(\lambda)$ by averaging this function over the pore cross-sectional area. All first order acoustical field quantities (Sec. 2.2A-D) and the second order energy flux (Sec. 2.2F) can be computed from this function and its companions $F(x,y;\lambda_T)$ and $F(\lambda_T)$. This general framework was used in Sec. 2.3 to investigate the optimal choice of capillary tube geometry for stacks. In the inviscid, short stack approximation, the parallel slit stack geometry is best for maximizing heat and work flow.

28

Impedance and pressure translation theorems were developed in Sec. 2.2E for determining these quantities at all points in the resonator shown in Fig. 2.1a. With this approach, analysis of complicated arrangements of thermoacoustic elements can be evaluated readily and in a unified manner. Work and heat flows were expressed in terms of specific acoustic impedance and pressure to take advantage of these theorems.

Finall;, the function $F(\lambda)$ is also the key element of capillary-pore based porous media models.[10,11,13] Factors are used in these models to scale properties of random media to circular pores. Thus the scaling factors and methodology of porous media modeling can be readily adapted to be useful in thermoacoustics. Afterall, thermoacoustic elements are nothing more than sections of a porous media, with the added complication of temperature gradients.

2.5 Acknowledgements

2.6 References

1. N. Rott, "Thermoacoustics," Adv. Appl. Mech. **20**, 135-175 (1980).

2. P. Merkli and H. Thomann, "Thermoacoustic effects in a resonance tube," J. Fluid Mech. **70**, 161-177 (1975).

3. N. Rott and G. Zouzoulas, "Thermally driven acoustic oscillations. Part IV. Tubes with variable cross-section." Z. Angew. Math. Phys. **27**, 197-224 (1976).

4. G. W. Swift, "Thermoacoustic engines," J. Acoust. Soc. Am. **84**, 1145-1180 (1988).

5. N. Rott, "Damped and thermally driven acoustic oscillation in wide and narrow tubes," Z. Angew. Math. Phys. **20**, 230-243 (1969).

6. The ceramics are manufactured by Corning Incorporated, Industrial Products Division, Corning, New York, 14831.

7. H. S. Roh, W. P. Arnott, J. M. Sabatier, R. Raspet, "Measurement and calculation of acoustic propagation constants in arrays of small air-filled rectangular tubes," to appear in J. Acoust. Soc. Am.

8. A. L. Fetter and J. D. Walecka, *Theoretical Mechanics of Particles and Continua* (McGraw-Hill, New York, 1980).

9. H. Tijdeman, "On the propagation of sound waves in cylindrical tubes," J. Sound Vib. **39**, 1-33 (1975).

10. C. Zwikker and C. Kosten, *Sound Absorbing Materials* (Elsevier, Amsterdam, 1949).

11. K. Attenborough, "Acoustical characteristics of porous materials," Physics Reports **82**, 179-227 (1982).

12. A. D. Pierce, *Acoustics: An Introduction to Its Physical Principles and Applications* (American Instutue of Physics, New York, 1989).

13. M. A. Biot, "Theory of propagation of elastic waves in a fluid-saturated porous solid," J. Acoust. Soc. Am. **28**, 168-191 (1956).

14. L. S. Han, "Hydrodynamic entrance lengths for incompressible laminar flow in rectangular ducts," J. Appl. Mech. **27**, 403-409 (1960).

15. M. R. Stinson and Y Champoux, "Assignment of shape factors for porous materials having simple pore geometries," J. Acoust. Soc. Am. Suppl. 1 **88**, S121 (1990).

3.0 DESIGN OF A THERMOACOUSTIC HEAT ENGINE

The design of the thermoacoustic engine involves the development of criteria for the following elements:

1. Tube length and operating frequencies
2. Heat exchangers
3. Stack
4. Driver
5. Gas handling system
6. Fluid flow system
7. Temperature measurements
8. Assembly

In the following we outline the design criteria for tube length and operating frequencies and the design of the heat exchangers.

3.1. Spacing of plates in the stack and the gas and ambient pressure and temperature combine to give the operating frequency and resonator tube length for the thermoacoustic refrigerator.

In Fig. 3.1, a is the semiwidth of each square of the ceramic material and $\delta_\kappa = [2 \kappa/(\rho_0 c_p \omega)]^{1/2}$ is the thermal penetration depth which is roughly the distance heat can diffuse through the fluid in time $1/\omega$. Here gas properties are κ = thermal conductivity, ρ_0 = ambient gas density, and c_p is the constant pressure heat capacity per unit mass. ω is the radian frequency. The thermal diffusivity of the gas is $K = \kappa / \rho_0 c_p$. The condition on δ_κ and 2a shown in Fig. 3.1 was taken from Ref. 1, pg. 1157 above Eq. (60) and will be used as the design criteria. The operating frequency f for a square pore stack thus is obtained from $a = 3\delta_\kappa$ or

$$f = \frac{9 \kappa}{\pi a^2 \rho_0 c_p} = \frac{9 \eta}{N_{pr} \pi a^2 \rho_0} \qquad . \tag{3.1}$$

31
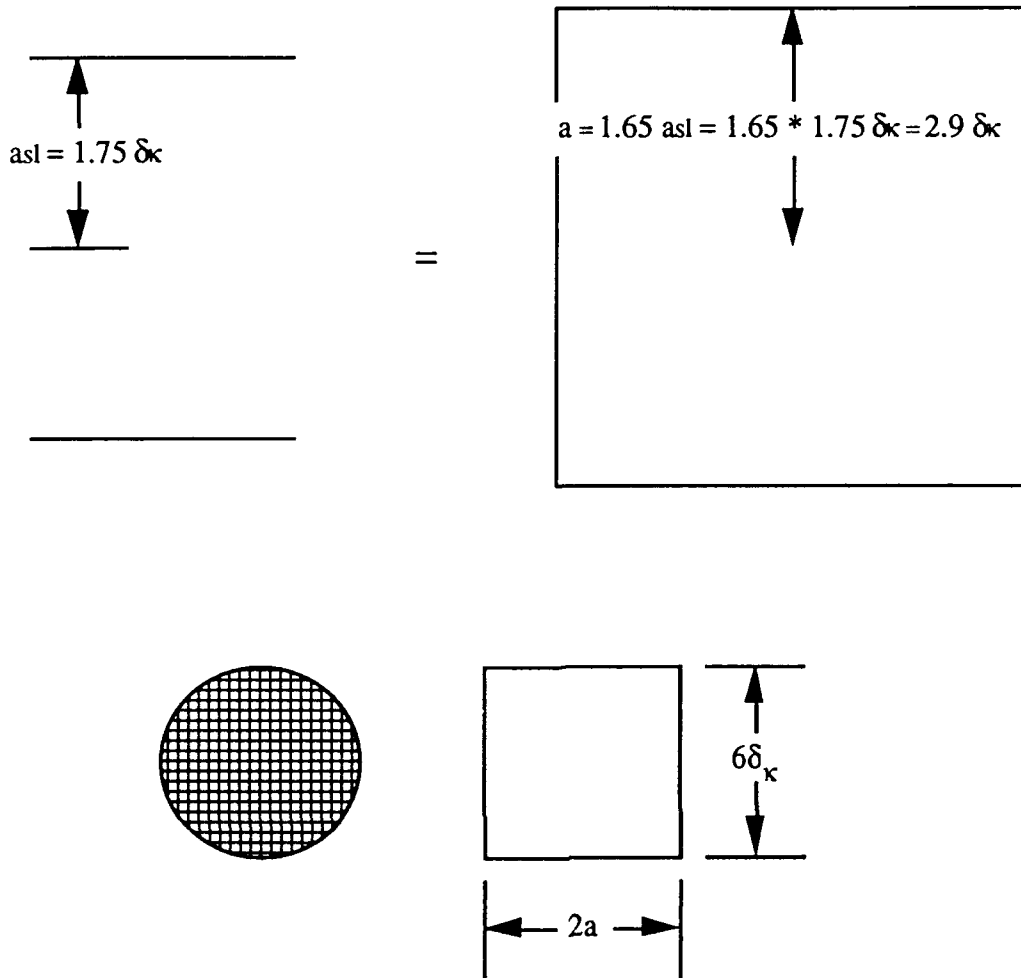
Figure 3.1   Parallel slits of semiwidth a used by Swift are roughly acoustically equivalent to square of semiwidth 1.65a. Requirements on boundary layer thickness and semiwidth are shown.

Gas density, pressure, and temperature are related by the ideal gas relation

$$\rho = \frac{p}{T\,R/\mu_{mw}} \quad , \tag{3.2}$$

where $R = 8.3143$ joules mole^{-1} Kelvin^{-1} is the gas constant and μ_{mw} i s the average molecular weight in kilograms / mole and for Helium (Argon) $\mu_{mw} = 4/1000\ (40/1000)$

kilograms / mole. For a monatomic gas $c_p = (5/2) R / \mu_{mw}$. From Ref. 2, pg 230-231, viscosity of Helium and other monatomic gases follows

$$\eta = \eta' \ (T/T')^s \quad , \tag{3.3}$$

where for Helium (Argon) we may take $\eta' = 1.887 * 10^{-5} \ (2.117 * 10^{-5})$ Pa sec for $T' = 273.15$ Kelvin and $s = 0.6567 \ (0.811)$ for the temperature range 33.15 Kelvin to 1073.15 Kelvin (293 to 373 Kelvin). For a monatomic gas the Prandtl number is (see Susalla's thesis, Ref. 3, and references therein) $N_{pr} = \eta \ c_p / \kappa = 2/3$ so we may calculate the thermal conductivity κ as

$$\kappa = \eta \ c_p / N_{pr} = \eta \ (5/2) R / \mu_{mw} / (2/3) = \kappa' \ (T/T')^s \quad , \tag{3.4}$$

where for Helium (Argon) $\kappa' = 0.1471 \ (0.01650)$ Watts / (meter Kelvin) at $T' = 273.15$ Kelvin and $s = 0.6567 \ (0.811)$ for the temperature range 33.15 Kelvin to 1073.15 Kelvin (293 to 373 Kelvin). The sound speed for an ideal gas is given for reference here as

$$c = \sqrt{\frac{\gamma \ R \ T_0}{\mu_{mw}}} = c' \ (T/T')^{0.5} \tag{3.5}$$

where for Helium (Argon) $c' = 972.8 \ (307.6)$ m/s at $T' = 273.15$ Kelvin.

Consideration of the operating frequency for Helium (Argon) gas we have from Eqs. (3.1-3.3)

$$f_{He} \ (f_{Ar}) = \frac{T_0^{1.6567}}{236 \ a^2 \ p_0} \ \left(= \frac{T_0^{1.811}}{5005 \ a^2 \ p_0} \right) , \quad . \tag{3.6}$$

Lets work at an ambient temperature of $T_0 = 300$ K and an ambient pressure $p_0 = 3$ atm $= 3$ atm $* 101325$ Pa / atm $= 303975$ Pa, and use the square pore media having a $= 0.77$ mm so that we get an operating frequency of $f_{He} = 300$ Hz and $f_{Ar} = 34$ Hz. The operating

wavelength is $\lambda_{He} = c / f_{He} = 3.4$ m and $\lambda_{Ar} = c / f_{Ar} = 9.5$. For a pressure maximum at both ends of the tube, $L_{tube} = \lambda_{He} / 2 = 1.7$ m for Helium and $L_{tube} = \lambda_{Ar} / 2 = 4.75$ m for Argon. Tables 3.1 and 3.2 summarizes these results. I recommend using Helium and the criteria given in the table for Helium.

TABLE 3.1 Design Criteria for Helium

QUANTITY	VALUE	CRITERIA
a = semiwidth of pore	0.77 mm	High porosity, several lengths, uniform
p_0 = ambient pressure	3 atm	nominal value = 303975 Pa
T_0 = ambient temp.	300 K	nominal value
ρ_0 = ambient density	0.488 kg / m^3	nominal value
f_{He} = operating freq	300 Hz	Boundary layer thickness = a / 3
c = adia. sound speed	1020 m/s	Ambient temperature
λ_{He} = wavelength	3.4 m = 11'2"	f_{He} and c
$L_{tube} = \lambda_{He} / 2$	1.7 m = 5'7"	operating wavelength, velocity node at each end

TABLE 3.2 Design Criteria for Argon

QUANTITY	VALUE	CRITERIA
a = semiwidth of pore	0.77 mm	High porosity, several lengths, uniform
p_0 = ambient pressure	3 atm	nominal value = 303975 Pa
T_0 = ambient temp.	300 K	nominal value
ρ_0 = ambient density	4.88 kg / m^3	nominal value
f_{Ar} = operating freq	34 Hz	Boundary layer thickness = a / 3
c = adia. sound speed	322.4 m/s	Ambient temperature
λ_{Ar} = wavelength	9.5 m	f_{Ar} and c
$L_{tube} = \lambda_{Ar} / 2$	4.75 m = 15'7"	operating wavelength, velocity node at each end

34

3.2. Heat Exchangers.

Heat carried by the stack is deposited at the ends where it is picked up by the heat exchangers. Design criteria for heat exchangers are as follows:

1. Height H is determined by the peak acoustic displacement in the gas. The acoustic displacement amplitude is roughly $\xi(z) = v_z(z) / -i\omega = p_1(z) / (-i\omega \rho c)$ and hence depends on the driving amplitude. Here ρ and c are complex quantities as a result of dissipation in the stack and velocity should be multiplied by q/Ω where q is tortuosity and Ω is porosity. For a rough estimate of ξ we proceed by supposing $p_1(z) = 0.05 \, p_0 = 15200$ Pa, $\rho_0 = 0.488$ Kg/m^3, c = 1020 m/s, and an operating frequency of 300 Hz to get $\xi = 1.6$ cm.

2. The hot heat exchanger (HHE) is located near a velocity node and the cold heat exchanger (CHE) is closer to a velocity antinode. As commented by Swift in Ref. 1, pg. 1168, the HHE must pick up more heat than the cold and hence it should be larger. Because the HHE is close to a velocity node viscous dissipation will be less than the CHE so the HHE can have a larger H and smaller Ta than the CHE.

Combining 1. and 2. I estimate $H_{HHE} = 2.0$ cm and $H_{CHE} = 1.5$ cm. For the HHE, $T_a = 0.5$ mm and $T_c = 0.25$ mm. For the CHE, $T_a = 0.7$ mm corresponding to the plate spacing in the stack and $T_c = 0.25$ mm. In both the CHE and HHE, T_c is the approximate stack wall thickness also. Referring to Fig. 3.2 the number of each aluminum and copper plates needed is

$$n_{plates} = 160 \text{ mm} / (T_a + T_c) \qquad (3.7)$$

where T's are the thickness of the aluminum and copper plates. For the CHE this gives $n_{plates} = 170$ and for the HHE $n_{plates} = 215$. If we close every 10 channel to flow fluid through as indicated by the closed channels in Fig. 3.2, the number of open plates is $n_{open} = n_{plates} * 0.9$. Hence the porosity is

$$\Omega = T_a * 0.9 \, n_{plates} / 160 \text{ mm} \qquad (3.8)$$

35

HEAT EXCHANGERS

SIDE VIEW BEFORE ELECTROPLATING

16 cm

COPPER
THICKNESS
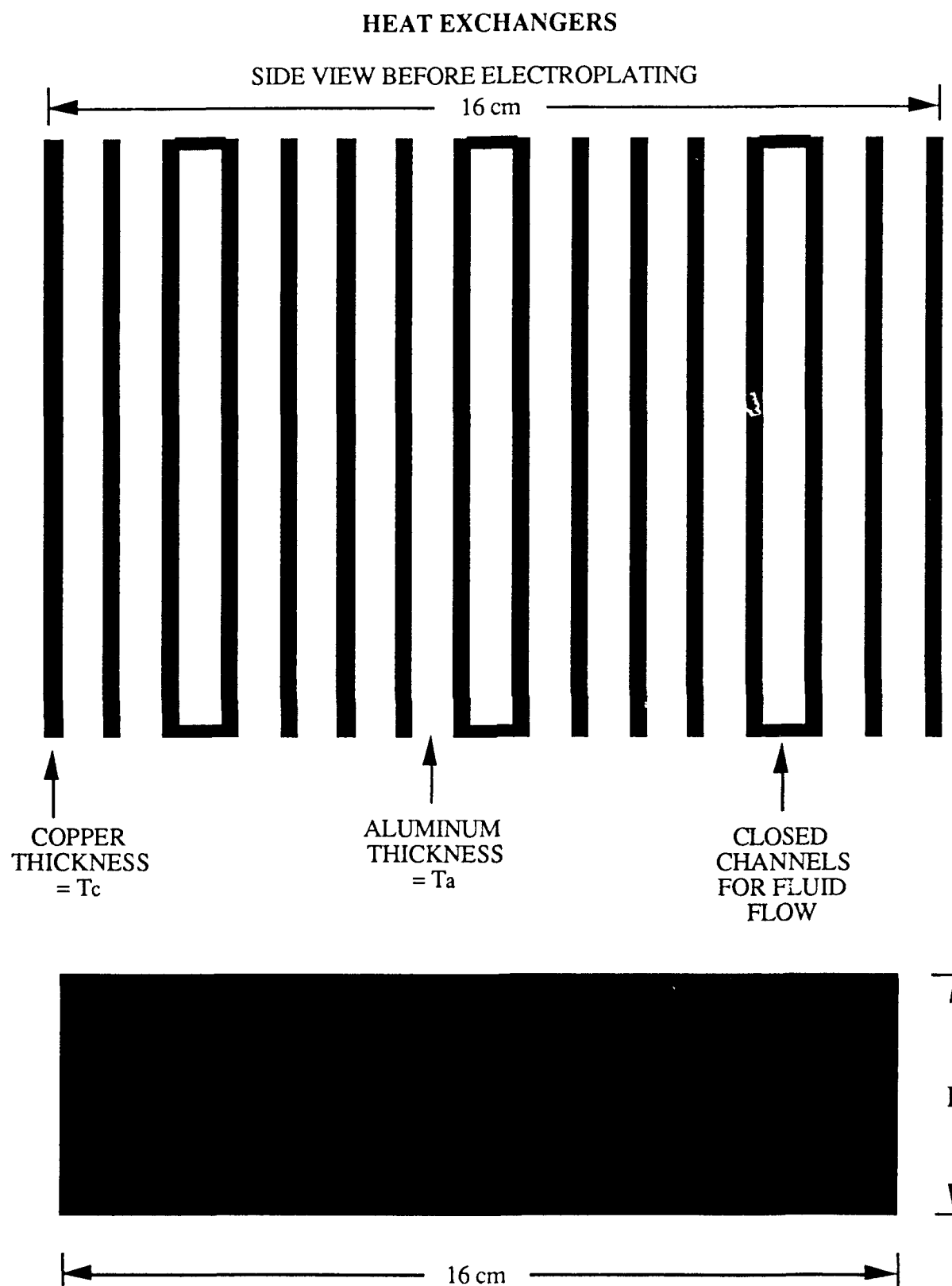= Tc

ALUMINUM
THICKNESS
= Ta

CLOSED
CHANNELS
FOR FLUID
FLOW

16 cm

Figure 3.2. Heat exchangers before electroplating.

and gives $\Omega_{CHE} = 0.67$ and $\Omega_{HHE} = 0.60$. By comparison the stack porosity is $\Omega_{STACK} = 0.73$. Table 3.3 summarizes the geometry of the HE's. Table 3.4 summarizes the number of 2'X4' sheets of aluminum and copper needed. Heat exchangers are made by the following steps:

1. Obtain aluminum and copper plates of the dimensions given in Table 2.1. Epoxy these plates together as indicated in Fig. 2. The aluminum plate at the tenth slot will have a height of $H_{al} = H - 16T_c = H - 4$ mm so that a channel can be formed through which fluid or heating wires may run.

2. Machine the composite to the form shown in Fig. 3.3 after the epoxy has dried.

3. Electroplate the machined exchangers with copper.

4. Machine the top and bottom of the exchangers until the aluminum just shows in the open channels. Do not machine open the closed channels.

5. Observing the locations of the closed channels, go to the side and machine through the electroplate to expose the aluminum. There will be 2 mm on top and bottom of the closed channels that are electroplate so be careful not to remove it.

6. The exchanger is ready to be dumped into an acid bath to remove the aluminum. Presumably the acid bath will put the aluminum into solution, leaving the copper relatively unharmed.

TABLE 3.3 Heat exchanger geometries in Metric and English Units.

Heat Exch.	H	H_{al}	T_a	T_c	n_{plates}	$n_{alshorts}$	Ω
	(mm)	(mm)	(mm)	(mm)			
COLD CHE	15	11	0.7	0.25	170	17	0.67
HOT HHE	20	16	0.5	0.25	215	22	0.60

Heat Exch.	H	H_{al}	T_a	T_c	n_{plates}	$n_{alshorts}$	Ω
	$(10^3 in)$	$(10^3 in)$	$(10^3 in)$	$(10^3 in)$			
	(mils)	(mils)	(mils)	(mils)			
COLD CHE	591	433	28	10	170	17	0.67
HOT HHE	787	630	20	10	215	22	0.60

TABLE 3.4 Number of 2' by 4' sheets of Al and Cu needed for 3 sets of HE's.

Heat Exch.	#20 mil Al	#28 mil Al	# 10 mil Cu
	2' X 4' sheets	2' X 4' sheets	2' X 4' sheets
CHE		3	3
HHE	3		3
TOTALS	3	3	6

|◄————————— 14.6 cm ————————►|
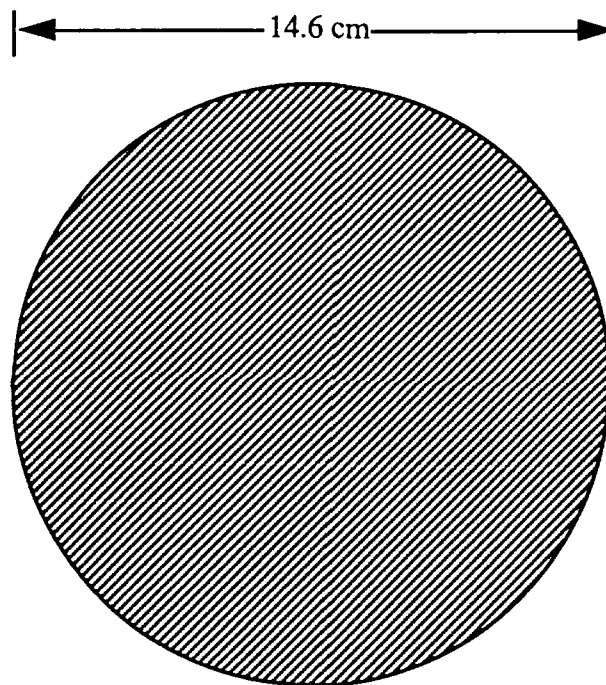
TOP VIEW AFTER MACHINING AND ELECTROPLATING:
SOME CHANNELS ARE CLOSED TO ALLOW FOR FLUID FLOW
OR FOR INSERTION OF HEATING WIRES

Figure 3.3. Top view of heat exchangers after electroplating and machining.

3.3 References

1. G. Swift, "Thermoacoustic engines," J. Acoust. Soc. Am **84**, 1145-1180, (1988).

2. S. Chapman, and T. Cowling, *The Mathematical Theory of Non-Uniform Gases*, (Cambridge, London, 1969).

3. M. P. Susalla, "Thermodynamic improvements for the space thermoacoustic refrigerator (star)," Master Thesis, Naval PostGraduate School, June 1988.

Appendix A:

Publication Patents/Presentations/Honors Report

OFFICE OF NAVAL RESEARCH
PUBLICATIONS/PATENTS/PRESENTATIONS/HONORS REPORT
1 Oct 89 through 30 Sept 90

R&T Number: N00014-89-J3087

Contract/Grant Number: 30-0220384142

Contract/Grant Title: Theoretical and Experimental Study of Thermoacoustic Engines

Principal Investigator: Richard Raspet

Mailing Address: University of Mississippi
         Department of Physics and Astronomy
         University, MS 38677

Phone Number: (with Area Code) (601) 232-5840

E-Mail Address: PAARNOTT at UMSVM (Bitnet)

a. Number of Papers Submitted to Refereed Journal but not yet Published: ___2___

    "Development of Nonlinear Waves in a Thermoacoustic Prime Mover", submitted to Proceedings of the 12th International Symposium on Non-Linear Acoustics, A.A. Atchley, H.E. Bass, and T.J. Hufler, 27-31 August 1990, Austin Texas.

    "Measurements and Calculation of Acoustic Propagation Constants in Arrays of Small Air-Filled Rectangular Tubes", acepted to J. Acoust. Soc. Am., __87__, (S1) May 90.

b. Number of Papers Published in Refereed Journals: ___0___
    (list attached)

c. Number of Books or Chapters Submitted but not yet Published: ___0___

d. Number of Books or Chapters Published: ___0___
    (list attached)

e. Number of Printed Technical Reports & Non-Refereed Papers: ___1___
    (list attached)

    "Study of a Parallel Slit Thermoacoustic Prime Mover"
f. Number of Patents Filed: ___0___

g. Number of Patents Granted: ___0___

h. Number of Invited Presentations at Workshops or Prof. Society Meeting: ___0___

i. Number of Presentations at Workshops of Prof. Society Meetings: ___2___
    "Sound Propagation in Capillary-Tube-Type Porous Media with Much Smaller Pores in the Capillary Walls", to ASA Conference Fall of 1990.

    General Formulation of Thermoacoustics for Stacks having Arbitrarily-Shaped Pore Cross-Sections", to ASA Conference Fall of 1990.

j. Honors/Awards/Prizes for Contract/Grant Employees:
    (list attached, this might include Scientific Soc Awards/Offices, Promotions, Faculty Awards/Office etc)

k. Total number of Graduate Students and Post-Doc Supported at least 25% this year on this contract/grant:

Grad Students _3_ and Post-Doc _1_ including
Grad Students Female _____ and Post-Doc Female _____
Grad Student Minority _____ and Post-Doc Minority _____

Minorities include Blacks, Aleuts, AmIndians, Hispanics etc. NB: Asians are not considered an under-represented or minority group in science and engineering.

Dr. L. C. Sutherland   9 July 1990
Associate Editor, Aeroacoustics, Atmospheric Sound
Wyle Laboratories
128 Maryland Street
El Segundo, CA 90245

Dear Dr. Sutherland,

Enclosed you will find three copies of the paper entitled "Measurement and calculation of acoustic propagation constants in arrays of small air-filled rectangular tubes" by H. S. Roh, W. P. Arnott, J. M. Sabatier, and R. Raspet which we would like to submit for publication in JASA. Also enclosed is the signed transfer of copyright. Please address correspondence for this paper to W. Pat Arnott, P.O. Box 847, University, MS, 38677.

We have been attempting to verify ground impedance models by considering ideal porous materials. This paper is about that work. Critical reviewers of this work might be Mike Stinson and others at NRC, Ottawa, and Keith Attenborough at the Open University.

Thank you for considering this paper for publication.

Sincerely,

H. S. Roh   J. M. Sabatier

Hun Seol Roh   *J M Sabat*
Graduate Student   Senior Scientist

W. P. Arnott   Richard Raspet

W. Pat Arnott   *Rich Raspet*
Postdoctoral Scientist   Associate Professor

Sound propagation in capillary-tube-type porous media with much smaller pores in the capillary walls. W. Pat Arnott, James M. Sabatier, and Richard Raspet (National Center for Physical Acoustics and the Dept. of Physics and Astronomy, P.O. Box 847, University, MS 38677).

Sound propagation in gas-filled capillary-tube-type porous media was investigated. The capillary tubes were taken to be nominally straight with very small pores in the walls of the capillary tubes. The central assumptions (which are frequency dependent) are that the wall pore diameters are much less than the viscous penetration depth, and that the acoustic pressure in the main pore is only a function of the longitudinal direction. As a consequence of these assumptions, the excess temperature of the gas in the wall pores can be taken as negligible. Walls were taken to be rigid. Propagation constants and the characteristic impedance of such a media were computed. Application to ceramic samples having square capillary pores and porous walls is developed as a possible explanation for the anomalous tortuosity factor previously inferred for this material [H. Roh, et. al., J. Acoust. Soc. Am. Suppl. 1 87, S139 (1990)]. Comparison is made to the theory for sound propagation in ducts having finite impedance walls.

Technical Committee: Physical Acoustics (Special session on Acoustics of fluid-filled porous media.)

Method of Presentation: Lecture

Subject Classification Numbers: 43.20.Hq, 43.28.Fp

Telephone Number: (601) 232-5129

Send Acceptance or Rejection Notice to: W. Pat Arnott

Special Facility: None

General formulation of thermoacoustics for stacks having arbitrarily-shaped pore cross-sections. W. Pat Arnott, Henry E. Bass, and Richard Raspet (National Center for Physical Acoustics and the Dept. of Physics and Astronomy, P.O. Box 847, University, MS 38677).

Previous theoretical results in thermoacoustics have been developed for stacks with circular pore [Rott, Adv. Appl. Mech. 20, 135-175 (1980)] or parallel slit [G. W. Swift, J. Acoust. Soc. Am. 84, 1145-1180 (1988)] geometries. We have developed a general linear formulation for gas-filled stacks having pores of arbitrary cross-sectional geometry. For compactness in the following, denote by F the functional form of the transverse variation of the longitudinal particle velocity. F generally is a function of the transverse coordinates, frequency, pore geometry, the response functions and transport coefficients of the gas used, and the ambient value of the gas density. We show how one may obtain expressions for the acoustic temperature, density, particle velocity, pressure, energy flux, and work flux from knowledge of F. Results are displayed for the special case of stacks having rectangular pore geometries. This analysis will be used as an aid in the design of an thermoacoustic engine with a stack having square pore geometries. Comparison is made to capillary-pore-based porous media theories. [Work supported by ONR].

Technical Committee: Physical Acoustics

Method of Presentation: Lecture

Subject Classification Numbers: 43.35.Ud (Special Session on Thermoacoustics.)

Telephone Number: (601) 232-5129

Send Acceptance or Rejection Notice to: W. Pat Arnott

Special Facility: None

Appendix B:

Status Report

A Theoretical and Experimental Study of

Thermoacoustic Engines

Richard Raspet

Status Report

Graduate Students
James Belcher, MS. student in progress
Janxing Tan, PhD. student in progress

Post Graduate Research Associate
William Pat Arnott, PhD.,Washington State University

Other Government Sponsored Research
Richard Raspet is principal investigator for a MIT Lincoln Laboratory grant of $80k for investigation of wind noise.

Henry E. Bass is principal investigator for NASA-Sonic Boom grant of $225k for research in atmospheric acoustics.

Status of contract funds as of 1 September 1990

$138,957.97 has been expended and $11,610.00 has been encumbered for equipment for a total of $150,567.97 out of the $160,000 budgeted. $4778.49 has been spent on travel; $4200 was budgeted. We have spent more money on equipment than was anticipated and will be requesting a budget revision from ONR. $17,194 was budgeted; we spent $25,973.25 during the first year of the contract.

Permanent Equipment Purchased

HP-3457A	Multimeter	$2,767.50
HP-44492A	Multiplexer Cord for HP-3457A	486.00
HP-35660A	Dynamic Signal Analyzer	11,610.00
HP-8904A	Multifunction synthesizer	4,158.00
HP-3478A	Multimeter	895.00
SR530	Lock-in Amplifier	4,010.00
HP-7475A	6 Pen Plotter	1,421.00
		========
		$25,347.25

46

Appendix C:

Study of a Thermoacoustic Prime Mover Below Onset of Self Oscillation

Study of a thermoacoustic prime mover below onset of self-oscillation.

Anthony A. Atchley, Henry E. Bass, Thomas J. Hofler and Hsiao-Tseng Lin

Physics Department

Naval Postgraduate School

Monterey, CA 93943

Abstract

The frequency response of a thermoacoustic prime mover (consisting of a parallel plate prime mover stack and heat exchangers housed in a resonant tube) has been measured as a function of the mean gas pressure and temperature gradient across the prime mover stack. The frequency response of two simpler resonator configurations was also measured in the absence of an applied gradient. The quality factor Q and resonance frequency can be determined from the response. As the temperature gradient is increased, the Q increases indicating a decrease in attenuation across the stack. At sufficiently large temperature differences (~ 300 K), the resonator goes into self-oscillation indicating negative attenuation. Measurements are reported for the prime mover and the simpler resonators in the absence of a temperature gradient for helium and argon at pressures ranging from 170 - 500 kPa. Measurements are also reported for the prime mover in the presence of temperature gradients, ranging from zero to that required for onset of self-oscillation, for helium at the same pressures. The results are explained in terms of a counterpropagating, plane wave analysis, based on techniques commonly used in porous media investigations. In general, the agreement between theory and experiment is good, especially for the simpler resonator configurations. For the prime mover configuration, there is considerable disagreement between the predicted and measured Q at low temperature gradients.

INTRODUCTION

Swift[1] and others[2,3] have developed theories that can be used to predict the onset of oscillation and the quality factor Q of a thermoacoustic prime mover. Their models are based on a thermodynamic approach that considers energy transfer and dissipation on the exposed surfaces. This treatment agrees with experimental results and includes all the applicable physics. It does have one disadvantage. As formulated, it is not simple to transfer extensive research of the acoustic properties of porous materials to performance predictions of thermoacoustic devices. One goal of this article is to develop such a formalism, which will be especially attractive when considering the use of alternate geometries in the prime mover stack.

In the following, we have attempted to apply the standard treatment of acoustic waves in porous media and propagation in a tube with multiple boundaries to predictions of prime mover performance. Except for one equation for heat flow in the presence of a temperature gradient, all equations and their description can be found in standard acoustics textbooks.[4] As one might expect, all the needed expressions without a temperature gradient can be found in the works of Lord Rayleigh.[5]

I. EXPERIMENTAL APPARATUS AND PROCEDURE

We measured the frequency response of a thermoacoustic prime mover as a function of the mean gas pressure and temperature gradient across the prime mover stack. The quality factor Q and resonance frequency can be determined from the response. The temperature gradients ranged from zero to that required for the onset of self oscillation. To gain confidence in our ability to measure the frequency response, we first measured the response of two simpler resonator

configurations: an empty, rigidly terminated resonant tube, and the empty tube plus the ambient heat exchanger These configurations, and that of the prime mover, are discussed in Section A. Temperature control and measurement are discussed in Section B, followed by a discussion of the data acquisition procedure in Section C.

A. Resonator Configurations

We measured the frequency response of three different resonator configurations: an empty, rigidly terminated resonant tube; the empty tube plus the ambient heat exchanger; and the prime mover. The empty resonator is made from two 3.82 cm ID (inner diameter) copper tubes, separated by a 2.19 cm long brass section having a slightly larger ID. This brass section is called the ambient heat exchanger container. The lengths of the two sections of copper tube are 11.43 cm and 87.95 cm. One end of each section is fitted with a flange that allows them to be soldered to the ambient heat exchanger container. A 0.64 cm thick copper cap is soldered to the other end of each section, forming a closed, rigid, termination. The cap on the longer section houses a 1.9 cm diameter electret driver and a 0.59 cm diameter electret microphone. The driver and microphone are flush mounted and sealed in the end cap with epoxy. The end cap is epoxied to the section of tube. Even with the driver and microphone mounted in the end cap, our measurements show that it still behaves as a rigid termination. The total length of the resonator, including the heat exchanger container, is 101.56 cm (internal dimensions). The resonator is connected to a gas handling system, through a fill tube in the ambient heat exchanger container. This connection allows for evacuation of the resonator before pressurization with gas (helium or argon) and a system vent. A dial pressure gauge and an OMEGA Model PX304-150AV pressure transducer are connected to the fill line to sense the mean pressure inside the tube. The driver input signal is provided by an HP 3325A function generator and amplified by a Techron Model 7520 power amplifier. The microphone output signal is amplified by a preamplifier with a gain of 100.

The second configuration differs from the first only in that the ambient heat exchanger is

50

mounted in the ambient heat exchanger container. The ambient heat exchanger consists of two stacks of parallel plates. Each stack is composed of 25, 0.045 cm thick, 1.02 cm long copper plates. The gap between each plate is 0.104 cm. The two stacks are mounted in a 3.82 cm ID copper tube such that there is a 0.15 cm gap between them. This double stack heat exchanger is not necessary, a single stack would suffice for these measurements. But, the double stack will be needed in a future phase of this research.

The third configuration, the prime mover, differs from the second by replacing the shorter section of copper tube used in the first two configurations with a different section This section consists of a nickel heater section, a nickel hot heat exchanger, and a stainless steel prime mover. It is designed to withstand the high temperatures required to reach onset of self oscillation. The heater section consists of a 3.82 cm ID, 5.762 cm long nickel tube. One end of the tube is rigidly capped and drilled to accommodate a thermocouple probe, used to sense the hot heat exchanger temperature. The hot heat exchanger is mounted at the other end of the heater section. This heat exchanger consists of 25, 0.045 cm thick, 0.762 cm long nickel plates. The gap between each plate is 0.104 cm. Between each plate there are 304 stainless steel spacers, 0.102 cm long and 0.031 cm in diameter. The distance from the closed end of the heater section to the beginning of the hot heat exchanger is 5.58 cm. The prime mover stack consists of 35, 0.28 cm thick 304 stainless steel plates, 3.50 cm long and spaced by 0.077 cm. This stack is housed within a thin walled (0.05 cm thick) stainless steel tube. One end of this stainless steel tube is welded to the nickel tube such that the hot heat exchanger and prime mover stack are in contact. The other end of the stainless steel tube is fitted with a flange so that the entire section can be soldered to the ambient heat exchanger container. Summarizing the prime mover configuration, it consists of a 5.58 cm long nickel tube, a 0.762 cm long hot heat exchanger, a 3.42 cm long prime mover stack, a 2.18 cm long double stack ambient heat exchanger, and an 87.95 cm long copper tube. The total length of the prime mover is 99.9 cm. The configuration is shown in Fig. 1.
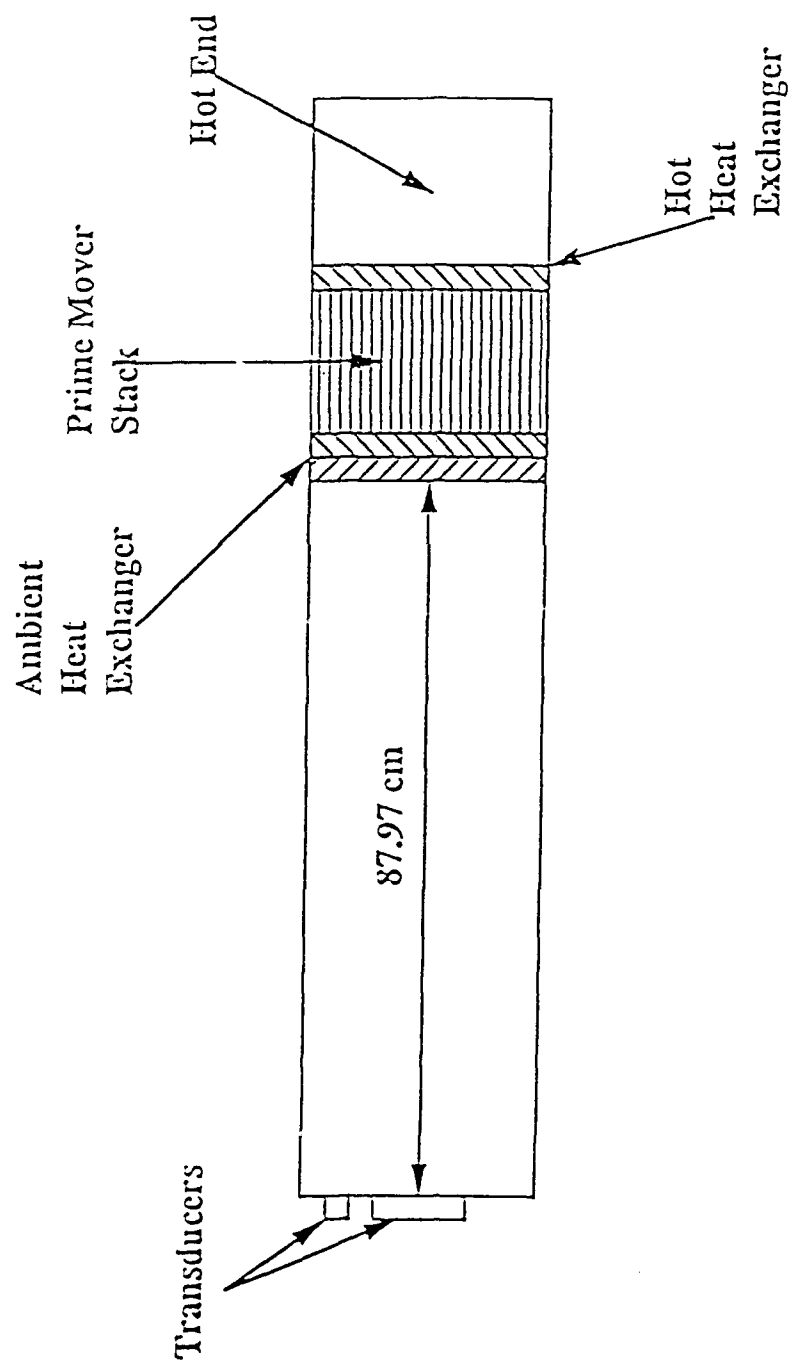
Figure 1: Diagram of the prime mover configuration.

B. Temperature Control and Measurement

The nature of the experiment requires that a temperature difference be established across the prime mover stack and maintained precisely (within 1 K). It is also necessary to eliminate temperature gradients elsewhere in the resonator. Temperature control of the prime mover is achieved as follows. An Omega Engineering Model HBA 202040 nozzle heater surrounds the nickel heater section, or hot end. Electrical power is supplied to the heater through a variable AC transformer. The hot end with its heater is surrounded by insulation to reduce heat loss to the room and to help maintain a uniform temperature distribution along it. The ambient heat exchanger is maintained at near room temperature by circulating water through a jacket which surrounds it. The temperature of the water is maintained with a Neslab Model RET-110 constant temperature bath. After the water leaves the jacket it circulates through flexible plastic tubing that is wrapped around the majority of the length of the longer section of copper tube. This section of tube is also surrounded by styrofoam insulation to help maintain a uniform temperature distribution along its length.

The temperature of the prime mover is monitored by four thermocouples. A type K thermocouple is in contact with the center of the hot heat exchanger to sense the temperature of the hot end. Three type E thermocouples were glued to the top, middle, and bottom of the cold end to sense the temperature along that section. The reference temperature for the whole system is found by using a 4-wire resistance measurement of a thermistor mounted on an aluminum isothermal block. For the first two configurations, the hot end is replaced by the shorter section of copper tube and the type K thermocouple is not used.

C. Data Acquisition

The quality factor of the various resonator configurations is determined by measuring the steady state frequency response. This measurement is accomplished by driving the resonator at frequencies near resonance and measuring the steady state amplitude of the microphone output signal with a Stanford Research Model SR-530 lock-in amplifier. The Q is determined by

performing a least squares fit of the data to the ideal response. Data acquisition is performed by a Standard 286 personal computer. Referring to Fig. 2, the computer communicates with the lock-in amplifier, the HP 3457A digital multimeter and the HP 3325A function generator through a GPIB interface. Through the execution of the controlling program, a source signal is supplied by the function generator to the electret driver. The output voltage from the microphone is amplified by a preamplifier and sent to the lock-in. The output of the lock-in, as well as all other data signals of interest, are fed to an HP 3457A multimeter. The output of the multimeter is recorded by the computer. A Kikusui Model COS6100A oscilloscope is used to monitor the driver input signal and the output signal from the preamplifier.

Before data acquisition is started, the resonator is evacuated and filled with helium or argon to the desired pressure. When data acquisition begins, the program records the mean gas pressure within the resonator. Next, the approximate resonance frequency and the half power bandwidth are entered into the computer, which then determines the start and stop frequencies and the frequency increment. The program sets the driving frequency and measures temperatures, frequency, and the output of the lock-in. The program then increments the frequency and repeats the process. The time required to measure the frequency response is approximately 5 minutes.

The temperature along the length of the resonator is held uniform during the measurements on the first two configurations. For the prime mover configuration, the temperature of the hot end is set by adjusting the electrical power supplied to the heater. After the hot end temperature has reached thermal equilibrium, data acquisition is initiated. The magnitude of the input electrical power is determined by taking the product of the voltage and current. The current is measured through a Tektronix Model P6021 current probe. The heater impedance is almost purely resistive, so there is no need to measure the phase angle between the heater voltage and current.
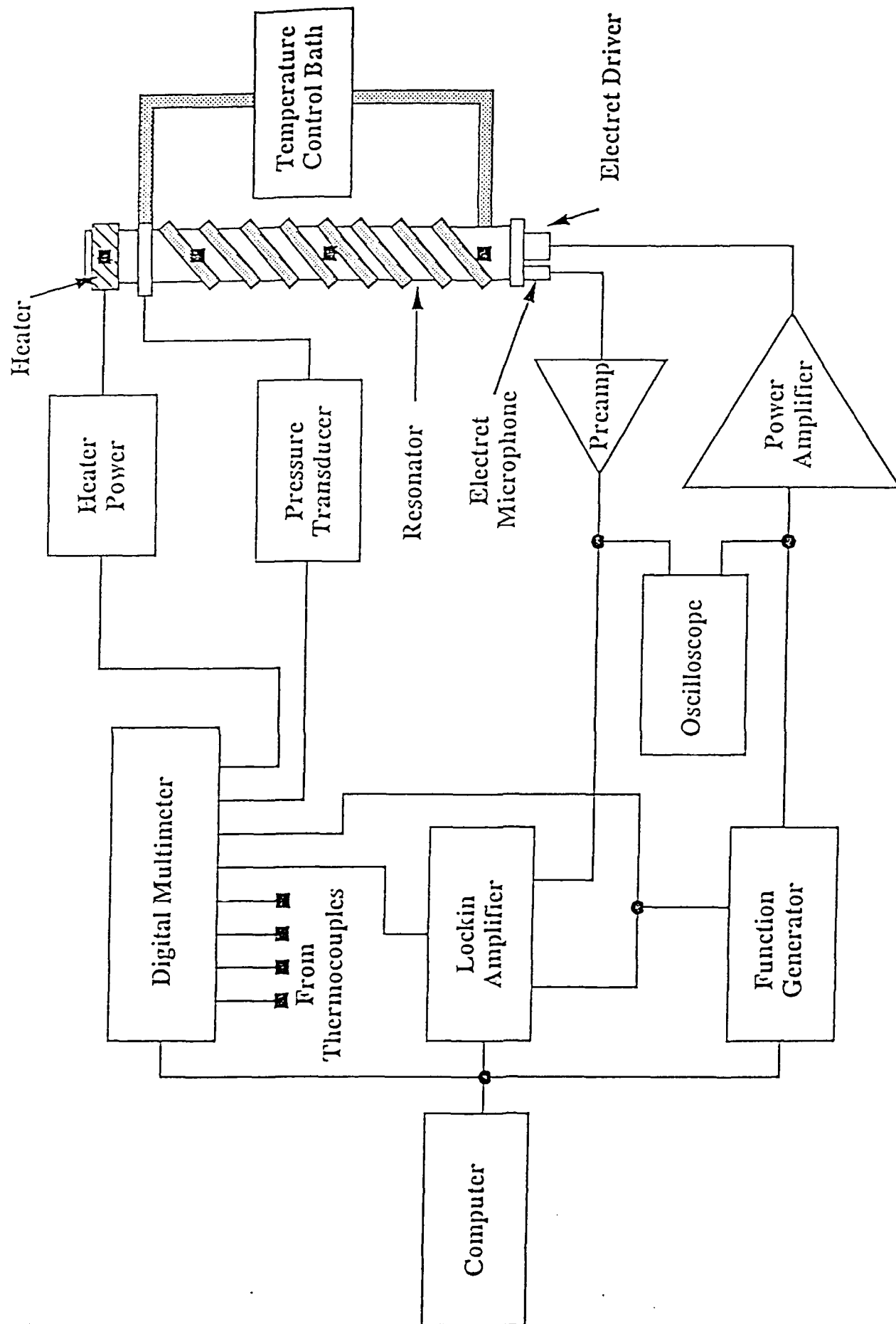
II. RESULTS AND ANALYSIS

Figure 2: Schematic diagram of the instrumentation used in the experiment.

the boundary conditions. We analyze the case of no temperature gradient in Section A below. Except in regions where plates are present, the propagation constants are computed from Shield's work.[6] In the regions where plates are present, the propagation constants are computed from the theory of sound propagation through porous media.[7,9] Pertinent results from porous media theory are discussed in Appendix B. Those unfamiliar with this type of analysis are advised to read Appendix B before proceeding. The case where temperature gradients are present is analyzed in Section B, where we modify the analysis to include the effects of a temperature gradient.

A. Analysis of Data Taken with No Temperature Gradient

In the empty resonator case, we set k_2, z_2, k_3, z_3, k_4, z_4, k_5, z_5 equal to k_1, z_1. k_1 is computed from Shield's work[6] as $k_1 = \omega/c_1 - i\alpha_1$. The impedance z_1 is computed as $z_1 = \omega\rho_0/k_1$. The length of the empty resonator is 1.0156 m. The measured and predicted Q's and resonance frequencies are shown in Table I for the resonator filled with argon and helium at various pressures. The experimental and calculated results are in agreement to within the program's ability to extract f_0 (±0.5 Hz) and Q given the uncertainty in temperature.

For the resonator plus the ambient heat exchanger, l_1 is set at 87.95 cm; l_2 at 90.13 cm. The heat exchanger consists of parallel plates with a gap of 1.02 mm. The porosity is 0.667. Attenborough's theory is used to compute z_2 and k_2. k_3 - k_5 and z_3 - z_5 are set equal to k_1 and z_1, respectively. The tube length is 1.0156 m. Results are shown in Table II. Again experimental and theoretical results are in close agreement. Note that the sign on the error in Q has changed signs for helium suggesting that more viscous attenuation is predicted than actually observed.

Finally, for the case of the prime mover with no temperature gradient, l_3 is set at 93.635 cm, l_4 at 94.397. The full length of the tube is 99.9 cm. The stack consists of parallel plates with a gap of 0.79 mm and a porosity of 0.76. This porosity was multiplied by the factor of open stack area that is blocked by the heat exchanger (0.7) to give an effective porosity of 0.53.

Data was collected for the empty resonator, the resonator with one heat exchanger, and the resonator plus prime mover stack and two heat exchangers. The Q of the resonator was determined by fitting the steady state frequency response to a standard resonance equation

$$A(\omega) = A_{max} / \left[1 + \left(\omega^2/\omega_0^2 \right) Q^2 \left(1 - \omega_0^2/\omega^2 \right)^2 \right]^{1/2}, \tag{1}$$

where ω is the angular frequency of the drive and ω_0 is the resonance angular frequency (frequency of maximum amplitude).

To model the experiment, a closed tube with counterpropagating plane waves is assumed as shown in Fig. 3. In each region, the acoustic pressure of the incident and reflected waves is expressed as $p_i^{(n)} = P_i^{(n)} e^{i(\omega t - kx)}$ and $p_r^{(n)} = P_r^{(n)} e^{i(\omega t + kx)}$, respectively. Continuity of pressure and volume velocity is assumed at each interface. Continuity of volume velocity is written in the form $(P_i^{(1)} - P_r^{(1)})/z_1 = (P_i^{(2)} - P_r^{(2)})/z_2$, where z is called the impedance of the region and defined in Appendix A. At the driving end ($x=0$), $u(0, t) = i\omega l e^{i\omega t}$ where l is the effective driver displacement (assumed to be independent of load). The total complex acoustic pressure at the driving end P_{total} is $P_i^{(1)} + P_r^{(1)}$. The amplitude of the sound at the driving end, where the response is measured, is the absolute value of P_{total}. The expression for P_{total} is derived in Appendix A. As the frequency assumed for the calculation is incremented, P_{total} goes through a maximum giving the resonance frequency f_0. Two methods were used to find the values of Q. From Eq. (1), values of A computed for any two frequencies ω can be used to solve for Q. Values of Q were computed from the amplitudes at adjacent frequency steps for all frequencies near f_0 using Eq. (1) and then averaged. The second method is to compute values of A for frequencies spanning resonance and then perform a least squares fit to Eq. (1) using Q as a one of the parameters.

To calculate P_{total}, all that need be specified are the propagation constants in each region and
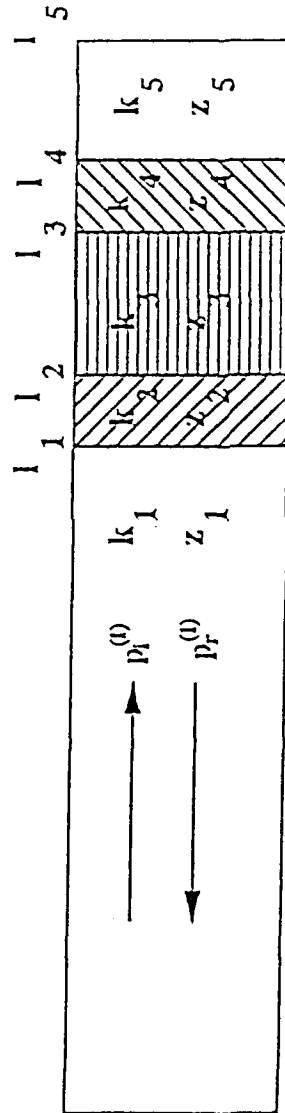
Figure 3: Diagram showing the subdivision of the prime mover used for the counterpropagating plane wave analysis.

Attenborough's theory is again used to compute k_3 and z_3. Results are shown in Table III.

B. Analysis of Data for a Prime Mover Below Onset

The expressions for the propagation constant and impedance derived in Appendix B must be altered when temperature gradients are present. To find these new expressions, we take the same approach as in Appendix B. The only difference being that we use a theoretical approach presented by Swift[1] to solve for the acoustic velocity and temperature distribution across a slit in the presence of a temperature gradient. Using these results, we find expressions for the complex density and compressibility and finally k and z. Once we have k and z we can find P_{total}.

The complex density is the same as that derived for the no temperature gradient case and derived in Appendix B. The result is

$$\rho_c = \rho_f \left(1 - \frac{\tanh\left[(1+i)a/\delta_v\right]}{(1+i)a/\delta_v} \right)^{-1}.$$ (2)

Swift writes for the appropriate heat balance equation,

$$\rho_f c_p \left(i\omega\theta + u_1 \frac{dT_m}{dx} \right) - i\omega\, T_m \beta p = \lambda_h \frac{\partial^2\theta}{\partial y^2}.$$ (3)

where ρ_f is the density of the gas; c_p the isobaric specific heat capacity (per unit mass), θ the variation in temperature due to the acoustic wave, u_1 the acoustic velocity in the direction of propagation, dT_m/dx the temperature gradient across the stack, T_m the mean temperature, β the coefficient of volume expansion, p the acoustic pressure, and λ_h the coefficient of thermal conduction. Again from Swift,

$$u_1 = \frac{i}{\omega \rho_f} \frac{dp}{dx} \left(1 - \frac{\cosh\left[(1+i)y/\delta_v\right]}{\cosh\left[(1+i)a/\delta_v\right]} \right).$$ (4)

Substituting this expression for u_1 into Eq. (3) gives

$$\rho_f c_p \left\{ i\omega\theta + \frac{i}{\omega\rho_f} \frac{dp}{dx} \left(1 - \frac{\cosh\left[(1+i)y/\delta_v\right]}{\cosh\left[(1+i)a/\delta_v\right]} \right) \frac{dT_m}{dx} \right\} - i\omega \, T_m \beta p = \lambda_h \frac{\partial^2 \theta}{\partial y^2},$$ (5)

where $\delta_v = (2\omega/v)^{1/2}$; v is the kinematic viscosity; and a is the semi-width of the slit. Swift identifies a solution

$$\theta = \frac{T_m \beta}{\rho_f c_p} p - \frac{1}{\rho_f \omega^2} \left(1 - \frac{\sigma \cosh\left[(1+i)y/\delta_v\right]}{(\sigma-1) \cosh\left[(1+i)a/\delta_v\right]} \right) \frac{dp}{dx} \frac{dT_m}{dx}$$

$$- \left[\frac{T_m \beta}{\rho_f c_p} p + \frac{(dp/dx)(dT_m/dx)}{(\sigma-1)\rho_f \omega^2} \left(1 + \frac{\varepsilon_s f_v}{f_k} \right) \right] \frac{\cosh\left[(1+i)y/\delta_k\right]}{(1+\varepsilon_s)\cosh\left[(1+i)a/\delta_k\right]},$$ (6)

where $\sigma = v/\kappa_f$ is the Prandtl number, and the other new terms are defined in Table IV. As explained in Appendix B, the condensation of the gas in the slit can be expressed as

$$s = p/p_m - \theta/T_m.$$ (7)

Substituting Eq. (6) into Eq. (7), factoring out $p/\gamma p_m$, setting $T_m \beta = 1$, and recognizing that $p_m/\rho_f c_p T_m = (\gamma - 1)/\gamma$ for an ideal gas, gives

$$s = \frac{p}{\gamma p_m} \left\{ 1 + (\gamma - 1) \frac{c_p}{\omega^2} \frac{\partial p/\partial x}{p} \frac{\partial T_m}{\partial x} \left[1 + \left(1 - \frac{\varepsilon_s f_v}{(\sigma - 1) f_k} \right) \frac{\cosh\left[(1+i)y/\delta_k\right]}{\cosh\left[(1+i)a/\delta_k\right]} \right] + (\gamma - 1) \frac{\cosh\left[(1+i)y/\delta_k\right]}{\cosh\left[(1+i)a/\delta_k\right]} \right\}.$$ (8)

Integrating the condensation across the slit gives

60

$$\bar{s} = \frac{p}{\gamma P_m}\left\{1 + (\gamma - 1)\frac{c_p}{\omega^2}\frac{\partial p/\partial x}{p}\frac{\partial T_m}{\partial x}\left[1 + \left(1 - \frac{\varepsilon_s f_v}{(\sigma - 1) f_\kappa}\right)\frac{\tanh\left[(1 + i)a/\delta_\kappa\right]}{(1 + i)a/\delta_\kappa}\right] + (\gamma - 1)\frac{\tanh\left[(1 + i)a/\delta_\kappa\right]}{(1 + i)a/\delta_\kappa}\right\}. \quad (9)$$

We use Zwikker and Kosten's [9] definition of complex compressibility ($C(\omega) = \bar{s}/\bar{p} = \bar{s}/p$) to get

$$C(\omega) = \frac{1}{\gamma P_m}\left\{1 + (\gamma - 1)\frac{c_p}{\omega^2}\frac{\partial p/\partial x}{p}\frac{\partial T_m}{\partial x}\left[1 + \left(1 - \frac{\varepsilon_s f_v}{(\sigma - 1) f_\kappa}\right)\frac{\tanh\left[(1 + i)a/\delta_\kappa\right]}{(1 + i)a/\delta_\kappa}\right] + (\gamma - 1)\frac{\tanh\left[(1 + i)a/\delta_\kappa\right]}{(1 + i)a/\delta_\kappa}\right\}. \quad (10)$$

For plane traveling waves, $\partial p/\partial x \approx \pm ik(T_m)p$. Assuming that the imaginary part of the propagation constant is small compared to the real part, $k(T_m) \approx \omega/c(T_m)$, and $(\partial p/\partial x)/p \approx \pm i\omega/c(T_m)$. Under these conditions Eq. (10) becomes

$$C(\omega) = \frac{1}{\gamma P_m}\left\{1 \pm i\ (\gamma - 1)\frac{c_p}{\omega^2}\frac{\omega}{c}\frac{\partial T_m}{\partial x}\left[1 + \left(1 - \frac{\varepsilon_s f_v}{(\sigma - 1) f_\kappa}\right)\frac{\tanh\left[(1 + i)a/\delta_\kappa\right]}{(1 + i)a/\delta_\kappa}\right] + (\gamma - 1)\frac{\tanh\left[(1 + i)a/\delta_\kappa\right]}{(1 + i)a/\delta_\kappa}\right\}. \quad (11)$$

Finally, referring to Appendix B, we can compute k and z according to

$$k^2 = \omega^2 C(\omega) \rho_c, \quad (12)$$

and

$$z = (k/\omega)/\Omega C(\omega). \quad (13)$$

Note that now $C(\omega)$, and therefore k, depends upon the direction of propagation and that where the $\pm$ appears, so does dT_m/dx. The term dT_m/dx is positive when the temperature increases in the direction of propagation.

The presence of a temperature gradient establishes a difference in propagation constants beyond a simple change in direction. In Region 3,

$$p_i^{(3)} = P_i^{(3)} e^{i(\omega t - k_3 x)} \quad (14)$$

In the direction of propagation of the incident wave, dT_m/dx is positive. The reflected wave is

$$p_r(3) = P_r(3)e^{i(\omega t - k'_3 x)}. \tag{15}$$

For $dT_m/dx = 0$, $k_3 = k'_3 = \omega/c - i\alpha$. In the presence of a temperature gradient, k_3 will have an increasing imaginary part while k'_3 will have an imaginary part that decreases to zero then becomes positive.

The only remaining task is to get an expression for P_{total}. If the impedance z is only associated with a boundary condition, then dT_m/dx should not enter the calculation of z, i.e., z is associated with a boundary, not with a wave. This means that at $x = l_3$, $z_3 = z'_3 = z$ calculated for that temperature. At $x = l_4$, $z_4 = z'_4 = z$ calculated at $T_m = T_{hot}$. To include this asymmetry, we must rewrite the boundary conditions at $x = l_3$ as

$$P_i^{(3)}e^{-ik_3 l_3} + P_r^{(3)}e^{ik'_3 l_3} = P_i^{(4)}e^{-ik_4 l_3} + P_r^{(4)}e^{ik_4 l_3} \tag{16}$$

and

$$\frac{1}{z_3}P_i^{(3)}e^{-ik_3 l_3} - \frac{1}{z_3}P_r^{(3)}e^{ik'_3 l_3} = \frac{1}{z_4}\left[P_i^{(4)}e^{-ik_4 l_3} - P_r^{(4)}e^{ik_4 l_3}\right], \tag{17}$$

or rewriting,

$$P_i^{(3)}\left[e^{-ik_3 l_3} - B\frac{z_4}{z_3}e^{-ik_3 l_3}\right] = -P_r^{(3)}\left[e^{ik'_3 l_3} + B\frac{z_4}{z_3}e^{ik'_3 l_3}\right] \tag{18}$$

and

$$P_r^{(3)} = \frac{e^{-ik_3 l_3}}{e^{ik'_3 l_3}}\frac{[B-1]}{[B+1]}, \tag{19}$$

where B is defined in Appendix A. Working toward the driving end, we must apply a similar treatment at $x = l_2$,

$$P_i^{(2)}e^{-ik_2 l_2} + P_r^{(2)}e^{ik_2 l_2} = P_i^{(3)}e^{-ik_3 l_2} + P_r^{(3)}e^{ik'_3 l_2} \tag{20}$$

and

$$\frac{1}{z_2}\left\{P_i^{(2)}e^{-ik_2 l_2} - P_r^{(2)}e^{ik_2 l_2}\right\} = \frac{1}{z_3}P_i^{(3)}e^{-ik_3 l_2} - \frac{1}{z_3}P_r^{(3)}e^{ik'_3 l_2} \tag{21}$$

or

$$P_i^{(2)}e^{-ik_2 l_2} - P_r^{(2)}e^{ik_2 l_2} = P_i^{(3)}\left\{e^{-ik_3 l_2} + e^{-ik_3 l_3 - ik'_3 l_3}\frac{[B-1]}{[B+1]}e^{ik'_3 l_2}\right\} \tag{22}$$

or

$$P_i^{(2)} e^{-ik_2l_2} - P_r^{(2)} e^{ik_2l_2} = P_i^{(3)} z_2 \left\{ \frac{1}{z_3} e^{-ik_3l_2} - \frac{1}{z_3} e^{-ik_3l_3 - ik_3'l_3} \frac{[B-1]}{[B+1]} e^{ik_3'l_2} \right\}. \qquad (23)$$

Dividing, and setting the ratio on the right hand side equal to C,

$$P_i^{(2)} e^{-ik_2l_2} + P_r^{(2)} e^{ik_2l_2} = CP_i^{(2)} e^{-ik_2l_2} - CP_r^{(2)} e^{ik_2l_2} \qquad (24)$$

or,

$$P_i^{(2)} e^{-ik_2l_2} [1-C] = -P_r^{(2)} e^{ik_2l_2} [1+C] \qquad (25)$$

or

$$P_r^{(2)} = \left[\frac{C-1}{C+1} \right] e^{-2ik_2l_2} P_i^{(2)}. \qquad (26)$$

The pattern for no temperature gradient derived in Appendix A is now reestablished and P_{total} has the same form as in Appendix A.

For the purpose of the calculations, the speed of sound, viscosity, etc. within the stack are computed at the average temperature of the stack. The results of the calculations are shown in Figs 4-8, along with the experimental data. These figures are graphs of 1/Q, which is proportional to the net attenuation in the resonator, versus temperature difference, ranging from zero to that required for onset of self oscillation. The figures correspond to mean gas pressures of 170, 238, 307, 376, and 500 kPa, respectively. The individual points represent the measurements and the lines show the results of the calculations. Although the agreement between the theory and experiment is generally pleasing, there are some noticeable differences. The theory over predicts the attenuation at low temperature differences, though this discrepancy diminishes with increasing mean pressure. Also, the predicted onset temperature difference increases with mean pressure, ranging from approximately 320 K at 170 kPa mean pressure to 460 K at 500 kPa. The measured onset temperature difference does not show such a regular pattern.

Measurements were also made for the second and third longitudinal modes of the resonator at
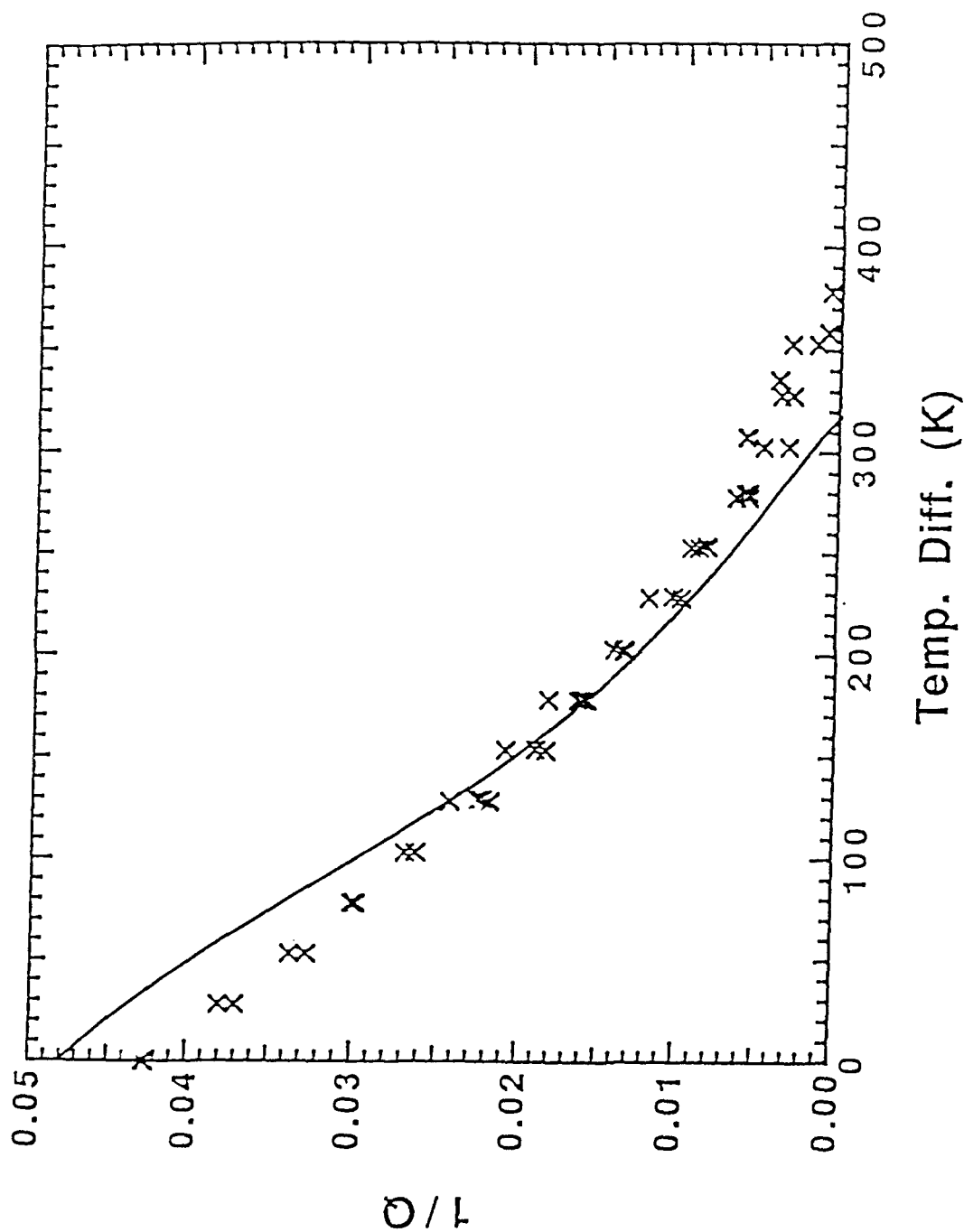
Figure 4: Graph of 1/Q vs the temperature difference across the prime mover stack. The symbols represent the data, while the line represents the results of the calculations. The prime mover is filled with helium at a mean pressure of 170 kPa.

Figure 5: Graph of 1/Q vs the temperature difference across the prime mover stack. The symbols represent the data, while the line represents the results of the calculations. The prime mover is filled with helium at a mean pressure of 238 kPa.

Figure 6: Graph of 1/Q vs the temperature difference across the prime mover stack. The symbols represent the data, while the line represents the results of the calculations. The prime mover is filled with helium at a mean pressure of 307 kPa.

Figure 7: Graph of 1/Q vs the temperature difference across the prime mover stack. The symbols represent the data, while the line represents the results of the calculations. The prime mover is filled with helium at a mean pressure of 376 kPa.
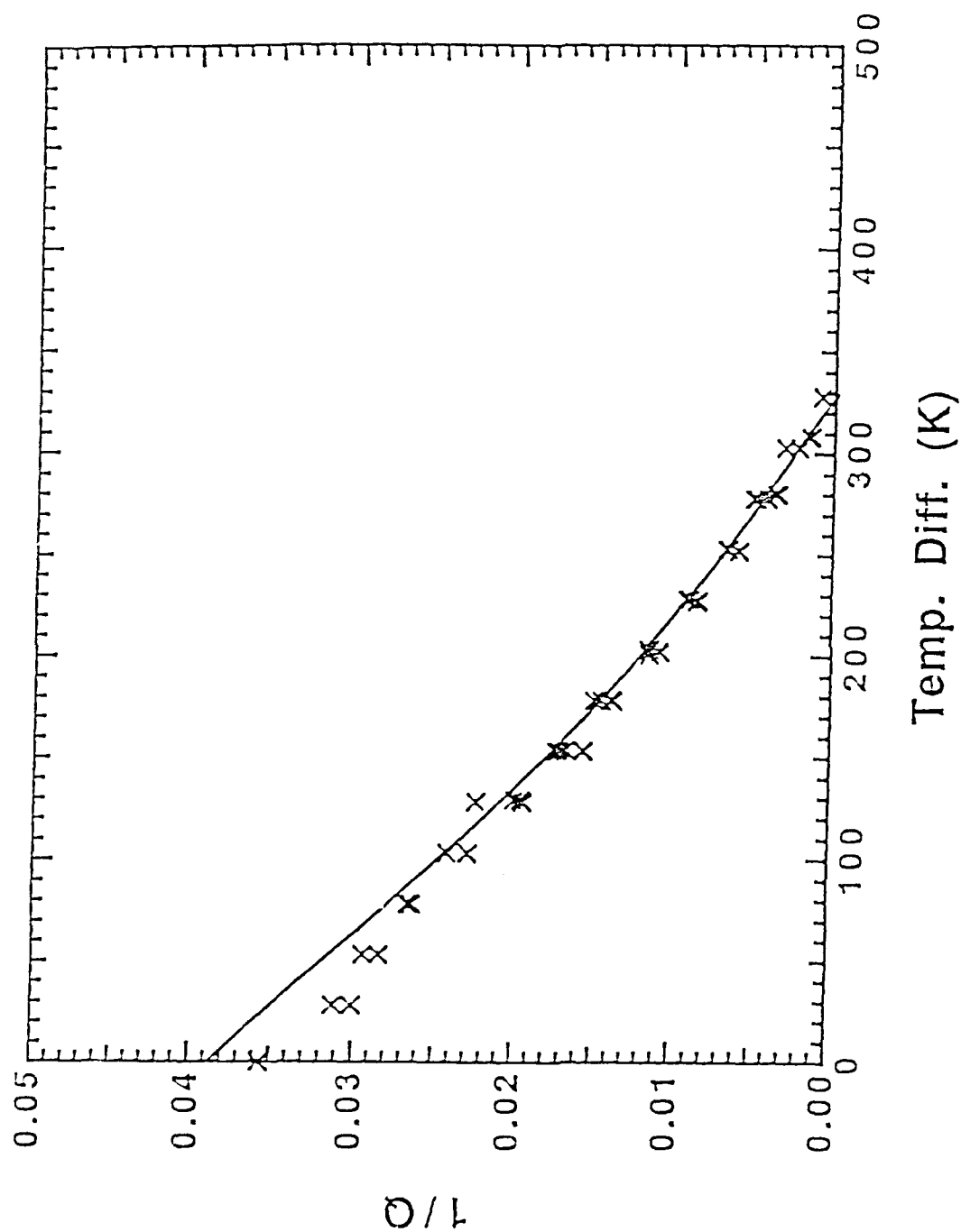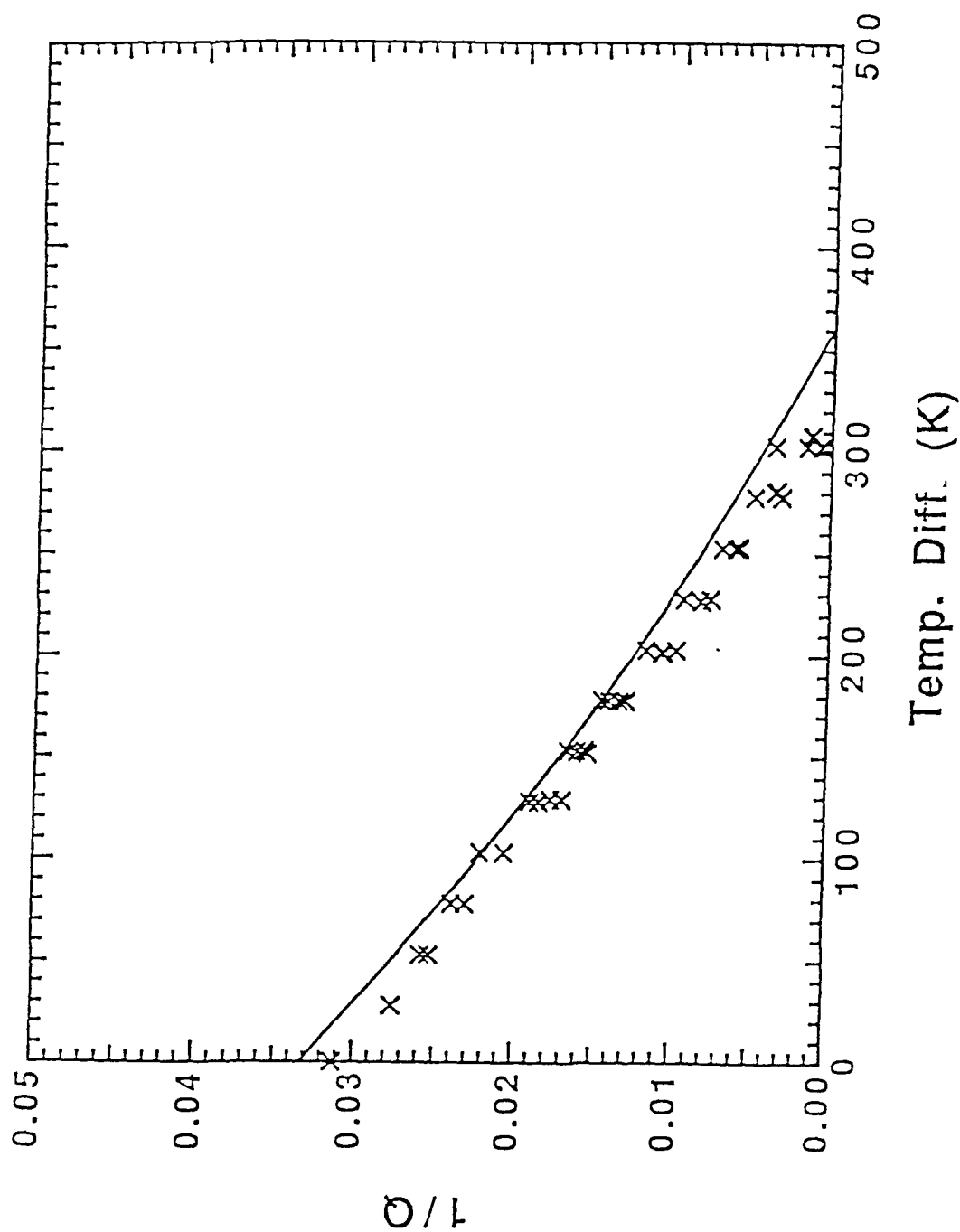
Figure 8: Graph of 1/Q vs the temperature difference across the prime mover stack. The symbols represent the data, while the line represents the results of the calculations. The prime mover is filled with helium at a mean pressure of 500 kPa.
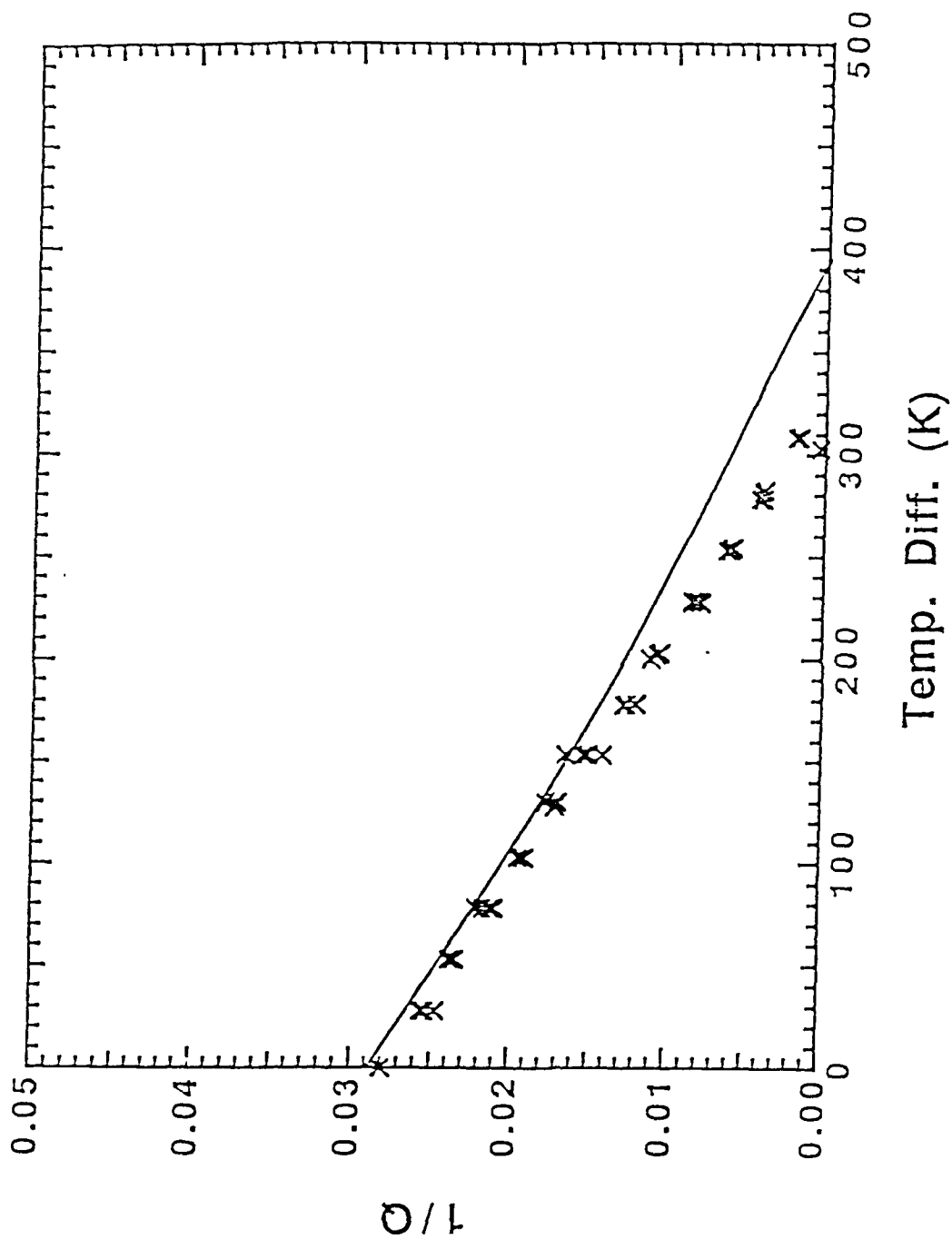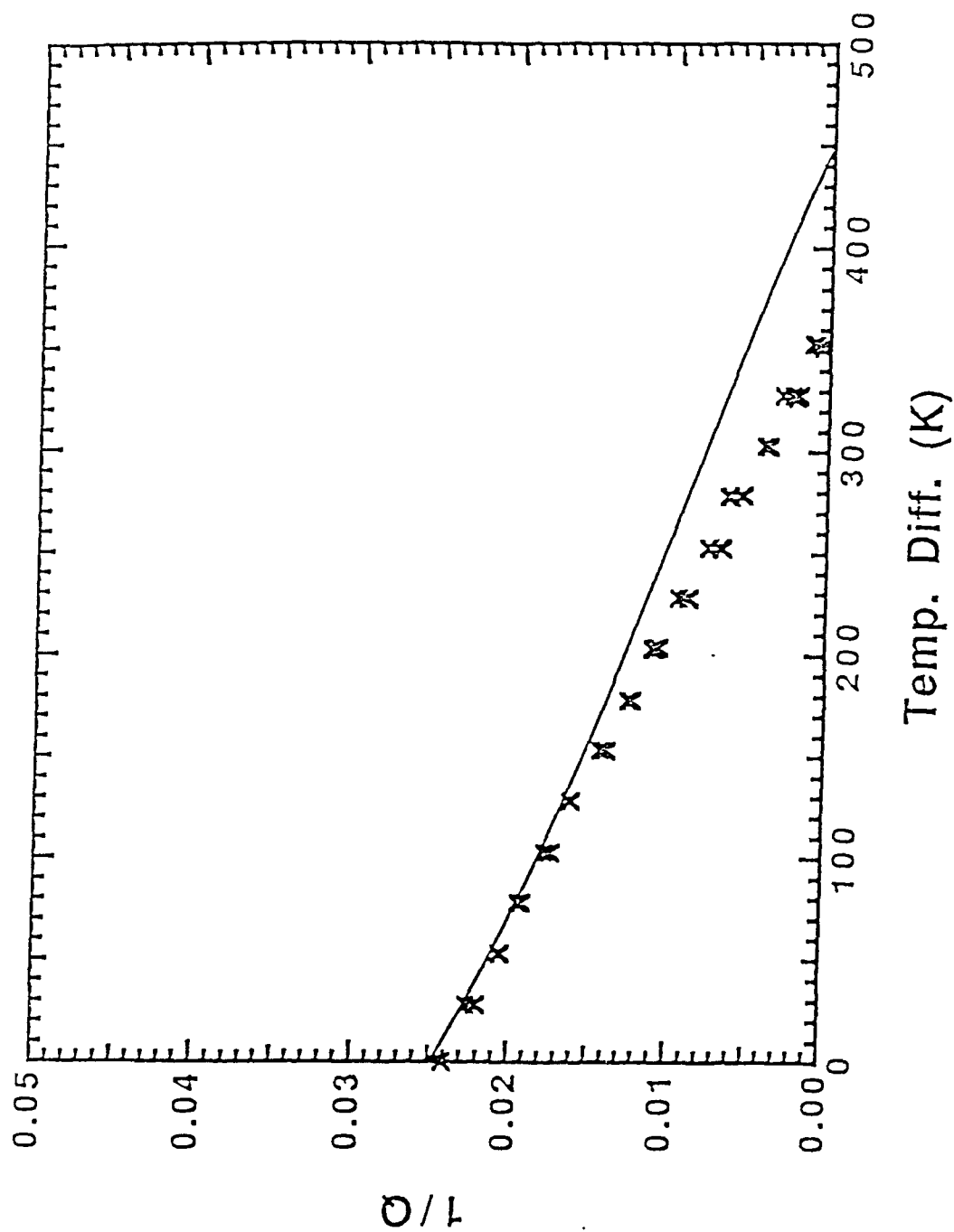
two mean gas pressures, 170 and 307 kPa. The data and calculations are shown in Figs. 9 and 10. The X's and solid lines correspond to the second mode, while the open squares and dashed lines correspond to the third. It was not possible to make measurements near onset for these modes, because the onset temperatures exceed that of the fundamental. The agreement is good. The tendency to over predict the attenuation at zero gradient decreases, especially for the third mode. No conclusions can be drawn concerning the ability to predict the onset temperature.

III. SUMMARY AND DISCUSSION

The frequency response of a thermoacoustic prime mover has been measured as a function of the mean gas pressure and temperature gradient across the prime mover stack. The frequency response of two simpler resonator configurations was also measured in the absence of an applied gradient. The quality factor Q and resonance frequency were determined from the response. Rather than using a standing wave analysis such as that given by Swift,[1] we have analyzed the results in terms of counterpropagating plane waves, an approach used in studies of the acoustic properties of porous materials. The motivation behind this analysis is to develop the ability to transfer extensive research of porous materials to performance predictions of thermoacoustic devices. This type of analysis will be especially useful when considering the use of alternative geometries in the prime mover stack.

In general, the predictions of the counterpropagating plane wave analysis are in good agreement with experiment. The predictions of Q and the change in resonance frequency with mean gas pressure are within approximately 5% and 0.4% of measured values for the no temperature gradient cases. In the cases where temperature gradients are present, the agreement is pleasing, but there are some noticeable discrepancies. Surprisingly, some of the worst agreement is for small temperature gradients. The reason for this discrepancy is unknown. However, the effect is less noticeable at higher mean gas pressures and frequencies. The analysis provides the

Figure 9: Graph of 1/Q vs the temperature difference across the prime mover stack for the second and third longitudinal modes. The X's and solid line correspond to the second mode, while the open squares and dashed line correspond to the third. The prime mover is filled with helium at a mean pressure of 170 kPa.
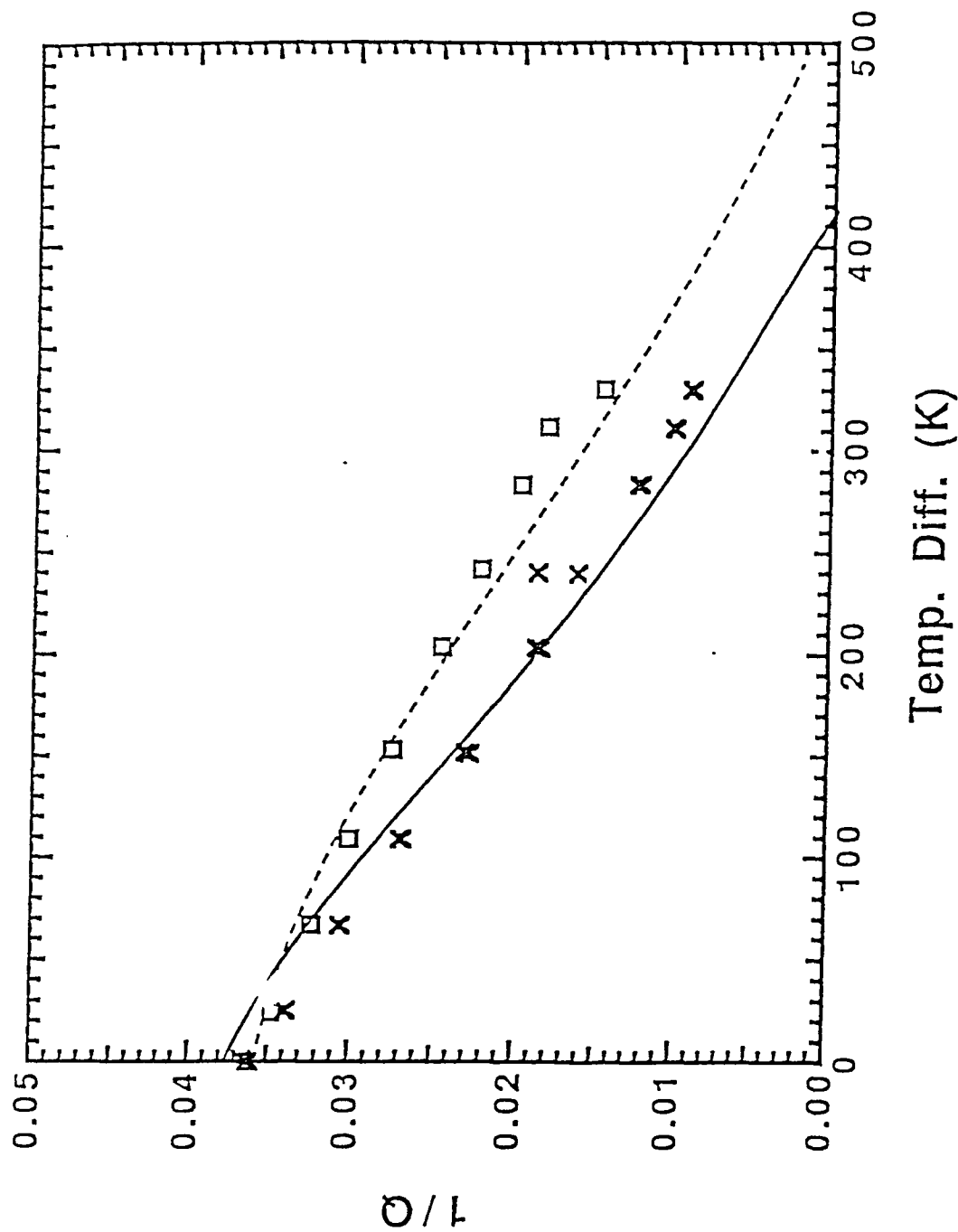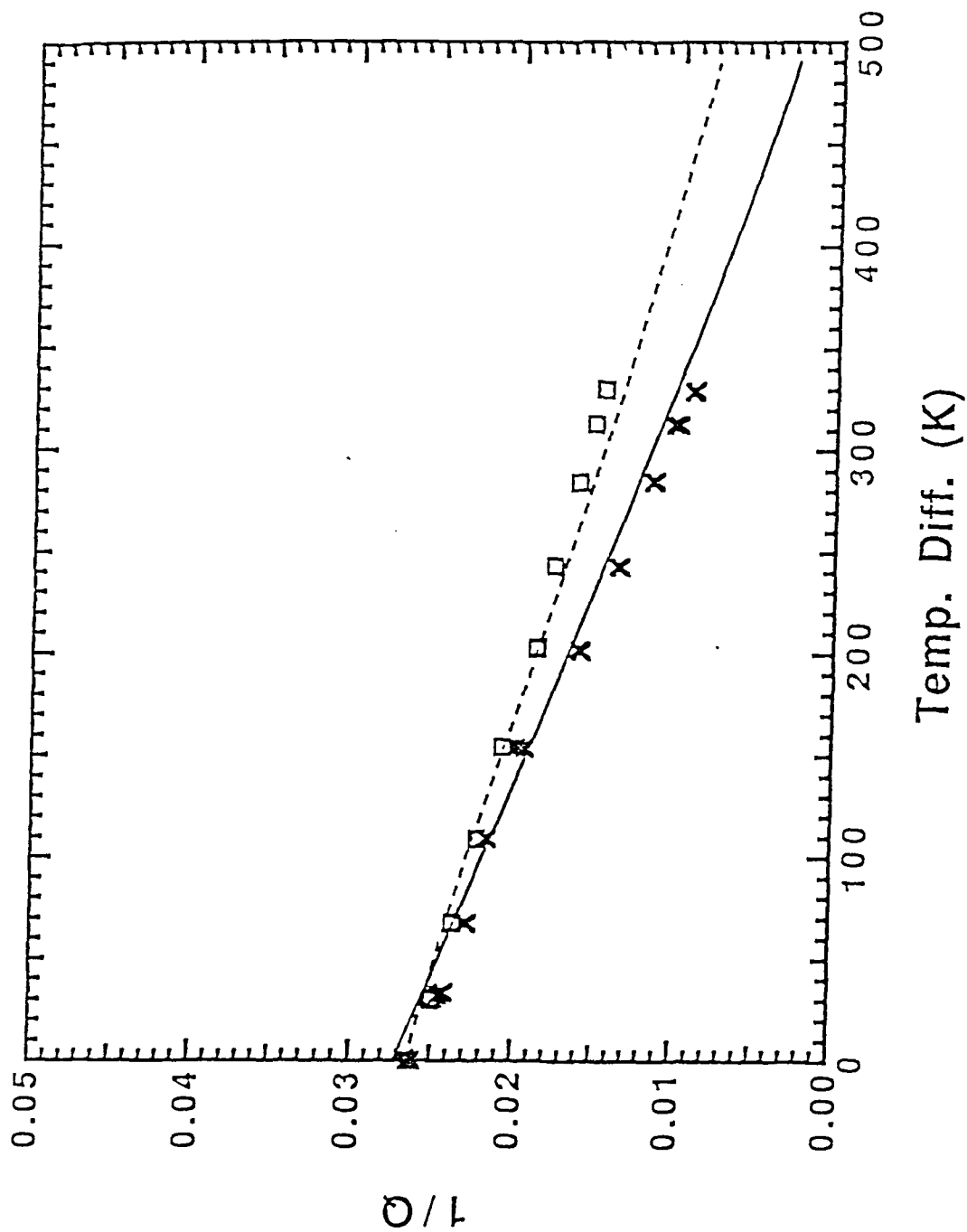
Figure 10: Graph of 1/Q vs the temperature difference across the prime mover stack for the second and third longitudinal modes. The X's and solid line correspond to the second mode, while the open squares and dashed line correspond to the third. The prime mover is filled with helium at a mean pressure of 307 kPa.

best overall agreement at intermediate gas pressures. There is a tendency to under predict the onset temperature at lower pressures and over predict it at higher pressures. We have not presented data or predictions for the resonance frequency as a function of temperature gradient. However, the predictions agree with measured values to within a few Hz, a discrepancy of approximately 1 %.

Even taking into consideration these discrepancies, our analysis provides a good overall prediction of the performance of the prime mover below onset. However, the true test is predicting the performance above onset. These are several significant differences between prime movers above and below onset. Most obvious is that the acoustic amplitudes above onset are quite large. Ratios of acoustic pressure amplitude to mean gas pressure of 1 - 10 % are common. Yet, our analysis is based on linear acoustics. Beyond the theoretical complications added by introducing nonlinear effects, there are a number of experimental complications. For instance, the acoustic displacement amplitudes approach the length of the heat exchangers. Also because of the large transport of heat, there is no assurance that the temperature distribution along the prime mover stack will be uniform.

The next logical step in this research is to investigate prime movers above onset, but still in the linear acoustics regime. This study requires the use of some type of known additional attenuation to limit the amplitudes. Also, the counterpropagating plane wave analysis should be compared to Swift's analysis.[1]

ACKNOWLEDGMENTS

APPENDIX A: Derivation of P_{total}

The derivation of P_{total} in the absence of a temeprature gradient is presented in this appendix. The combination of elements in the thermoacoustic prime mover creates a series of boundaries, each with a characteristic impedance. The total acoustic field inside the resonant tube will be evaluated by considering the field as a superposition of traveling waves moving in each direction through this series of boundaries and porous elements.

The incident and reflected waves in the five regions can be expressed as

$$p_i^{(1)} = p_i^{(1)} e^{i(\omega t - k_1 x)} \qquad\qquad p_r^{(1)} = p_r^{(1)} e^{i(\omega t + k_1 x)}$$

$$\bullet \qquad\qquad\qquad\qquad \bullet$$

$$\bullet \qquad\qquad\qquad\qquad \bullet$$

$$\bullet \qquad\qquad\qquad\qquad \bullet$$

$$p_i^{(5)} = p_i^{(5)} e^{i(\omega t - k_5 x)} \qquad\qquad p_r^{(5)} = p_r^{(5)} e^{i(\omega t + k_5 x)}$$

First consider the rigid end at $x = l_5$. For a rigid boundary, $u=0$. Newton's law gives $\rho_0\, \partial u/\partial t = -\nabla p$. Assuming time harmonic plane waves, $\partial u/\partial t = j\omega u$ so $j\omega\rho_0 u = -\nabla p$. Hence, the boundary condition $u = 0$ requires that $\nabla p = 0$ at $x = l_5$ or

$$[\nabla (P_i^{(5)} e^{i(\omega t - k_5 x)} + P_r^{(5)} e^{i(\omega t + k_5 x)})]_{x=l_s} = 0 , \qquad (A1)$$

or

$$P_r^{(5)} = e^{-2ik_5 l_s}\, P_i^{(5)}. \qquad (A2)$$

Next consider the boundary at $x = l_4$. Continuity of pressure gives

$$P_i^{(4)} e^{i(\omega t - k_4 l_4)} + P_r^{(4)} e^{i(\omega t + k_4 l_4)} = P_i^{(5)} e^{i(\omega t - k_5 l_4)} + P_r^{(5)} e^{i(\omega t + k_5 l_4)}, \qquad (A3)$$

or using Eq. (A2)

73

$$P_i^{(4)} e^{-ik_4 l_4} + P_r^{(4)} e^{ik_4 l_4} = P_i^{(5)} \left[e^{-ik_5 l_4} + e^{-2ik_5 l_5} + e^{ik_5 l_4} \right]. \tag{A4}$$

Continuity of volume velocity needs to take into account changes in porosity and can be written as

$$\left[U_i^{(4)} + U_r^{(4)} = U_i^{(5)} + U_r^{(5)} \right]_{x = l_4}. \tag{A5}$$

But, $U = Su = Sp/z_{sa}$, where S is the cross sectional area of the fluid and z_{sa} is the specific acoustic impedance of the region. Hence, continuity of volume velocity can be written as

$$\frac{S^{(4)}}{z_{sa}^{(4)}} \left(P_i^{(4)} e^{-ik_4 l_4} - P_r^{(4)} e^{+ik_4 l_4} \right) = \frac{S^{(5)}}{z_{sa}^{(5)}} \left(P_r^{(5)} e^{-ik_5 l_4} - P_r^{(5)} e^{+ik_5 l_4} \right). \tag{A6}$$

Dividing by the cross sectional area of the empty tube S, defining the porosity $\Omega^{(n)} = S^{(n)}/S$, and further defining the impedance $z_n = z_{sa}^{(n)}/\Omega^{(n)}$ yields

$$\frac{1}{z_4} \left[P_i^{(4)} e^{-ik_4 l_4} - P_r^{(4)} e^{ik_4 l_4} \right] = \frac{P_i^{(5)}}{z_5} \left[e^{-ik_5 l_4} - e^{-2ik_5 l_5} e^{ik_5 l_4} \right]. \tag{A7}$$

Dividing Eq. (A4) by Eq. (A7) and solving for $P_r^{(4)}$ gives

$$P_r^{(4)} = e^{-2ik_4 l_4} \left[\frac{A-1}{A+1} \right] P_i^{(4)}, \tag{A8}$$

where

$$A = \frac{z_5}{z_4} \frac{e^{-ik_5 l_4} + e^{-2ik_5 l_5} e^{ik_5 l_4}}{e^{-ik_5 l_4} - e^{-2ik_5 l_5} e^{ik_5 l_4}}. \tag{A9}$$

Now to the boundary at $x = l_3$;

$$P_i^{(3)} e^{-ik_3 l_3} + P_r^{(3)} e^{ik_3 l_3} = P_i^{(4)} e^{-ik_4 l_3} + P_r^{(4)} e^{ik_4 l_3}, \tag{A10}$$

and

$$\frac{1}{z_3} \left[P_i^{(3)} e^{-ik_3 l_3} - P_r^{(3)} e^{ik_3 l_3} \right] = \frac{1}{z_4} \left[P_i^{(4)} e^{-ik_4 l_3} - P_r^{(4)} e^{ik_4 l_3} \right], \tag{A11}$$

so

$$\frac{P_i^{(3)} e^{-ik_3 l_3} + P_r^{(3)} e^{ik_3 l_3}}{P_i^{(3)} e^{-ik_3 l_3} - P_r^{(3)} e^{ik_3 l_3}} = \frac{z_4}{z_3} \left\{ \frac{e^{-ik_4 l_3} + e^{-2ik_4 l_4} \left[\frac{A-1}{A+1}\right] e^{ik_4 l_3}}{e^{-ik_4 l_3} - e^{-2ik_4 l_4} \left[\frac{A-1}{A+1}\right] e^{ik_4 l_3}} \right\} = B \tag{A12}$$

and

$$P_r^{(3)} = e^{-2ik_3 l_3} \left[\frac{B-1}{B+1}\right] P_i^{(3)}. \tag{A13}$$

We can now identify a pattern and write

$$P_r^{(2)} = e^{-2ik_2 l_2} \left[\frac{C-1}{C+1}\right] P_i^{(2)}, \tag{A14}$$

where

$$C = \frac{z_3}{z_2} \left\{ \frac{e^{-ik_3 l_2} + e^{-2ik_3 l_3} \left[\frac{B-1}{B+1}\right] e^{ik_3 l_2}}{e^{-ik_3 l_2} - e^{-2ik_3 l_3} \left[\frac{B-1}{B+1}\right] e^{ik_3 l_2}} \right\}, \tag{A15}$$

and

$$P_r^{(1)} = e^{-2ik_1 l_1} \left[\frac{D-1}{D+1}\right] P_i^{(1)}, \tag{A16}$$

where

$$D = \frac{z_2}{z_1} \left\{ \frac{e^{-ik_2 l_1} + e^{-2ik_2 l_2} \left[\frac{C-1}{C+1}\right] e^{ik_2 l_1}}{e^{-ik_2 l_1} - e^{-2ik_2 l_2} \left[\frac{C-1}{C+1}\right] e^{ik_2 l_1}} \right\}. \tag{A17}$$

Now we must consider the driver. We will assume that the driver delivers a constant displacement l independent of load, $x = l\, e^{i\omega t}$. In this case, the velocity (provided l is small) is $u_0(0,t) = i\omega l\, e^{i\omega t}$. Applying continuity of volume velocity (with the definition of z_n) at $x=0$,

$$i\omega l\, e^{i\omega t} = \frac{1}{z_1} (P_i^{(1)} - P_r^{(1)})\, e^{i\omega t} = \frac{1}{z_1} P_i^{(1)} \left(1 - e^{-2ik_1 l_1} \left[\frac{D-1}{D+1}\right]\right) e^{i\omega t}, \tag{A18}$$

so

$$P_i^{(1)} = \frac{i\omega l / z_1}{\left(1 - e^{-2ik_1 l_1} \left[\frac{D-1}{D+1}\right]\right)}, \tag{A19}$$

and

$$P_{total} = P_i^{(1)} + P_r^{(1)} = i\omega l / z_1 \frac{1 + e^{-2ik_1 l_1} \left[\frac{D-1}{D+1}\right]}{1 - e^{-2ik_1 l_1} \left[\frac{D-1}{D+1}\right]}. \tag{A20}$$

75

APPENDIX B: Parallel Slits Without a Temperature Gradient

Using fundamental concepts from inviscid acoustics, it is easy to show that the propagation constant and specific acoustic impedance can be expressed as

$$k^2 = \omega^2 \, C \, \rho_f, \tag{B1}$$

and

$$z_{sa} = (k/\omega)/C. \tag{B2}$$

In these equations ω is the angular frequency, ρ_f the mean fluid density and C the compressibility of the medium. One way of defining the compressibility is through the equation of state $p = s/C$, p is the acoustic pressure and s the condensation. These results must, of course, be modified when considering propagation through porous media to take into acoustic the complications introduced by viscosity and thermal conductivity. The approach commonly taken in porous media analysis is to incorporate the added complexity into the definitions of new parameters, such as the complex density and compressibility, leaving the forms of Eqs. (B1) and (B2) unchanged. This analysis is outlined in this Appendix. The reader is directed to *Refs. 7, 9 and 10 for a more complete analysis.*

The average acoustic velocity in the slit formed between two stationary parallel plates separated by 2a is[10]

$$\bar{u}_1 = \frac{-1}{i\omega\rho_f}\frac{\partial p}{\partial x}\left(1 - \frac{\tanh\left[(1+i)a/\delta_v\right]}{(1+i)a/\delta_v}\right), \tag{B3}$$

where where $\delta_v = (2v/\omega)^{1/2}$, and v is the kinematic viscosity. We define the complex density ρ_c in terms of the pressure gradient and the slit-averaged acoustic velocity such that

$$\frac{-\partial p}{\partial x} = \rho_c\left(\frac{\partial \bar{u}_1}{\partial t}\right). \tag{B4}$$

To be consistent we should use the slit-averaged pressure gradient in Eq. (B4). However, we have assumed the pressure to dependent only on x, so this distinction need not be made. Solving Eq. (B3) for $-(\partial p/\partial x)$ and comparing the result to Eq. (B4) gives

$$\rho_c = \rho_f\left(1 - \frac{\tanh\left[(1 + i)a/\delta_v\right]}{(1 + i)a/\delta_v}\right)^{-1}.$$ (B5)

The temperature equation is

$$i\omega\rho_f c_p\theta + i\omega p = \lambda_h \frac{\partial^2\theta}{\partial y^2},$$ (B6)

where λ_h is the coefficient of thermal conduction, θ the difference between slit wall and fluid temperatures, and c_p the specific heat of the fluid. y is measured perpendicular to the slit wall. Applying the boundary condition that $\theta = 0$ at $y = \pm a$ yields the solution

$$\theta = p/\rho_f c_p\left(1 - \frac{\cosh\left[(1 + i)y/\delta_\kappa\right]}{\cosh\left[(1 + i)a/\delta_\kappa\right]}\right).$$ (B7)

A differential form of the ideal gas equation of state is $d\rho/\rho_f = dp/p_m - dT/T_m$. Substituting acoustic quantities for differentials and identifying the condensation as ρ/ρ_f, we have

$$s = p/p_m - \theta/T_m.$$ (B8)

Substituting Eq. (B7) into Eq. (B8), and noting that $p_m/\rho_f c_p T_m = (\gamma - 1)/\gamma$ for an ideal gas, gives

$$s = \frac{p}{\gamma p_m}\left(1 + (\gamma - 1)\frac{\cosh\left[(1 + i)y/\delta_\kappa\right]}{\cosh\left[(1 + i)a/\delta_\kappa\right]}\right).$$ (B9)

Averaging the condensation across the slit gives,

$$\bar{s} = \frac{p}{\gamma p_m}\left(1 + (\gamma - 1)\frac{\tanh\left[(1 + i)a/\delta_\kappa\right]}{\left[(1 + i)a/\delta_\kappa\right]}\right).$$ (B10)

Zwikker and Kosten[9] define the complex compressibility of the gas in the slit through the silt-averaged equation of state

$$\bar{p} = \bar{s}/C(\omega) \tag{B11}$$

Substituting Eq. (B10) into Eq. (B11) and keeping in mind that the pressure is assumed constant across the slit, we arrive at the following expression for the complex compressibility

$$C(\omega) = \frac{1}{\gamma P_m}\left(1 + (\gamma - 1)\,\frac{\tanh\left[(1 + i)a/\delta_\kappa\right]}{\left[(1 + i)a/\delta_\kappa\right]}\right).\tag{B12}$$

Now that we have the (slit-averaged) complex density and compressibility, we can immediately write down the slit-averaged expressions for the propagation constant and impedance. From Eq. (B1),

$$k^2 = \omega^2\, C(\omega)\, \rho_c\,.\tag{B13}$$

From Eq. (B2) and the relation $z = z_{sa}/\Omega$ (see Appendix A)

$$z = (k/\omega)/\Omega C(\omega).\tag{B14}$$

To find common ground with those readers familiar with Swift's work, especially Ref. 1, our Eqs. (B3), (B6), and (B7) are identical to (from Ref. 1) the slit averaged Eq. (A4), and Eqs. (A9) and (A10) in the absence of a temperature gradient, respectively.

REFERENCES

1. G.W. Swift, "Thermoacoustic Engines," J. Acoust. Soc. Am. 84, 1145-1180 (1988).

2. J.C. Wheatley and A. Cox, "Natural Engines," Phys. Today 38, 50 (1085).

3. N. Rott, "Thermoacoustics," Adv. Appl. Mech. 20, 135 (1980).

4. See, for example, Samuel Temkin, "Elements of Acoustics," Chapter 3 (John Wiley and Sons, Inc., New York, 1981).

5. J.W.S. Rayleigh, "The Theory of Sound," Chapters XI and XII (1896, Reprinted 1945 by Dover Publications, Inc., Toronto).

6. F.D. Shields, "Numerical solution for sound velocity and absorption in cylindrical tubes," J. Acoust. Soc. Am. 37, 724-729 (1965).

7. Keith Attenborough, "Acoustical characteristics of porous materials," Physics Reports 82, 179-227 (1982).

8. Keith Attenborough, private communication.

9. C. Zwikker and C. W. Kosten, Sound absorbing materials (Elsevier Publishing Co., Inc., New York, 1949).

10. M.A. Biot, "Theory of propagation of elastic waves in a fluid-saturated porous solid. II. Higher frequency range," J. Acoust. Soc. Am. 28, 179-192 (1956).

	Argon					
Pressure (kPa)	f_o(measured)	f_o(predicted)	% error	Q(measured)	Q(predicted)	% error
170	155.6	156.	+0.3	79	81	+2.5
238	155.8	156.5	+0.4	91	95	+4.4
307	156	156.5	+0.3	102	110	+7.8
376	156.1	156.5	+0.3	116	123	+6.0
	$\Delta f = 0.5$	$\Delta f = 0.5$	avg = +0.3			avg = +5.1

	Helium					
Pressure (kPa)	f_o(measured)	f_o(predicted)	% error	Q(measured)	Q(predicted)	% error
170	489	487.5	+0.3	48	50	+4.2
238	490.2	488	+0.4	57	59	+3.5
307	490.6	488.5	+0.4	64	67	+4.7
376	490.5	489	+0.3	70	74	+5.7
	$\Delta f = 1.6$	$\Delta f = 1.5$	avg = +0.35			avg = +4.5

Table I. Measured and predicted values of the resonance frequency and Q of the empty resonator for helium and argon gas at various pressures. Δf is the total change in resonance frequency with pressure.

Argon

Pressure (kPa)	f_o(measured)	f_o(predicted)	% error	Q(measured)	Q(predicted)	% error
170	156.4	156.5	+0.1	60	59	-1.7
238	156.5	157	+0.3	72	71	-1.4
307	156.4	157	+0.4	81	82	+1.2
376	156.7	157	+0.2	89	91	+2.2
500	157.1	157	-0.1	102	103	+1.0
	$\Delta f = 0.7$	$\Delta f = 0.5$	avg = +0.2			avg = +0.3

Helium

Pressure (kPa)	f_o(measured)	f_o(predicted)	% error	Q(measured)	Q(predicted)	% error
170	490.3	488.5	-0.4	36	35	-2.8
238	491.4	489.5	-0.4	43	42	-2.3
307	492.0	490	-0.4	49	49	0
376	493.1	490.5	-0.5	55	54	-1.8
	$\Delta f = 2.8$	$\Delta f = 2.0$	avg = -0.4			avg = -1.7

Table II. Measured and predicted values of the resonance frequency and Q of the resonator with the ambient heat exchanger for helium and argon gas at various pressures. Δf is the total change in resonance frequency with pressure.

Argon

Pressure (kPa)	f_0(measured)	f_0(predicted)	% error	Q(measured)	Q(predicted)	% error
170	161.6	162.0	+0.2	40	38	-5
238	161.8	162.0	+0.1	47	47	0
307	162.1	162.0	+0.0	54	53	-2
376	162.1	162.5	+0.2	58	59	+2
500	162.3	162.5	+0.1	68	70	+3
	$\Delta f = 0.7$	$\Delta f = 0.5$	avg = +0.15			avg = +2

Helium

Pressure (kPa)	f_0(measured)	f_0(predicted)	% error	Q(measured)	Q(predicted)	% error
170	505.2	504.5	-0.1	23	20	-13
238	507.2	505.5	-0.3	28	26	-7
307	508.5	506	-0.5	32	30	-6
376	509.4	507	-0.5	36	34	-6
500	510.5	507.5	-0.6	42	40	-5
	$\Delta f = 5.3$	$\Delta f = 3.0$	avg = -0.4			avg = -7

Table III. Measured and predicted values of the resonance frequency and Q of the prime mover with no temperature gradient for helium and argon gas at various pressures. Δf is the total change in resonance frequency with pressure.

$$f_v = \frac{\tanh\left[(1+i)\, a/\delta_v\right]}{(1+i)\, a/\delta_v} \qquad\qquad f_k = \frac{\tanh\left[(1+i)\, a/\delta_k\right]}{(1+i)\, a/\delta_k}$$

$$\varepsilon_s = \sqrt{\frac{\lambda_h \rho_f c_p}{\lambda_s \rho_s c_s} \frac{\tanh\left[(1+i)a/\delta_k\right]}{\tanh\left[(1+i)a/\delta_s\right]}}$$

$$\delta_v = \sqrt{2v/\omega} \qquad\qquad\qquad \delta_k = \sqrt{2\kappa_f/\omega}$$

$$\delta_s = \sqrt{2\kappa_s/\omega} \qquad\qquad\qquad \kappa_s = \lambda_s/\rho_s c_s$$

$$\kappa_f = \lambda_h/\rho_f c_p \qquad\qquad \lambda_h = \text{thermal conductivity of the fluid}$$

λ_s = solid thermal conductivity $\qquad\qquad$ ρ_s = solid density

c_s = solid specific heat/unit mass $\qquad\qquad$ b = half width of solid

----

Table IV. Symbols used in Eq. (6).

Appendix D:

Measurement and Calculation of Acoustic Propagation Constants in Arrays of Small
Air-Filled Rectangular Tubes

Measurement and calculation of acoustic propagation constants in arrays of small air-filled rectangular tubes

Heui-Seol Roh, W. Patrick Arnott, and James M. Sabatier

National Center for Physical Acoustics, University of Mississippi, University, Mississippi 38677

Richard Raspet

Department of Physics and Astronomy, University of Mississippi, University, Mississippi 38677

ABSTRACT

An experimental and theoretical investigation of sound propagation in a porous sample composed of capillary tubes with rectangular cross sections is described in this paper. An experimental technique valid for low flow resistivity and high porosity porous samples was developed to measure the attenuation and phase velocity in the porous material. This technique uses transmission of a short pulse in a large tube through the porous sample and subsequent frequency domain analysis in the range 200 to 1300 Hz. Good agreement was obtained if an anomalous tortuosity factor of 1.1 is used in the theory. A scaling factor for relating cylindrical and square tube capillary theories, known as the dynamic shape factor, was investigated. Propagation constants computed from use

of a near unity dynamic shape factor in the cylindrical pore theory agree favorably with calculations based on the square pore theory for the frequencies and pore radii used in the experiment.

(PACS #'s: 43.28.Fp, 43.20.Bi, 43.20.Mv, 43.85.Dj)

INTRODUCTION

The interaction of sound with porous media has many practical applications and has a long history. Porous media are ideal sound absorbers for use in architectural acoustics and anechoic chambers. The porous nature of the Earth's surface and ocean bottoms can greatly influence the propagation of sound in the air and oceans. An example of the diverse uses of sound propagation in porous media comes from our laboratory where we recently used measurements and theory for sound propagation in the porous ground to determine physical parameters which are related to the agricultural suitability of the soils investigated.[1]

Several models[2-5] for porous media are based on the adaptation of the solution for sound propagation in cylindrical capillary tubes to pores of irregular geometries. The basic fluid field equations used in these models are a simplified version of the linearized Navier-Stokes equations[3] for a fluid. The approximation employed in this calculation is that the transverse fluid velocities are much smaller than the longitudinal fluid velocity. Zwikker and Kosten[5] were first to obtain the solution based on the simplified version of the fluid model equations and showed that these solutions agreed with Kirchoff's exact solution[4] in the limit of high and low frequencies. Tijdeman[6] investigated the range of validity of the Zwikker and Kosten solution in comparison to the more rigorous Kirchoff solution and determined that the condition for the approximation to hold was the condition on velocities listed above. He refers to the Zwikker and Kosten theory as the "low reduced frequency approximation".

We have developed a porous media model for rectangular cross section capillary tubes. The rectangular pore calculation is based on the low reduced frequency approximation. Specifically, the model allows one to compute propagation constants and characteristic impedances for porous media consisting of rectangular pores. The effects of a slight capillary tube curvature or tortuosity are accounted for in this model. For the single pore, a series solution is used for the particle velocity, pressure, density, and temperature. The extension of the single pore theory to bulk media consisting of an array of pores is developed using standard techniques.[2,5] This is discussed in Sec. I. The single pore solution for rectangular pores has been developed independently by Stinson.[7]

The rectangular pore model is compared to attenuation and phase velocity measurements. The ceramic porous samples used in the experiment consisted of nominally straight capillary tubes having square cross sections. These low flow resistivity, high porosity samples may be useful for low frequency sound absorption. A more thorough description of the po₁ous samples and experimental technique is given in Sec. II. Comparison of theory and experiment is discussed in Sec. III.

A general theory for arbitrary pore shape[8] was developed by introducing a scale factor known as the dynamic shape factor to scale between different pore geometries. The limiting cases for this scaling factor are circular pores and parallel slits. The limiting cases of rectangular pores are square pores and parallel slits, which give rectangular pore theory a wide range of applicability. The dynamic shape factor for square pores is frequency dependent just as it is for parallel slits.[8] A discussion of the dynamic shape factor for square pores is given in Sec. IV.

I. PROPAGATION IN RECTANGULAR PORE MEDIA

Sound propagation in a single rectangular capillary tube is developed first. The acoustic field in the pore is specified to first order in the acoustic variables. Boundary

conditions at the pore wall are that the walls are rigid and thus the total particle velocity is taken as zero. Due to the high heat capacity and thermal conductivity of the pore wall, the temperature of the fluid in the pore at the boundary is taken to be the same as the pore wall. We do not assume any internal mean flow.[9] The single pore theory is then used to develop the theory for a porous material consisting of an array of rectangular capillary tubes possibly having a slight longitudinal curvature or tortuosity.

A. Acoustical disturbances in a single rectangular capillary tube.

The coordinate system shown in Fig. 1 has the z axis parallel to the tube axis. The transverse dimension is spanned by an x–y coordinate system with origin at the lower left corner of the rectangle. First order acoustic variables are the real parts of:

$$p(z,t) = p_0 + p_1(z) \exp(-i\omega t), \tag{1}$$

$$\vec{v}(x,y,z,t) = [v_x(x,y,z), v_y(x,y,z), v_z(x,y,z)] \exp(-i\omega t) \tag{2}$$

$$T(x,y,z,t) = T_0 + T_1(x,y,z) \exp(-i\omega t), \tag{3}$$

and

$$\rho(x,y,z,t) = \rho_0 + \rho_1(x,y,z) \exp(-i\omega t). \tag{4}$$

Subscript 0 refers to ambient values. Subscript 1 implies first order and in Eq. (2) the x,y, and z components of particle velocity are v_x, v_y, and v_z, respectively. Equations (1), (3), and (4) are the acoustic pressure, temperature, and density. Acoustical disturbances within the pore are taken to satisfy the following relations:

$$-i\omega\rho_0 v_z(x,y,z) = -\frac{dp_1(z)}{dz} + \eta\left(\frac{\partial}{\partial x^2} + \frac{\partial}{\partial y^2}\right)v_z(x,y,z), \qquad (5)$$

$$-i\omega\rho_1(x,y,z) + \rho_0\left(\frac{\partial v_x(x,y,z)}{\partial x} + \frac{\partial v_y(x,y,z)}{\partial y} + \frac{\partial v_z(x,y,z)}{\partial z}\right) = 0 \qquad (6)$$

$$\rho_1(x,y,z) = -\rho_0\beta T_1(x,y,z) + \frac{\gamma}{c^2}p_1(z), \qquad (7)$$

and

$$-i\omega\rho_0 c_p T_1(x,y,z) = -i\omega\beta T_0 p_1(z) + \kappa\left(\frac{\partial}{\partial x^2} + \frac{\partial}{\partial y^2}\right)T_1(x,y,z). \qquad (8)$$

These relations are given in the frequency domain where $\partial/\partial t$ is replaced by $-i\omega$ where t is time and ω is radian frequency. Response functions and transport coefficients are c_p, the constant pressure heat capacity per unit mass; γ, the ratio of specific heats; c, the adiabatic sound speed; $\beta = -(\partial\rho/\partial T)_p/\rho_0$, the thermal expansion coefficient; η, the viscosity; and κ, the thermal conductivity. In order, these equations express the z component of the equation of motion, continuity or mass conservation, equation of state for density, and heat transfer. Equations (5) through (8) are the same set of equations used by Zwikker and Kosten.[5] In using these approximate equations the assumption is that the transverse velocity components v_x and v_y are much less than the longitudinal velocity v_z. Further discussions of these approximations can be found in Appendix B of Ref. 6 and Appendix A of Ref. 10.

The following notation will be used to facilitate comparison with Attenborough's results.[2,8] A dimensionless "shear-wave number" which is proportional to the ratio of the pore radius and the viscous boundary layer thickness is $\lambda = R(\rho_0\omega/\eta)^{1/2}$. Here R is a characteristic transverse dimension of the pore. For definiteness we take R to be twice the

transverse pore area divided by the transverse pore perimeter. Thus, R is the tube radius for a cylindrical pore and is the semi-width for a square pore. "Wide tubes" with the same R are acoustically equivalent, i.e. they have the same propagation constants.[3] A dimensionless number proportional to the ratio of the pore radius to the thermal boundary layer thickness is $\lambda_T = R(\rho_0 \omega c_p / \kappa)^{1/2}$ or $\lambda_T = \lambda N_{pr}^{1/2}$ where $N_{pr} = \eta c_p / \kappa$ is the Prandtl number.

To make rapid progress, denote the z-component of particle velocity, v_z, by

$$v_z(x,y,z) = \frac{F(x,y;\lambda)}{i\omega\rho_0} \frac{dp_1(z)}{dz} .$$

(9)

Similarly, denote by

$$T_1(x,y,z) = \frac{\gamma - 1}{c^2 \rho_0 \beta} p_1(z) F(x,y;\lambda_T)$$

(10)

the acoustic pore temperature. The thermodynamic relation $T_0 \beta^2 / c_p = (\gamma - 1)/c^2$ can be used in Eq. (8) for T_1. Particle velocity and temperature $^\Gamma$ (5) and (8) reduce to the simple forms

$$F(x,y;\lambda) + \frac{R^2}{i\lambda^2} \left(\frac{\partial}{\partial x^2} + \frac{\partial}{\partial y^2} \right) F(x,y;\lambda) = 1 ,$$

(11)

and

$$F(x,y;\lambda_T) + \frac{R^2}{i\lambda_T^2} \left(\frac{\partial}{\partial x^2} + \frac{\partial}{\partial y^2} \right) F(x,y;\lambda_T) = 1 ,$$

(12)

respectively, subject to the boundary condition F = 0 at the pore boundary. The solution for F(x,y;λ) for rectangular pore boundaries is[11]

$$F(x,y;\lambda) = \frac{16}{\pi^2} \sum_{m,n\,odd} \frac{\sin(m\pi x/2a)\,\sin(n\pi y/2b)}{mnY_{m,n}(\lambda)} \tag{13}$$

where

$$Y_{m,n}(\lambda) = 1 + (i\pi^2/\lambda^2)\,\frac{b^2m^2 + a^2n^2}{(a+b)^2} \tag{14}$$

and the ratio of transverse pore area to perimeter is R = 2ab/(a + b). (Recall that λ = $R(\rho_0\omega/\eta)^{1/2}$). For later use, the average (1/4ab) $\int$ F(x,y;λ)dxdy over the pore cross section is

$$F(\lambda) = \frac{64}{\pi^4} \sum_{m,n\,odd} \frac{1}{m^2n^2Y_{m,n}(\lambda)} \;. \tag{15}$$

The z-component of particle velocity is given by Eq. (9) with F(x,y;λ) in Eq. (13) and the excess temperature by Eq. (10) with the replacement of λ in Eq. (13) by λ_T.

To derive a wave equation for the pressure, the fluid equations in Eqs. (5) through (8) are averaged over the pore cross section. Denote by $\rho_1(z)$ = (1/4ab) $\int \rho_1$(x,y,z)dxdy the average of the acoustic density in the pore, and similar notation for $v_z(z)$ and $T_1(z)$ for the transverse area average of v_z(x,y,z) and T_1(x,y,z). Use of Eq. (9) and Eq. (10) for the z-component of particle velocity and temperature, and the fluid equations (5) through (8) results in a set of averaged equations,

$$\frac{i\omega\rho_0}{F(\lambda)}\,v_z(z) = \frac{dp_1(z)}{dz} \tag{16}$$

$$-i\omega\rho_1(z) + \rho_0 \frac{dv_z(z)}{dz} = 0, \tag{17}$$

and

$$\rho_1(z) = \frac{(1-\gamma)F(\lambda_T) + \gamma}{c^2} p_1(z) . \tag{18}$$

The boundary conditions, $v_x(x,y,z) = 0$ and $v_y(x,y,z) = 0$ at the boundary, were used in obtaining Eq. (17) from the continuity equation, Eq. (6). Also, Eq. (10) for $T_1(z)$ was used in the equation of state Eq. (7) to obtain Eq. (18). Following Attenborough[2] we define a complex density from Eq. (16) and complex compressibility from Eq. (18).

$$\tilde{\rho} = \frac{\rho_0}{F(\lambda)} , \tag{19}$$

and

$$\tilde{C} = \frac{1}{\rho_0} \frac{\rho_1}{p_1} = \frac{(1-\gamma)F(\lambda_T) + \gamma}{\rho_0 c^2} \tag{20}$$

Eliminating ρ_1 from continuity and state Eqs. (17) and (18) and using Eqs. (19) and (20) we obtain:

$$i\omega \tilde{\rho} v_z(z) - \frac{dp_1(z)}{dz} = 0 \tag{21}$$

and

$$\frac{dv_z(z)}{dz} - i\omega \, \widetilde{C} \, p_1(z) = 0 \qquad . \qquad (22)$$

B. Extension to bulk media: Propagation constants and characteristic impedance.

Consider a fluid half space overlying a porous half space saturated by the same fluid. The pores are taken to have a rectangular cross section and let the capillary tube axis of each pore be at an angle θ with respect to the surface normal. The tortuosity $q = 1/\cos\theta$ for such a porous sample.[2,5,8,12] The open volume divided by the total volume is the porosity Ω of the sample. The boundary conditions are continuity of volume velocity (from mass conservation) and the continuity of pressure (from Newton's third law) at the porous interface.[2,3,5,8] As fluid only flows into the pores, the bulk particle velocity V_{zb} in the porous media is $V_{zb} = \Omega \, v_z / q$.[2,12] In order to account for propagation in a slanted pore (or other tortuous path), the differential dz in Eqs. (21) and (22) is replaced with qdz where $q > 1$ is the tortuosity.[2,5,8] Thus, the bulk acoustical equations are

$$i\omega \widetilde{\rho} q \, \frac{V_{zb}(z)}{\Omega} - \frac{dp_1(z)}{qdz} = 0 \qquad (23)$$

and

$$\frac{dV_{zb}(z)}{\Omega dz} - i\omega \, \widetilde{C} \, p_1(z) = 0. \qquad (24)$$

Differentiating Eq. (23) by z and eliminating V_{zb} with Eq. (24) give an expression

$$\frac{d^2p_1(z)}{dz^2} + \omega^2 \widetilde{\rho} \, \widetilde{C} \, q^2 \, p_1(z) = 0 \qquad (25)$$

for the pressure in the porous media. Assuming $p_1 \propto \exp(ikz)$ gives the dispersion relation

$$k^2 = \omega^2 q^2 \tilde{\rho} \tilde{C} = \frac{\omega^2}{c^2} q^2 \frac{\left[(1 - \gamma)F(\lambda_T) + \gamma\right]}{F(\lambda)} \qquad (26)$$

for the propagation constant k. From Eq. (23), the characteristic impedance is

$$Z = \frac{\tilde{\rho}\omega q^2}{\Omega k} = \frac{\rho_o}{F(\lambda)^{1/2}} \frac{q}{\Omega} \frac{c}{\left[(1 - \gamma)F(\lambda_T) + \gamma\right]^{1/2}} \qquad . \qquad (27)$$

The plane wave pressure reflection coefficient r_p for a wave normally incident from the fluid half space on the porous sample is

$$r_p = \frac{Z - \rho_o c}{Z + \rho_o c} = \frac{\left\{F(\lambda)\left[(1 - \gamma)F(\lambda_T) + \gamma\right]\right\}^{-1/2} - \Omega/q}{\left\{F(\lambda)\left[(1 - \gamma)F(\lambda_T) + \gamma\right]\right\}^{-1/2} + \Omega/q} \qquad . \qquad (28)$$

This relation will be used in the next section. Principal results of this section are the propagation constant Eq. (26) and characteristic impedance Eq. (27) which for rectangular pore porous media are to be evaluated with the function $F(\lambda)$ given in Eq. (15).

II. MEASUREMENT OF THE PHASE VELOCITY AND ATTENUATION

A. Description of the porous media.

A schematic drawing of the porous sample is shown in Fig. 2. Each subsection of the composite sample was of nominal length 7.68 cm. Figure 2 indicates a composite sample made from 5 individual pieces. Individual pieces were taped together at the joint. A sheet of Teflon was wrapped around the composite to facilitate insertion of the sample into the tube and to seal the sample-tube interface. Individual pieces were ceramics made by Corning.[13] The pores of each piece were nominally square in cross section and were

nominally straight in the longitudinal direction.

Three different square pore media were investigated. Table 1 lists characteristics of each. In Table 1, porosity was estimated using Ω = (number pores/unit area) $\times (2a)^2$ where a is the square semi-width. Flow resistivity was computed using Attenborough's equation[8] $\sigma = 8\eta q^2 S/a^2\Omega$ where S is a steady flow shape factor S = 0.89 for square pores[12] and a tortuosity q=1.1 was estimated from fitting the theory and experiment for the propagation constants as discussed below. In comparison with other porous media,[8] the square pore samples have low flow resistivity and high porosity. The average semi-widths are listed in table 1 for the 200 and 400 pores/inch^2 material for which the pore cross-sectional shape is well approximated as a square. However, due apparently to differences in the manufacturing process, the pores of the 300 pores/inch^2 samples were not well-approximated by a square shape. Two opposite corners of the otherwise square shape were rounded. The semi-width of a = 0.50 mm listed in Table 1 for the 300 pores/inch^2 samples was determined from the shortest diagonal length divided by (2 $2^{1/2}$). No explicit use was made of the calculated flow resistivity in the theory for the propagation constants.

B. Experimental Apparatus.

A block diagram for the experimental apparatus used to determine the attenuation and phase velocity of sound in porous media is shown in Fig. 3. A single cycle of a sine wave of duration 1.3 ms (for a center frequency of 750 Hz) was generated using an HP 3314A Function Generator. The signal was amplified using a Krohn-Hite Model 7500 Amplifier and was added to a DC polarizing voltage of 125 volts. The capacitive driver consisted of an aluminized mylar membrane stretched over a grooved backplate.[14] A Teflon ring around the perimeter of the driver was used to hold the mylar in place and to seal the driver inside of the tube. The tube was made of aluminum, had a length of 6.09 meters, an inside diameter of 14.6 cm, and a wall thickness of 1.11 cm. Radio Shack Model 270-090

microphones were glued into 10 cm long natural gas nipples having inside diameters of 9 mm. Holes were made and threaded in the tube 60 cm from each end and the microphones were inserted to be flush with the inner tube wall. Microphone signals were amplified using Tektronix AM 502 Differential Amplifiers. A Masscomp 5550 Minicomputer with a 12 bit analog-to-digital board was used to record and analyze the microphone signals. The digitizing rate was 300 kHz. The HP Function Generator was used to trigger the Masscomp 5550 and 30 pulses were averaged in the time domain for each measurement. The purpose of Microphone 2 was to give a reference time and space location for a pulse traveling in the empty tube so that the ambient sound speed could be determined from the pulse arrival time at Microphone 1.

A single microphone measurement method was used to determine the propagation constants in the square pore media. Figure 4a shows Microphone 1 measurement of pulses both with and without a sample present in the tube. As expected the pulse measured with the sample present is delayed in time and attenuated on account of passage through the porous media. The Fourier transform of a typical pulse indicated that the pressure level was about 20 dB above the background for frequencies in the range 200 Hz to 1300 Hz. The cutoff frequency[3] above which non-planar modes can propagate in the tube is 1376 Hz.

C. Determination of attenuation and phase velocity by the transfer function method.

Denote by $p_0(t)$ the incident pressure pulse at the right end of the sample and denote by $p_0(f)$ the Fourier transform of $p_0(t)$. The spectrum $p_m(f)$ after passage through a sample of length D_m is

$$p_m(f) = p_0(f) \exp(ikDm) \frac{1 - r_p^2}{1 - r_p^2 \exp(2ikD_m)} \tag{29}$$

where r_p is the frequency dependent pressure reflection coefficient Eq. (28) and k is the propagation constant for the porous media Eq. (26). Since the tube has a large diameter we approximate the characteristic impedance of the tube by $\rho_o c$ where c is the adiabatic sound speed in air. The $\exp(ikD_m)$ factor accounts for propagation through the sample, the $(1 - r_p^2)$ factor is for transmission into and out of the sample, and the denominator accounts for the multiple-reflection of waves within the sample.

In Eq. (29) the subscript m refers to the number of subsections used for a measurement. For example, m = 5 in Fig. 2 and Fig. 3. We may form a transfer function $h_m(f)$ from the results of two experiments on different porous sample lengths. The Fourier transform of the time domain pulses recorded by microphone 1 in Fig. 4b for two different sample lengths gives a transfer function from use of Eq. (29),

$$h_m(f) = \frac{p_m(f)}{p_1(f)} \approx exp[i(k - k_o)(D_m - D_1)] \tag{30}$$

where $k_o = \omega/c$ is the wavenumber for sound in air and k is given in Eq. (26). In Eq. (30) the single subsection spectrum $p_1(f)$ was used as a reference to divide out the frequency response of the capacitive driver and microphone and to divide out the transmission coefficient $(1 - r_p^2)$ in Eq. (29). The second part of Eq. (30) is an approximation because we have assumed $[(1 - r_p^2\, exp2ikD_1) / (1 - r_p^2 exp2ikD_m)] \approx 1$. The reflection coefficient r_p in Eq . (28) is significantly less than 1 for two reasons. First $|F(\lambda)| \approx 1$ for the frequency range of the present experiment, as a consequence of the low flow resistivity of the square pore samples used. Second, for the square pore material the porosity Ω is large. Hence, by Eq. (28) we expect $r_p^2 \approx 0$. Measurements of r_p with Microphone 2 in Fig. 3 for a nominal frequency of 750 Hz gave $|r_p^2| \approx (0.03, 0.05, \text{and } 0.03)$ for the (200, 300, and 400) pores/inch^2 samples, respectively.

The phase velocity and attenuation are computed from $k = \omega/c_{ph} + i\alpha$ and

$$c_{ph}(f) = \frac{2\pi f}{(D_m - D_l)^{-1} \, Im \, ln(h_m) + k_o} \tag{31}$$

and

$$\alpha(f) = - \frac{0.2 \, (D_m - D_l)^{-1}}{ln \, (10)} \, Re \, ln(h_m) \tag{32}$$

where c_{ph} is the phase velocity and α is the attenuation in dB/cm and where $Re \, ln(h_m)$ and $Im \, ln(h_m)$ refer to the real and imaginary parts of $ln(h_m)$, respectively.

Equations (30)-(32) were used to analyze the time domain pulses to obtain experimentally the phase velocity and attenuation for the square pore media. In all cases, we averaged over 30 times domain pulses before taking transforms. We also used five subsections so that $m = 5$ in Eqs. (30)-(32) and $(D_m - D_l) = 30.7$ cm nominally. Since a transfer function technique was used, it was not necessary to determine the pressure absolutely or to determine the frequency response of the microphone. A central assumption which was verified experimentally was the repeatability of any pulse measurements since $p_5(t)$ and $p_1(t)$ were measured at different times. The experimental results for the three different pore sizes given in Table 1 are displayed in Fig. 5. The experimental technique described here is similar to a method used by Ding[15] to measure the reflection coefficient of absorbents.

III. DISCUSSION OF EXPERIMENTAL AND THEORETICAL ATTENUATION AND PHASE VELOCITY

The experimental and theoretical attenuation and phase velocity were determined from use of Eqs. (30)-(32) and Eq. (26), respectively, and $k = \omega/c_{ph} + i\alpha$. Figures 5a and 5b

are the experimental and theoretical attenuation and phase velocity. For the theory, physical constants used were $\gamma = 1.4$, $N_p = 0.707$, $\rho_o = 1.2$ kg/m^3, $\eta = 18.5$ μP, and the adiabatic sound speed c from the propagation time of a pulse between Microphones 1 and 2 in Fig 3.

To get the acceptable agreement among theory and experiment as indicated in Figs. 5a and 5b, a tortuosity of q = 1.1 was used. Referring to Eq. (26) for the propagation constant k, note that the effect of tortuosity, (which is q $\geq$ 1), is to increase the attenuation α and decrease the phase velocity as one would intuitively expect. The calculated propagation constant for a tortuosity q = 1 results in an attenuation 10% lower than the measured value and a phase velocity 10% above the measured value. The discrepancy between experimental and theoretical phase velocity in Fig. 5b for the 300 pores/inch2 samples having pores of semi-width 0.50 mm may be due to the irregular shape of the pore cross-section as described in Sec. IIA.

Pores which have a tortuosity other than one have a radius which is not constant along the pore, have a slight curvature or tilt with respect to the axis normal to the surface, or are in a material for which the rigid frame assumption is not valid.[5] In the ceramic square pore material used in the experiment, the pores were straight and the pore walls had a density and moduli much greater than that of air. However, the semi-width of the squares as determined with a measuring microscope at the sample surface varied by approximately 5% from the average value. This variation could result in a tortuosity other than 1 if the 5% radius variation extended down a single pore also. Another possibility for a tortuosity other than one is that the ceramic pore walls were also porous. Use of a measuring magnifying glass indicated that the pore walls were indeed porous, with an average pore diameter of about 75 μm and pores as large as 100 μm. Wall pores were spaced by about 150 μm. Apparently the wall pores did not connect adjacent square pores. Intuitively, it seems that the effects of porous walls would be to increase the compressibility of the gas and hence, decrease the phase velocity. The attenuation would

also increase which is what was observed experimentally. Champoux[16] reported a tortuosity of 1.5 for the 200 and 400 pores/inch^2 samples using a non-acoustical technique.[17] It was difficult to estimate the uncertainty in this measurement since his technique requires accurate knowledge of the sample porosity which, due to wall porosity, was uncertain for the ceramic samples used.

It was not possible to align the pores in neighboring subsections of the composite sample as discussed in Sec. IIA. To investigate the effects of misalignment, attenuation and phase velocity were measured for composite samples consisting of 1-5 subsections. In the single subsection measurement the reference for the transfer function in Eq. (30) was taken to be the empty tube signal. The discrepancy between these measurements was less than 3% and showed no systematic trends. Sample misalignment was probably not the cause of an apparent tortuosity greater than one.

IV. DYNAMIC SHAPE FACTOR FOR SQUARE PORES

The hypothesis of Attenborough's[8] cylindrical capillary-tube based porous media theory was that a circular pore of radius a/n could be made acoustically equivalent to another pore of characteristic radius a by proper choice of n. The condition for acoustical equivalence is taken to be

$$Im \ \widetilde{\rho}_c(\lambda/n) = Im \ \widetilde{\rho}_s(\lambda) \tag{33}$$

where recall that $\lambda = a(\rho_0 \omega/\eta)^{1/2}$ for a circular pore of radius a or a square pore of semi-width a and subscripts c and s refer to circular and square pores, respectively. This condition occurs since the imaginary part of the complex density $\widetilde{\rho}$ is very large for small λ and thus determines the behavior of the propagation constants and impedance for small λ.[8]

The complex density is given generally for rectangular pores in Eq. (19). For square

pores of semi-width a the function $F_s(\lambda)$ is

$$F_s(\lambda) = \frac{64}{\pi^4} \sum_{m,n\,odd} \frac{1}{m^2 n^2 \left[1 + \left(i\pi^2/\lambda^2 \right) \left(m^2 + n^2 \right) \right]} \tag{34}$$

from Eqs. (14) and (15) for the special case a = b. For cylindrical pores[2],

$$F_c(\lambda/n) = 1 - \frac{2}{\sqrt{i}\,\lambda/n} \frac{J_1\left(\sqrt{i}\,\lambda/n\right)}{J_0\left(\sqrt{i}\,\lambda/n\right)} \tag{35}$$

where the dynamic shape factor n has been inserted and the J's are Bessel functions. The range[8] of n is thought to be $0.5 \leq n \leq 1$. The dependence of n on the shear-wave number λ is shown in Fig. 6.

The shear-wave number range in our experiments was $4.5 \leq \lambda \leq 18$. As indicated in Fig. 6, n is a frequency dependent parameter, which has been previously noted.[8]. Choosing a representative value of $\lambda = 4.532$, the corresponding value of the dynamic shape factor is n = 0.97. Propagation constants are shown in Fig. 7 for square and circular pore theories where the value n = 0.97 was used. Propagation constants for circular pores were computed from use of Eq. (35) for $F(\lambda)$ in Eq. (26) for k. There is less than 1% difference between the propagation constants calculated with these theories.

In Eq. (23) of Ref. 8 the author uses a steady flow shape factor S to define a flow resistivity for general porous media as $\sigma = 8\eta q^2 S/a^2 \Omega$ where a is a characteristic dimension of the pore equal to the pore radius for circular pores. The DC mass flux through a circular pore of radius $a/S^{1/2}$ is equal to that of a pore of characteristic dimension a, e.g. the semi-width a for a square pore. If we take the DC limit of n in Fig. 6 (i.e. $\lambda = 0$), we get Carman's value[12] for the steady flow shape factor of square pores, $S = 0.89 = n_{DC}^{1/2}$. Hence, we are led to conjecture that the steady flow shape factor[8] and the square root of the

dynamic shape factor are the same when the dynamic shape factor is evaluated at the DC limit.

V. CONCLUSION

We have developed a model for porous media consisting of rectangular pore capillary tubes. Viscous and thermal dissipation were accounted for. A series solution was obtained for the transverse variation of the longitudinal velocity and the excess temperature. A measurement technique using frequency domain analysis of short pulses propagated through high porosity, low flow resistivity samples was developed for determining propagation constants. Propagation constants were measured for a ceramic porous media having straight capillary tube openings with square cross sections. Use of an anomalous tortuosity factor q = 1.1 resulted in favorable agreement among experimental and theoretical values of the propagation constants. It was argued that the non-unity tortuosity value was due to the finite porosity of the ceramic pore walls. A dynamic shape factor n = 0.97 was suggested as the radius scaling factor for square pore and circular pore theories for the frequency range (200 Hz to 1300 Hz) and pore sizes (0.50 mm to 0.77 mm semi-width square pores) of this investigation. The steady flow shape factor was found to be calculable from the DC limit of the dynamic shape factor for square pores. Future work will involve an investigation of the anomalous tortuosity and propagation constant measurements on longer samples.

ACKNOWLEDGEMENTS

REFERENCES

1. J. M. Sabatier, H. Hess, W. P. Arnott, K. Attenborough and M. Romkens, "*In situ* measurements of soil physical properties by acoustical techniques," Soil Sci. Soc. Am. J. **54**, 658-672 (1990).

2. K. Attenborough, "Acoustical characteristics of porous materials," Physics Reports **82**, 179-227 (1982).

3. A.D. Pierce, *Acoustics: An Introduction to Its Physical Principles and Applications* (Acoustical Society of America, New York, 1989), Ch. 10.

4. J.W.S. Rayleigh, *The Theory of Sound* (Dover, New York, 1945) Vol. II.

5. C. Zwikker and C. W. Kosten, *Sound Absorbing Materials* (Elsevier, Amsterdam, 1949), Ch. 2.

6. H. Tijdeman, "On the propagation of sound waves in cylindrical tubes," J. Sound Vib. **39**, 1-33 (1975).

7. M. Stinson (private communication).

8. K. Attenborough, "Acoustical characteristics of rigid fibrous absorbents and granular materials," J. Acoust. Soc. Am. **73**, 785-799 (1983).

9. A. Cummings and I.J. Chang, "Acoustic propagation in porous media with internal

mean flow," J. Sound Vib. **114**, 565-581 (1987).

10. G.W. Swift, "Thermoacoustic engines," J. Acoust. Soc. Am. **84**, 1145-1180 (1988).

11. L.S. Han, "Hydrodynamic entrance lengths for incompressible laminar flow in rectangular ducts," J. Appl. Mech. **27**, 403-409 (1960). The author gives the solution for our Eq. (11) for a coordinate system at the center of a rectangle. He uses the differential equation for a different purpose than the present paper.

12. P. C. Carman, *Flow of Gases Through Porous Media* (Academic, New York, 1956).

13. The ceramics were manufactured by Corning Incorporated, Industrial Products Division, Corning, New York, 14831.

14. F. D. Shields, H. E. Bass, and L. N. Bolen, "Tube method of sound absorption measurement extended to frequencies far above cut off," J. Acoust. Soc. Am. **62**, 346-353 (1977).

15. Y. Ding, "A wave-tube impulse method for measuring sound-reflection coefficient of absorbents," Acustica **57**, 188-190 (1985).

16. Y. Champoux (private communication).

17. Y. Champoux and M. R. Stinson, "Measurement of tortuosity of porous material
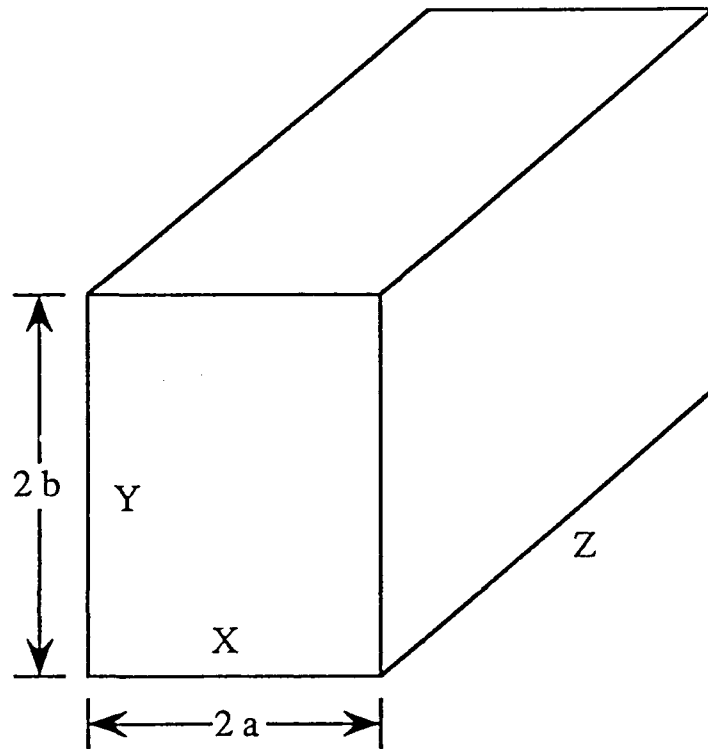
Roh, Arnott, et. al. JASA

and implications for acoustical modeling," J. Acoust. Soc. Am. Suppl. 1 **62**, S139 (1990).

TABLE I. Geometrical Properties of the Three Porous Samples Used.

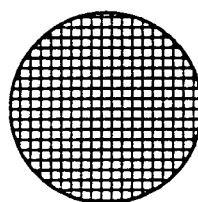| Pores/unit area (inch^{-2})	Semi-Width a (mm)	Porosity Ω (%)	Flow Resistivity σ (N m^{-4} s)
200	0.77	73	368
300	0.50	47	1356
400	0.57	81	606

FIGURE CAPTIONS

1. Coordinate system and geometry for the single pore calculation.

2. (a) Side and (b) end view of a square pore porous sample. To form the total sample several pieces of nominal length 7.68 cm were put together. It was not possible to align the squares from subsection to subsection.

3. Block diagram of the apparatus used to determine the phase velocity and attenuation of sound in low flow resistivity, high porosity samples.

4. (a) Sample waveforms for microphone 1 both with and without the porous material in the tube. The porous media was constructed as shown in Fig. 2. (b) Expanded schematic view of the tube and porous sample in Fig. 3. The Fourier transform after the incident pulse passes through the sample is $p_m(f)$.

5. (a) Experimental and theoretical attenuation and (b) phase velocity for the 3 square pore semi-widths given in Table 1.

6. Dynamic shape factor n to scale between square and circular pores of semi-width a and radius a/n, respectively.

7. (a) Attenuation and (b) phase velocity computed using a square pore of semi-width a = 0.50 mm and a circular pore of radius a = 0.50 mm / n where n = 0.97 is a dynamic shape factor.
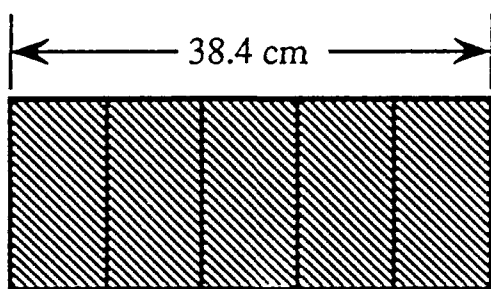
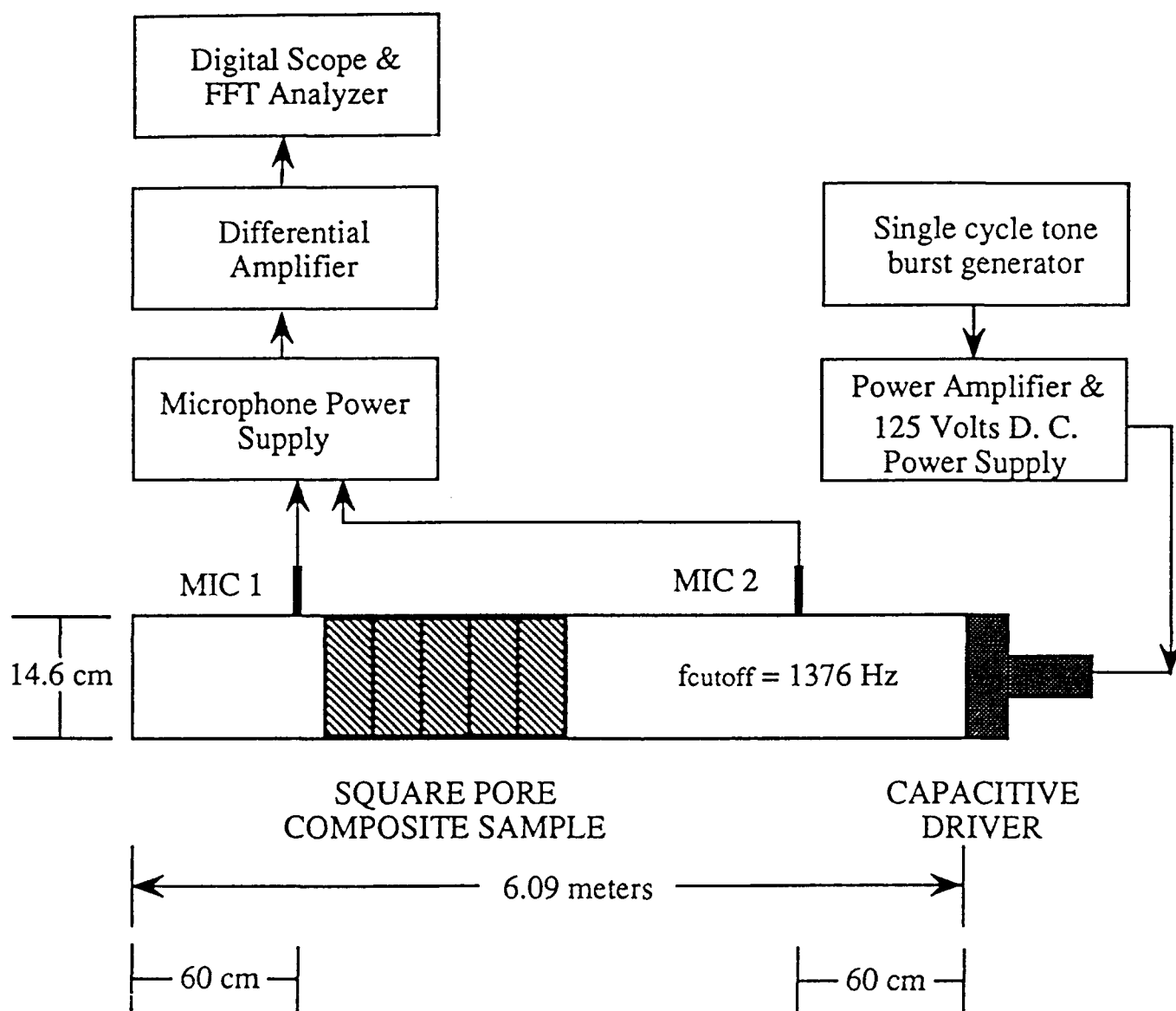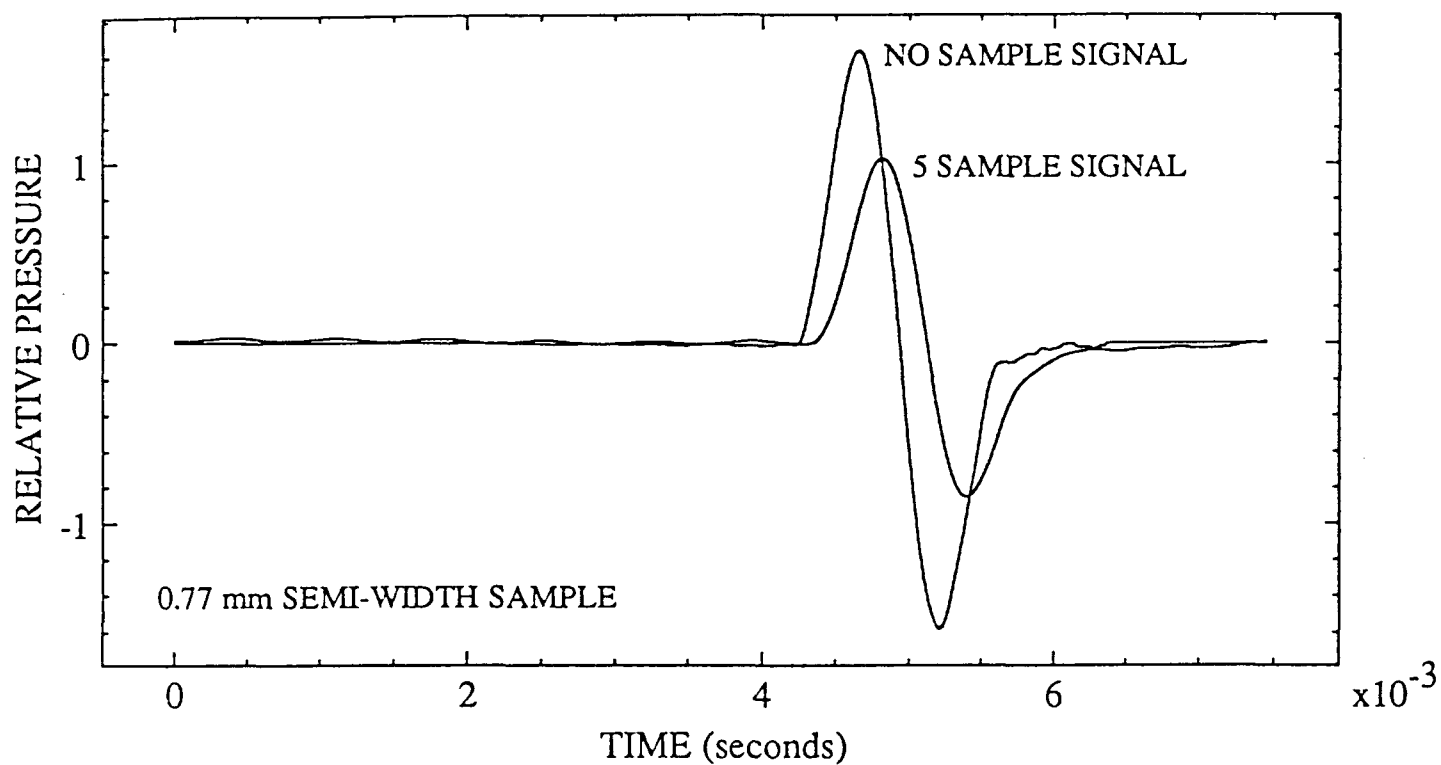SIDE VIEW:
5 SUBSECTION-
COMPOSITE SAMPLE

END VIEW

38.4 cm

14.2 cm

Digital Scope &
FFT Analyzer

Differential
Amplifier

Microphone Power
Supply

Single cycle tone
burst generator

Power Amplifier &
125 Volts D. C.
Power Supply

MIC 1

MIC 2

14.6 cm

fcutoff = 1376 Hz

SQUARE PORE
COMPOSITE SAMPLE

CAPACITIVE
DRIVER

6.09 meters

60 cm

60 cm

(a)

(b)

(4.532 , 0.97)